THESIS FOR THE DEGREE OF LICENTIATE OF ENGINEERING

Modeling of PMSM Full Power Converter Wind Turbine with Turn-To-Turn Fault

JOACHIM HÄRSJÖ

Division of Electric Power Engineering
Department of Energy and Environment
Chalmers University of Technology
Göteborg, Sweden 2014

Modeling of PMSM Full Power Converter Wind Turbine with Turn-To-Turn Fault
Joachim Härsjö

Copyright © Joachim Härsjö, 2014.

Division of Electric Power Engineering
Department of Energy and Environment
Chalmers University of Technology
SE-412 96 Göteborg, Sweden
Telephone + 46 (0)31-772 1000
Chalmers Bibliotek, Reproservice
Göteborg, Sweden 2014

Abstract

Over the past several years the number of renewable energy installations has shown a strong increase rate. Due to the ambition to close down fossil and nuclear power plants, this rate of increase is not expected to decline during the coming decades. In particular, wind energy represents one of the most dominant renewable energy sources. Due to the fact that wind energy has become such an important source of electric power, stable operation as well as high availability is needed. With the increasing amount of installations and the increase in power ratings of the single turbines, the task of maximizing the operational time of the wind turbine is more and more important in order to reduce the cost of energy. Under this scenario, early detection of fault conditions can be important to minimize the damage and therefore reduce the downtime of the wind turbine. It is therefore important to understand the behavior of the faulty component, both in order to limit the damage, but also to be able to more efficiently detect the fault.

This work presents a system model of the electrical parts of a full power converter wind turbine with a permanent magnet synchronous machine as generators. The system model is modular based, where each sub-system can be replaced by a model of a faulty component in order to study its impact on a system level. Statistics has shown that faults occur in all of the different sub-systems of the turbine, not only in the electrical parts. However, generator faults are among the most common wind turbine component to fail, and in addition it is a costly and time consuming component to replace. This work presents an analytical model of a permanent magnet synchronous machine with a turn-to-turn fault, which is the most common winding fault. There are other works available in this subject, however there is little information regarding how to detect a turn-to-turn fault.

The derived analytical model of the faulty machine is verified using a finite element model. In order to simulate the transition of the generator from healthy to faulty conditions, a flexible model of the permanent magnet synchronous machine is developed. The flexible model can also be used to emulate the evolvement of the fault by using a variable resistance in the fault loop of the investigated winding. The developed model can also be used to understand which quantities that needs to be monitored to be able to early detect a faulty condition in the machine. It is shown that turn-to-turn faults in the permanent magnet synchronous generator can be detected through monitoring of the harmonic content of the stator current in the rotating reference frame as the harmonic content slightly change when a turn-to-turn-fault arise.

Index Terms: Wind energy, Wind turbine modeling, full power converter wind turbine, permanent magnet synchronous machine (PMSM) modeling, fault, turn-to-turn, fault detection.

Acknowledgement

This research work has been carried out within Swedish Wind Power Technology Centre (SWPTC). The financial support is gratefully acknowledged.

I would like to sincerely and wholeheartedly thank my supervisors Associate Professor Massimo Bongiorno, Professor Ola Carlson and Dr. Stefan Lundberg for their guidance and support throughout the research work. A special thanks to Massimo for his patience and for the effort he gave to support me in order to be able to complete this thesis.

I would also like to thanks my colleague Christian Du-Bar for the fruitful discussions you provided together with the possibility to share simulation models.

A special thanks goes to the industry partners; especially Luca Peretti, Ville Sarkimaki (ABB), Emad Ahmed, Christof Sihler(GE Global Research) and Niklas Almgren (Göteborg Energi) whose experience and guidance with data and real world issues helped in improving this research.

Another special thanks to Sara Fogelström whose administrative support within SWPTC made it possible to carry out the project without any difficulties.

I am grateful to everyone in my office; Nicolas, Pavan, Pinar and Pramod for making the time in the office more enjoyable. I would also like to thank all my colleagues at the division of Electrical Power Engineering and within SWPTC.

Finally I would like to thank my family, with a special thanks to my beloved wife Johanna, for all their love and support.

Joachim,
Gothenburg, 2014

Preface

The Swedish Wind Power Technology Centre (SWPTC) is a research centre for design of wind turbines. The purpose of the Centre is to support Swedish industry with knowledge of design techniques as well as maintenance in the field of wind power. The research in the Centre is carried out in six theme groups that represent design and operation of wind turbines; Power and Control Systems, Turbine and Wind loads, Mechanical Power Transmission and System Optimisation, Structure and Foundation, Maintenance and Reliability as well as Cold Climate.

This project is part of Theme group 1.

SWPTC's work is funded by the Swedish Energy Agency, by three academic and thirteen industrial partners. The Region Västra Götaland also contributes to the Centre through several collaboration projects.

List of publication

1. J. Härsjö, M. Bongiorno, O. Carlson, “Dually Fed Permanent Magnet Synchronous Generator Condition Monitoring Using Generator Current”, EWEA 2013: Europe’s Premier Wind Energy Event, February 2013, Vienna, Austria

2. J. Härsjö, M. Bongiorno, S. Lundberg, O. Carlson, “Permanent Magnet Synchronous Generator Inter-turn Fault Identification Using Stator Current Analysis”, 9th PhD Seminar on Wind Energy in Europe, September 2013, Visby, Sweden

Content

Chapter 1

Introduction

1.1 Background

The world's energy consumption keeps increasing, and due to the climate issues and the cost of fossil fuel the renewable energy sources present a sustainable solution. Wind and flowing water have been utilized by mankind throughout the ages as an energy source for various applications. For the last few decades wind has been utilized for electrical power production and is likely to be utilized further. Countries such as the U.S. and China (as well as the European Union) have stated that they aim to incorporate more wind power in their system, where up to 25 % of energy production should be wind based [1]. As such, the total number of installed turbines is increasing. However is not only the amount of turbines that increase; turbines have increased in both physical size and in power rating in order to achieve better land exploitation, benefit from scale economies and to reduce the operation and maintenance costs [2]. This increase in power rating will also contribute towards the goal of increasing the wind energy penetration. But in order for wind energy to become a true competitive energy source, the cost of wind energy needs to be on par with other conventional energy sources. Even though the increase in turbine size helps to decrease the operational and maintenance cost, the operational and maintenance cost is still comparably high for wind turbines due to the hard-to-access structure and that they are often located in remote locations [1]. For onshore wind turbines the operational and maintenance cost could be as high as 20-30% of the total levelized life cycle cost [3].

It is not only the cost of energy which drives the wind industry forward, as grid integration has become more demanding. The increasing amount of energy produced through wind has lead to the need of regulation when interconnecting wind farms into the power network, similar to other conventional power plants. This has motivated stricter wind energy grid codes, and future wind grid codes may also incorporate more grid support functions, both during normal operation as well as during grid fault conditions. The grid codes of today require that turbines are to remain connected during grid voltage drops with limited duration, and some grid codes also require that the wind turbine should provide voltage support. However, remaining connected during grid disturbances can cause additional mechanical stresses for the fixed-speed and DFIG wind turbines [4]. The extra stresses will affect the amount of maintenance needed and possibly the lifetime of the turbine. The wind turbines electrical and mechanical interaction is a field which requires further research in order to fully understand the additional stresses and by extension how to reduce them. Therefore, accurate models of the electrical drive system which can be incorporated into larger system models of wind turbines are needed to be able to study the effects of the faults on both the component level as well as on a system level. However, all additional stresses does not necessarily originate from a grid disturbance, as it may originate from an faulty component within the wind turbine

The increasing amount of power electronics and computational power in wind turbines presents the opportunity for more accurate measurements and monitoring while at the same time increasing the controllability. Utilizing the monitoring capabilities together with the knowledge of how a faulty component behaves, presents the possibility for more accurate and timely detection of faults within the turbine. It also enables the possibility to detect new types of faults which previously lacked efficient methods of detection.

1.2 Aim of thesis and scientific contributions

The aim of this thesis is to present how to analytically model the electrical subassembly of a direct-driven full power converter wind turbine using a permanent-magnet synchronous machine as generator. The models should be modular to increase flexibility and to be more easily integrated into larger system models, which include both electrical and mechanical models. The modularity will also make the models interchangeable, which makes them usable for other turbine topologies but it will also provide the possibility to investigate the effects of faulty components by the exchange of a the model of a healthy component for a model of a faulty component. Since the generator is a critical component for wind turbines which is both costly and time consuming component to change if failed, an efficient generator health monitoring system is needed. This thesis will therefore focus on the development of an analytical generator model which is to be used as the first step in the development of a complete method for detecting the most common machine winding fault: the turn-to-turn short circuit. The developed analytical model is verified during various operating conditions using a finite element model. Using the derived model a detection method is derived which can be used as an indication of a turn-to-turn fault.

1.3 Thesis outline

In this thesis, a short review of the development of wind turbines and the current trends and future possibilities will be presented in Chapter 2. Chapter 3 presents models over the electrical sub-systems of a full power converter wind turbine, where the modeled sub-systems are generator, the converter and its control and protection system together with the grid and filter. All the sub-systems will be interconnected to perform a complete system simulation during both typical operation and for more a dynamic operation in the form of a low voltage ride through. Chapter 4 presents a brief review typical faults occurring within the different wind turbine sub-systems, including the mechanical, structural and the electrical sub-systems. Chapter 5 presents an analytical model of a permanent magnet synchronous machine with a turn-to-turn fault, both in the stationary reference frame and in the synchronously rotating reference frame. To verify the analytical model a finite element model is developed with which the analytical models is compared. Using the derived model, a method of detection a turn-to-turn fault is suggested. Chapter 6 presents the conclusions and together with some topics which requires further research.

Chapter 2

Wind turbine topology review

This chapter gives a short introduction to the most common wind turbine topologies, a brief review of future trends as well as a short review of the possibilities future advancements in materials and computer software that may enable new possibilities for the wind turbine industry.

2.1 Introduction

The amount of wind turbines installed in the power grid has steadily increased since the late 1980s, both in numbers and power rating. Figure 2.1 presents the globally installed wind power up until the year 2013 [5] which shows how the installed wind power capacity has grown exponentially over the past decade.

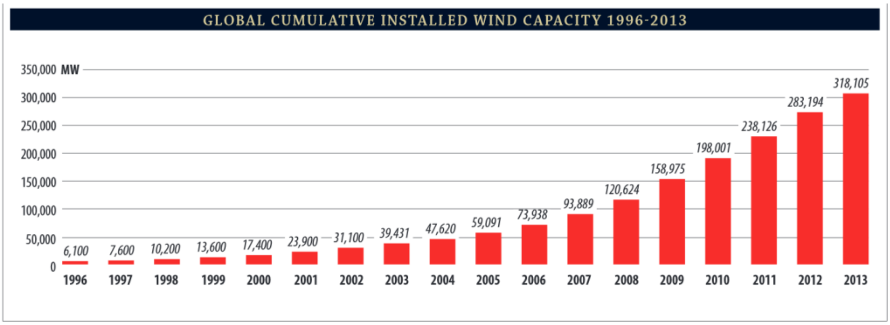

Figure 2.1 The global cumulative installed wind capacity from 1996 to 2013 [5]

Wind turbines have evolved from the smaller fixed-speed 1980's turbines with a power rating of less than 100 kW. During the mid 1990's the typical turbine rating was between 750 kW to 1000 kW[6], and the modern turbines have a power rating up to 7.5 MW [7]. The modern turbines utilize variable-speed drive and can typically also provide some grid support features. This chapter presents a brief overview of the turbine development from fixed-speed to the variable-speed with full power converter, the current trends within wind turbine topologies and some future scenarios for wind turbines.

2.2 Fixed-speed wind turbine

The early wind turbines utilized simple and cheap solutions compared to modern ones, where a standard induction machine directly connected to the grid was used as the generator. Since induction machines typically operate in the speed range of 1000 to 3000 revolutions per minute in a 50 Hz grid, the fixed-speed turbine needs a gearbox. Figure 2.2 illustrates a fixed-speed wind turbine using an induction machine directly connected to the grid.

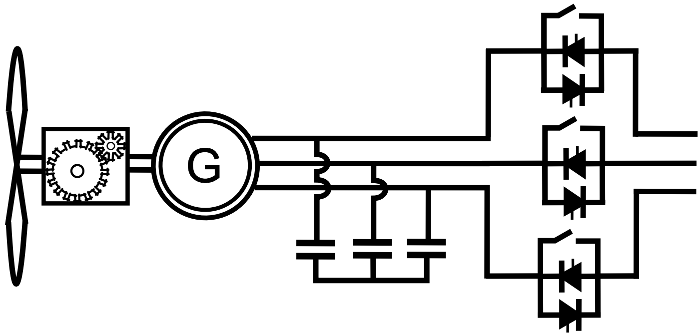

Figure 2.2 Conceptual image of a fixed-speed wind turbine supplemented with a capacitor bank and a soft starter.

Induction machines can generally be categorized either as a squirrel-cage or a wound rotor type. The squirrel-cage rotor type uses a simpler, cheaper and more robust construction as compared with the wound rotor type and it mainly requires bearing maintenance since the rotor circuit consists of short-circuited and non-isolated aluminum bars. This design makes it less sensitive to pollution, moist, and vibrations.

The wound rotor, as the name implies, uses wound conductors instead of bars. This makes it easier to utilize copper instead of aluminum, leading to an increase of the machine efficiency since copper has higher conductivity than aluminum. However, copper is more expensive than aluminum and the production method of the wound rotor is more complicated than the squirrel-cage, leading to an increased cost of the wound rotor machine. On the other hand, the wound rotor solution has big advantage compared to the squirrel-cage, being the option to connect to the rotor circuit via slip rings. The rotor accessibility provides more control possibilities, i.e. the rotor currents can be manipulated using passive components or power electronics, where the later part will be described more in Section 2.3.

To limit the inrush current during the start-up of the fixed-speed turbines, soft starters are used. The soft starters consist of back-to-back connected thyristors (see Figure 2.2), which are used to regulate the voltage supplied to the wind turbine which by extension provides control over the inrush current. Once normal operation is reached, the soft starter is bypassed in order to reduce losses. There are some other drawbacks when using an induction machine directly connected to the grid as generator other than the high inrush current; one of them is the needed of reactive power for magnetization. This characteristic can be an issue for turbines connected to weak grids. To cope with this issue the turbine can be complemented with additional supporting systems that locally provide reactive power compensation, where the simplest solution is the installation of capacitor banks, as shown in Figure

2.2. However, the capacitor bank only complements the turbine during normal operation; it cannot provide any protection or support for the turbine during grid faults. Another issue of this kind of solution is that any grid disturbance has a direct impact on the turbine. In the event of a severe voltage dip in the grid, causing a greatly reduced turbine terminal voltage, large currents in the generator will be experienced. This forces the activation of the protection system which disconnects the turbine from the grid. However, modern grid codes do not allow this behavior as will be discussed in Section 2.5

Another drawback of using an induction machine directly connected to the grid is its very limited speed variation. The speed variation is caused by the slip associated with induction machines which is typically one or two percent of rates speed. This narrow speed range is not sufficient to optimally cope with the natural fluctuations of the wind. As a result an optimal operation point with respect to energy extraction cannot be reached which also causes increased mechanical stresses.

2.3 Doubly-fed induction generator

The Doubly-Fed Induction Generator (DFIG) is the most common turbine used today as it represents almost 50 % of all installed turbines [8]. It uses a wound rotor induction machine where the rotor circuit is connected via slip rings to a back-to-back converter. The other side of the back-to-back converter is connected to the point of common connection of the grid and machine stator, see Figure 2.3.

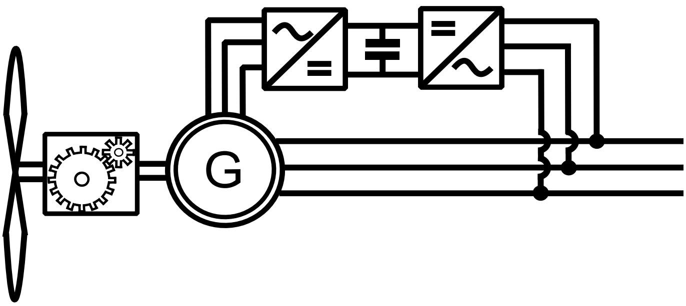

Figure 2.3 Conceptual image of a DFIG wind turbine

The converter enables control of the currents in the rotor circuits, which in turn enables a limited control over generator speed. The gained speed range is dependent on the converter rating, where a larger converter provides a larger speed range. Therefore a trade-off must be made between turbine speed range and converter size and cost. Typically the converter rating is about 25 % of the turbine rated power, allowing speeds of 60 % to 110 % of synchronous speed [9]. This speed range is sufficient for wind turbine applications due to the relatively narrow operation region originating from the wind speed. Due to the introduction of variable-speed operation, the turbine can extract the wind energy more efficiently, i.e. a variable-speed wind turbine can produce more energy compared to a fixed-speed turbine. However, the addition of a converter also introduces additional losses. This will reduce the turbine output power which (despite the more efficient variable speed) will make the net gain of energy small. However, the large advantage of the DFIG compared with the fixed-speed is the reduction of mechanical stresses through the enabling of variable speed operation.

The DFIG converter is able to provide the reactive power needed for magnetizing the induction machine, i.e. a DFIG doesn't need any additional complimentary system. However, since the stator is directly connected to the grid, like the fixed-speed turbines, the issue of too large stator currents during a grid fault is still present. For less severe grid faults a DC-crowbar in the converter is able to dissipate the additional rotor energy caused by the grid fault. The converter is still active and can provide grid support during DC-crowbar operation. For more severe grid faults where DC-crowbar is unable to dissipate all the additional energy, in order to protect the converter the rotor windings are short circuited through an AC-crowbar which effectively turns the DFIG into a squirrel-cage induction machine. However, the short-circuiting of the rotor circuit sudden change the DFIG into a squirrel-cage, which can produce extra mechanical stresses on the wind turbine [8]. Even if the rotor circuit is short-circuited, the stator fault currents are still large and as a result the turbine protection system may disconnect the turbine from the grid, like the fixed-speed turbine would.

2.4 Full power converter wind turbine

Instead on only using a partly rated converter connected to the rotor circuit, a full power converter connected at the interface between the stator and the grid can be used, see Figure 2.4.

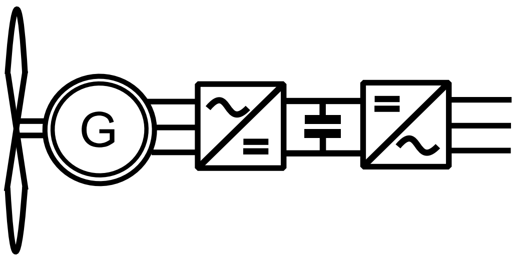

Figure 2.4 Conceptual image of a full power converter wind turbine topology

As mentioned in the previous section, a convert with a higher rating increases the initial cost of the turbine as well as the overall losses. However, with the use of full power converters the turbine controllability greatly increases. The full power converter will during normal operation decouple the generator from the grid, as the back-to-back configuration will allow generator controller to operate independently of the grid voltage as long a there is a DC-link voltage. If the converter has a DC-crowbar, it is able to cope with the low voltage ride through without disconnection. Due to the decoupling provided by the full power converter, there will not be any additional mechanical stressed during a low voltage ride through as for the DFIG and the fixed-speed wind turbines. In addition, the full power converter is able provide grid supporting functions both during normal operation as well as during grid faults.

An advantage of the full power converter is its flexibility regarding generator type. It can be utilized together with various machine types but the most common for wind turbine applications are squirrel-cage induction machine, electrically excited synchronous machine and permanent magnet synchronous machine. Variable-speed is easily achieved with the full power converter due to the grid and machine decoupling which makes it possible to choose the machine frequency freely. By varying the frequency supplied to the machine its synchronous speed varies, hence, the machine speed varies. The option to freely choose the frequency enables what is called the direct-drive, which utilize a large multi pole generator with low mechanical speed that eliminates the need for a gearbox. In order to reduce the size and weigh while increasing the machine efficiency of a generator, powerful magnets can be used. However, by the use of permanent magnets instead of an electrically excited rotor some of the machine controllability is lost. However, the main drawback of the permanent magnet machine is the cost of the magnets which makes the initial cost of the generator higher compared to the electrically excited machine.

2.5 Current wind turbine trends and future possibilities

The main objective of any power producing unit is to minimize the cost of the energy delivered to the grid. For wind turbines the “fuel” can be considered free whereas the cost arises from the initial investment as well as the operation and maintenance. As such, the most efficient system is not necessarily the best solution since it may have too high initial cost or excessive maintenance cost. However, it is not solely the cost of energy which is the driving force of wind turbine development as stricter grid codes will also be a deciding factor.

In general, there is no trend towards a single new topology but rather the trend lies in further development of the existing topologies where an increase in reliability is desired[10], especially for off-shore applications where maintenance is more difficult. Off-shore turbines are starting to be more and more attractive due to higher wind speeds and more available space compared to land. There is also a trend towards replacing dispersed turbines with larger wind farms[10] and that the fixed-speed turbines, at least for power ratings greater than one MW, are disappearing from the market in favor of the variable-speed topologies [9].

2.5.1 Grid code compliance

Countries with high wind penetration typically have specific grid codes which only apply to wind turbines with various specifications. However, all grid codes have specified a low voltage ride though profile during which a turbine must stay connected. If the voltage level becomes lower than the minimum voltage specified in the grid code or have a longer duration the turbine is allowed to disconnect and stop as a protective procedure. The low voltage ride through profiles varies from country to country and Figure 2.5 illustrates the profiles of some countries which are presented in [11].

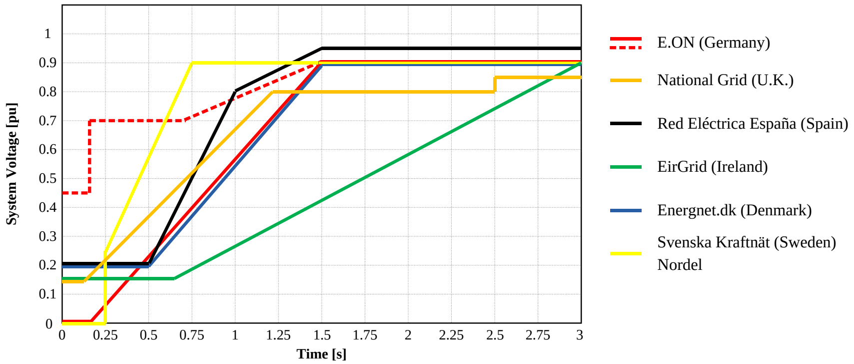

Figure 2.5 The different low voltage ride through presented in [11]

As can be seen, there are variations between the different grid codes where all turbines must fulfill all of the criteria imposed by the grid codes. For manufacturer to make specific turbine for single markets/grid codes is not economically justifiable, i.e. turbines should be able to cope with all criteria specified in all grid codes by only adjusting the software to enable the desired behavior. The full power converter topology has the highest controllability and can therefore cope with low voltage ride through more efficiently than the DFIG and fixed-speed topology. However, research has successfully been performed in order to enable grid fault ride through for the DFIG which still makes it a viable option [9].

2.5.2 Turbine structure

Wind turbines have with time grown in size in order to reduce the cost of energy. Since the early 1980’s the modern turbine power has almost increased a hundred times, see Figure 2.6 [12]. The reason for the increase in hub height is due to the wind gradient, where higher heights provide greater wind speeds. The increase in rotor blades provide a larger rotor sweep area which in turn allows for a higher energy capture for a given wind speed. The constant development of new light weight (and more durable) materials allows for the even larger wind turbines in the future. Larger towers and blades does however create practical issues during construction, where the main issue lies with the logistics to move the component to the turbine erection site. As such, research is being conducted on blades which can be built in segments and assembled on site while still maintaining the aerodynamic performance and durability [13].

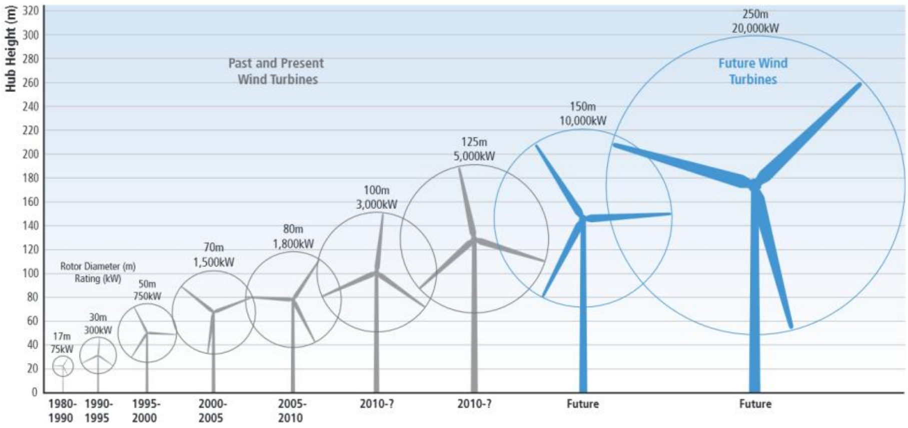

Figure 2.6 The increase wind turbine size over the last three decades and a possible future scenario based on the current trend. [12]

The wind turbine efficiency in extracting the wind energy has improved through better aerodynamics and structural dynamics and has resulted in an overall yearly improvement of wind turbine energy output of 5 %[14].

2.5.3 Generator

The main trend within wind generators is to improve the reliability for the currently available topologies[10]. There are general improvement possibilities for the materials such as core materials with lower losses or to use insulation materials with nano-particles in order to create a thinner insulation layer with increased heat conductivity while keeping the withstand voltage at a desired level [15]. However, since the cost of energy is very important for wind turbines, it can be beneficial to use proven and off-the-shelf generators. The typical electrical machine operates at higher speeds which will require a gearbox for wind turbine operation. The use of full power converters allows for a variety of generators, which has contributed to the increase of diversity regarding generator types. By using a gearbox there are more components in the drive-train chain that reduce the overall efficiency and potentially increase the turbine failure rate. The alternative is to use the direct drive solution, but the direct drive generators are large, heavy, and have to be custom made which all contribute to an increase in the initial investment cost. However, modern and optimized direct drive drives have a comparable weight to that of geared systems [16]. Figure 2.7 shows a direct drive generator which is presented in [17].

Figure 2.7 Photo of a direct drive generator in the MW range, presented in [17].

A method which both reduces the weight of a generator as well as improves its reliability and efficiency is to use permanent magnet. However, almost all of the rare-earth magnetic materials are mined in China, and China has made protective action which has lead to a reduction in their exports of these materials. This reduction has in turn both increased the current price of power magnets, as well as made it difficult to predict the future price [16]. As such the cost of saving weight by the use of permanent magnates may not be justifiable. If the magnet price stabilizes at reasonable level, this kind of electrical machine will likely be used more due to its superior performance compared to electrically excited solutions[10]. However, in order to remove the dependence of expensive materials, other machine designs are considered for wind turbine applications. A candidate is the reluctance machine which has a comparably high power-density-to-cost ratio, where another possible candidate is the electrically excited claw-pole machine [18]. The drawback for these machine types is that they have a low power factor which requires a larger converter.

Research is currently being conducted to be able to use non-scarce materials to produce strong magnets. A potential material is an iron-nitrate compound which possibly has the highest saturation ever recorded for a material [19]. However, the material is not stable and demagnetizes easily. Other research is conducted to find new types of material combinations which can be uses as substitutes for the rare earth metals, both in magnetic properties as well as in extending the operation range

[19]. However, a new material must also be able to be manufactured in a cost-effective manner in order for it become a commercially viable option.

There are other machine types which in the future could be used as wind turbine generators such as axial flux machines, air core machines, brushless DFIG, magnetically geared generators and superconducting generators. These generator types will not be further address in this thesis but some further information regarding these generator types can be found in [9].

There are some studies on transformer-less wind turbine which helps in reducing the overall nacelle weight [20]. This can be achieved either by using specially designed generators with a higher rated voltage or by the use of power electronics.

2.5.4 Power electronics

The use of power electronics has been considered in wind application since the 1980s. Back then power electronics was utilized in soft starters to limit the inrush current of the fixed-speed turbines. Along with the development of power electronics, its use in wind energy systems has gradually shifted towards a mean of regulating the generated power [21]. The use of full power back-to-back converters enables wind turbines to become fully controllable generation units which simplifies their integration into the grid. With the latest improvement of power electronics, the full power converter is expected to become the dominating topology on the market, as the wind turbines with full power converters are the preferred choice in the best selling range of wind turbines [21].

The typical converter topology used for wind applications is a two-level voltage source converter which is operating at a voltage less than one kV. However, with turbines reaching power ratings of several MW a single converter may suffer from large switching losses due to the high currents. Therefore some manufacturers use back-to-back converters connected in parallel where the machine side converters are connected to different segments of the generator windings. The advantage of this setup is that it uses the proven low voltage converters [21]. By the use of a multilevel converter the voltage can be increased in order to reduce the current and possibly also enable a transformer-less system. The three-level neutral point diode clamped is one of the most commercialized topologies available on the market. The advantages of using the three-level compared with the two-level converter is the extra voltage level, lower switching frequency and that it has lower voltage gradient stresses [21]. There are other types of multilevel topologies which are discussed in [22-24] and in [25], where [25] has a wind turbine perspective.

The Silicon (Si) based semiconductors of today are close to what is theoretically achievable regarding performance and efficiency. There is therefore research conducted on new types of semi-conducting materials with better performance than Si which can improve performance of high-power power electronics. A potential material is Silicon Carbide (SiC), which has higher conductivity than Si and it can operate at a higher temperature while being a more efficient heat conductor. SiC is still expensive and there is only FET transistors and diodes available. However, SiC transistors are still not a real competitor for Si based Insulated Gate Bipolar Transistors (IGBT) in high power applications. But by the use of SiC instead of Si in wind power applications will according to [26] improve the system efficiency.

The use of power electronic converters also provides the possibility of integrating energy storage in the wind turbine by installing batteries in the DC-link. This provides the possibility of reducing the impact of the stochastic nature of wind power and make the turbine more controllable and predictable [27]. Less stochastic power from wind increases the grid stability and the stored energy can also be used for additional features such as frequency control. The storage capacity and power rating of the energy storage depends on the acceptable grid power fluctuation and the variation in wind speed. Since energy storage increases the investment cost of a turbine there will be a trade-off between power fluctuations and cost [28].

2.6 Summary

This chapter presented a brief topology overview of fixed- and variable-speed wind turbine topologies. Then the current trends and some future possibilities for wind turbines were presented. It was concluded that all topologies presents strength and weaknesses and no topology has been shown to have an overall superior performance. This makes the choice of turbine topology non-trivial. As such, there is currently no converging trend towards a single wind turbine topology. However, with the grid code compliance of the full power converter wind turbines, it is likely to be the dominating solution in the future. A more general trend in the wind industry is the improvement the currently available topologies with focus on increasing component reliability in order to reduce the cost of energy. The reliability aspect becomes even more important for off-shore wind turbine applications where maintenance and repair is more difficult.

However, the full power converter together with a permanent magnet synchronous machine as generator is from an operational perspective an attractive solution due to its high controllability provided by the converter and its higher efficiency compared to electrically excited generators. If the permanent magnet price stabilizes at reasonably price, then the number of full power converter wind turbines with a permanent magnet synchronous machine should increase in the future.

The following chapter presents how to model the electrical parts of a full power converter using a permanent magnet generator. The models can be used to investigate how the wind turbines electrical parts behave during normal operation as well as during operation with a faulty component.

Chapter 3

PMSM full power converter wind turbine model – From rotor speed to grid power

This chapter presents analytical models of a full power converter wind turbine with a three phase permanent magnet machine as generator. The different electrical parts of the turbine are described and the system is modularly designed so that each sub-system is easily exchangeable. This is to be able to study the impact of a faulty sub-system on a system level.

3.1 Introduction

A wind turbine can be modeled at various detail levels depending on the model application. The turbine models range from simplified model, used for simulations to study the effects of integrating wind farms to a national grid, to highly accurate and detailed finite element models to study the behavior of a single component within the turbine. The parts of the wind turbine of interest for this thesis are mainly the electrical components, namely the generator, the back-to-back converter, and the grid connection. However, the mechanical drive-train is also modeled through a simple two-mass model as it will simplify the comparison between measurements and simulations. This chapter presents dynamic models of the sub-systems of a full power converter wind turbine with a permanent magnet synchronous machine (PMSM) as generator, which can be used to study of the interaction between the sub-systems during both normal operation as well as during operation under faulty conditions. The fault can either be in the grid or within one of the sub-systems. In the case of a faulty sub-system, the model presented in this chapter should be replaced by a model of the faulty sub-system. Figure 3.1a illustrate the complete setup of sub-systems used to model the full power converter wind turbine used in this thesis. Figure 3.1b illustrates the full power converter, consisting of two two-level converters connected in back-to-back. Figure 3.1b also includes the overvoltage protection (the DC-crowbar) discussed in later in the section.

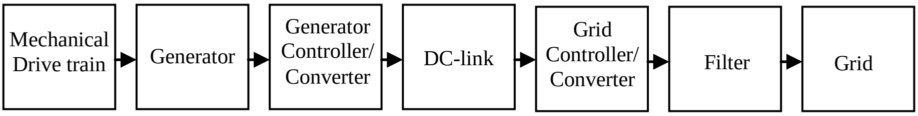

a

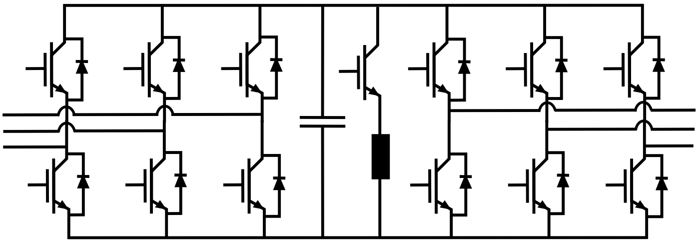

b

Figure 3.1 Figure a illustrate a system overview represented using blocks. Figure b illustrates the two-level converters connected back-to-back with the DC-link and the overvoltage protection.

As mentioned earlier, this chapter presents models of a one- and two-mass model mechanical drive train, the generator together with a method of how to calculate the inductances from the geometry, and the machine and grid side controllers together with the protection system. Finally, the complete system is simulated during typical operating condition and during grid fault to verify the low voltage ride through capabilities.

3.2 Mechanical drive train model

The purpose of electrical machines is to convert electrical energy into mechanical rotation or vise versa. Depending on what the machine is connected to the mechanical model can vary. A simple model of the mechanical drive train for direct-drive wind turbines is the two-mass model, which can be described as:

$$J_{turbine}\frac{d\Omega_{turbine}}{dt} = T_{wind} - K_s\alpha - K_d\frac{d\alpha}{dt} - B\Omega_{turbine} \tag{3.1}$$

$$J_{generator}\frac{d\Omega_{generator}}{dt} = K_s\alpha + K_d\frac{d\alpha}{dt} - B\Omega_{generator} - T_{generator} \tag{3.2}$$

$$\frac{d\alpha}{dt} = \Omega_{turbine} - \Omega_{generator} \tag{3.3}$$

where J is inertia, Ω denotes the mechanical rotational speed, T is the torque, K_s is the shaft stiffness, K_d is the self damping constant, B is the friction constant, and α is the shaft displacement angle in radians. As seen in (3.1) and (3.2) the shared torque of the two inertias is $K_s\alpha + K_d\frac{d\alpha}{dt}$. It can also be seen that a positive value of T_{wind} will increase the speed, while positive value of $T_{generator}$ will reduce the speed. The typical shaft that connects the wind turbine rotor with the generator is a comparably short shaft with a large diameter. As such, the mechanical shaft is in this thesis assumed to have a high stiffness while being poorly damped. If the shaft is excited by a torque step, the two masses will cause a misalignment between the two ends of the shaft, as the interties will oppose any change in movement. Since the shaft stiffness is high, any transient speed difference between the two masses will be small as well as the misalignment angle. However, since the shaft has poor damping any speed difference between the two masses will result in an oscillation in the speed in one of the masses relative to the other, before reaching steady state. This behavior is presented in Figure 3.2, which presents the speed $\Omega_{generator}$ for a step in T_{wind}. The speed is normalized to with respect to the pre-step value.

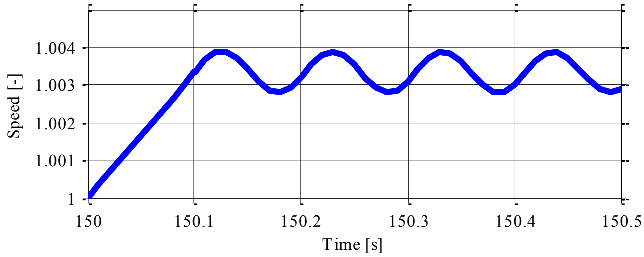

Figure 3.2 The oscillation in $\Omega_{generator}$ from a stepwise increase in T_{wind}. This speed response is typical for a stiff but poorly damped shaft between two inertias, represented as a two-mass model.

A more simplified mechanical model is the one-mass model, described as

$$J_{total}\frac{d\omega_{rotor}}{dt} = T_{wind} - T_{generator} \tag{3.4}$$

where J_{total} is the sum of both the turbine and generator inertia. The one mass model behaves as a mechanical low-pass filter for the speed, where the input is the torque difference between the aerodynamic torque T_{wind} and the generator torque $T_{generator}$. Using the one-mass model over the two-mass model will make the system more ideal as the generator speed will not oscillate as in the case of the two-mass model.

3.3 Permanent magnet synchronous machine

The rotor of a synchronous machine rotates with the same speed as the stator flux for one pole pair machines. This is due to the alignment of the rotor and stator fluxes. For machine with more pole pairs the mechanical and electrical speed is scaled with the number of pole pairs, i.e.

$$\omega_r = p\Omega_r \tag{3.5}$$

where ω_r is the electrical rotor speed, p is the number of pole pairs and Ω_r is the mechanical rotational speed. For the rotor to contribute to the magnetic flux it requires either currents within the rotor or permanent magnets. By using magnets the rotor can be made smaller, simpler, and lighter at the cost of no controllability of the rotor magnetic field strength. The way the magnets are mounted on the rotor impacts the rotor magnetic field strength, but it will also affect the machine behavior to some extent. One way to mount the magnets is to glue them (using glue or any other adhesive method) to the rotor surface; This technique has a small impact on the airgap reluctance due to that the reluctance of magnets is almost equal to the reluctance of air. However, for high speed machines the mechanical stresses on the adhesive can be excessive. To reduce the risk of magnets detaching from the rotor an option is to make sockets in the rotor to place the magnets, thus creating what is known as an inset mounted rotor. The inset mounted magnets can be coated with an additional layer of rotor iron making the magnets to be completely mounted inside the rotor, and then, an interior mounted rotor is obtained. A machine using one of these rotor setups does not have uniform airgap reluctance since the rotor material and air typically has different reluctance. Thus the magnetic coupling becomes dependant on the rotor position and will cause cogging torque if not accounted for by a machine controller.

Figure 3.3 shows the different rotor mounting setups.

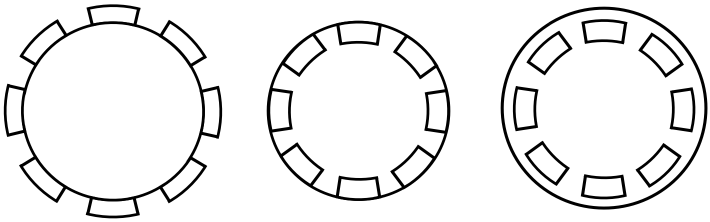

Figure 3.3 The different magnet mounting setups. Surface mounted to the left, inset in the middle and interior to the right

A good PMSM type to use as generator for a direct-drive wind turbine is the radial flux machine which surface mounted magnets [29]. The phase voltage of a wye-connected PMSM with surface mounted magnets can electrically be modeled as

$$u_a = R_s i_a + \frac{d\Psi_a}{dt} \tag{3.6}$$

where u_a is the voltage of phase a, R_s is the stator winding resistance, i_a is the current in phase a, and $\Psi_a$is the flux linking phase a. The flux linking phase a can be described as

$$\Psi_a = (L_\sigma + L)i_a + M_{ab}i_b + M_{ac}i_c + \Psi_{pm}\cos(\theta_r + \varepsilon) \tag{3.7}$$

where L_σ is the leakage inductance, L is the self inductance, M is the mutual inductance, Ψ_{pm} is the permanent magnet flux, θ_r is the angle between the reference point and the north pole of the permanent magnet and ε is the angle between phase a and the reference.

It can be assumed that the coupling between two phases is unidirectional, i.e.

$$M_{ab} = M_{ba} \tag{3.8}$$

and that the stator phases are identically constructed except for being shifted in space which makes identical inductive coupling and leakage parts, i.e.

$$M_{ab} = M_{ac} = M_{bc} = M \tag{3.9}$$
$$L_{\sigma_a} = L_{\sigma_b} = L_{\sigma_c} = L_\sigma \tag{3.10}$$

If saturation is neglected the inductance values becomes constant, i.e.

$$\frac{dL_s}{dt} = \frac{dM}{dt} = 0 \tag{3.11}$$

Utilizing these assumptions and selecting phase a as reference for the permanent magnet alignment, i.e. φ is zero in (3.7), then the flux derivative of phase a can partly be evaluated to

$$\frac{d\Psi_a}{dt} = (L_\sigma + L)\frac{di_a}{dt} + M(\frac{di_b}{dt} + \frac{di_c}{dt}) - \omega_r \Psi_{pm} \sin(\theta_r) \tag{3.12}$$

since derivative of the electrical position of the rotor is the rotors electrical speed, i.e.

$$\frac{d\theta_r}{dt} = \omega_r. \tag{3.13}$$

The flux derivatives for the other two phases can be evaluated in a similar fashion. The three phase machine can be modeled using matrixes as

$$\begin{bmatrix} U_a \\ U_b \\ U_c \end{bmatrix} = \begin{bmatrix} R_s & 0 & 0 \\ 0 & R_s & 0 \\ 0 & 0 & R_s \end{bmatrix} \begin{bmatrix} i_a \\ i_b \\ i_c \end{bmatrix} + \begin{bmatrix} L & M & M \\ M & L & M \\ M & M & L \end{bmatrix} \frac{d}{dt} \begin{bmatrix} i_a \\ i_b \\ i_c \end{bmatrix} - \omega_r \Psi_{pm} \begin{bmatrix} \sin(\theta_r) \\ \sin\left(\theta_r - \frac{2\pi}{3}\right) \\ \sin\left(\theta_r + \frac{2\pi}{3}\right) \end{bmatrix} \tag{3.14}$$

where it is assumed that phase b and phase c are $-\frac{2\pi}{3}$ and $\frac{2\pi}{3}$ electrical radians shifted, respectively.

Equation (3.14) can be written in compressed from as (where a bold quantity represents either a vector or a matrix)

$$\mathbf{U} = \boldsymbol{R}\mathbf{i} + \boldsymbol{L}\frac{d\boldsymbol{i}}{dt} + \boldsymbol{E} \tag{3.15}$$

where $\mathbf{U}$ represent the voltage vector, $\boldsymbol{R}$ represents the resistances matrix, $\boldsymbol{L}$ represents inductance matrix and $\boldsymbol{E}$ represents the back-EMF vector. In this thesis bold an entity represents either a matrix or a vector. A circuit representation of a wye-connected three phase PMSM is shown in Figure 3.4.

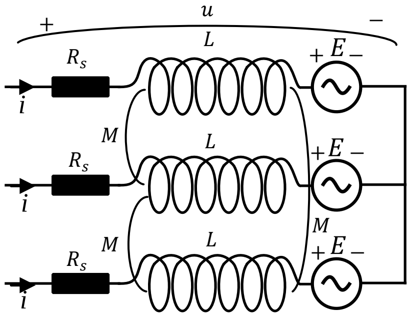

Figure 3.4 Circuit representation of a wye-connected three phase PMSM

In order to be able to simulate the machine model, a state-space representation can be used:

$$\frac{d\mathbf{x}}{dt} = \boldsymbol{A}\boldsymbol{x} + \boldsymbol{B}\boldsymbol{u} \tag{3.16}$$

$$\boldsymbol{y} = \boldsymbol{C}\boldsymbol{x} + \boldsymbol{D}\boldsymbol{u} \tag{3.17}$$

where $\boldsymbol{x}$ is the state variables, $\boldsymbol{u}$ is the system inputs and $\boldsymbol{y}$ is the system output. However, the machine is neither linear nor time invariant since both the $\boldsymbol{A}$ and the $\boldsymbol{B}$ matrix vary with time. Therefore, during simulations both the $\boldsymbol{A}$ and the $\boldsymbol{B}$ matrix should be updated every time step. In this thesis the currents are chosen as the state variables for the machine model. As such, if (3.15) is converted into state-space form it becomes

$$\frac{d\boldsymbol{i}}{dt} = \mathbf{L}^{-1}(\mathbf{U} - \boldsymbol{R}\mathbf{i} - \boldsymbol{E}) \tag{3.18}$$

where

$$\boldsymbol{A} = \mathbf{L}^{-1}(-\boldsymbol{R}),\quad \boldsymbol{B} = \mathbf{L}^{-1},\quad \boldsymbol{C} = \boldsymbol{I},\quad \boldsymbol{D} = \mathbf{0} \tag{3.19}$$

$$\boldsymbol{x} = \mathbf{i}\ ,\ \boldsymbol{u} = \boldsymbol{U} - \boldsymbol{E} \tag{3.20}$$

The machine parameters and the back-EMF can either be measured directly or indirectly. In the indirect case the values are obtained through calculations performed on measurement data. The values of the inductances can be calculated using the machine geometry.

3.3.1 Inductance calculations using the machine geometry

Inductance is a property of a conductor that induces a voltage both within itself as well as in other conductors when the current flowing through it changes. This is due to the coupling between electric current and magnetic flux. The ability of inducing a voltage within the conductor itself is the self inductance, and it is also a measurement of how much magnetic energy a coil is able to store within itself. The ability to induce voltage in other conductors is caused by the mutual inductance, which relates how much of the stored energy in one coil is accessible from another coil. The amount of energy that can be stored depends on the permeability of the materials surrounding the coil. The surrounding material also determine the reluctance of the flux path, where the reluctance of a flux path is defined as

$$\mathcal{R} = \frac{l}{\mu_0 \mu_r A} \tag{3.21}$$

where l is the length of the flux path, μ_0 is the permeability of vacuum, μ_r is the relative permeability of the material and A is the cross-section area of the path. As such, the reluctance can be acquired from the geometry of a machine. A practical method is to divide the path into smaller segments to create a reluctance circuit as illustrated in Figure 3.5. In Figure 3.5 the different segments have different reluctance, such as the stator tooth $\mathcal{R}_t$, the stator back between two teeth $\mathcal{R}_s$, the airgap and magnet between tooth and rotor $\mathcal{R}_g$, the leakage airgap between teeth $\mathcal{R}_\sigma$, and the rotor core $\mathcal{R}_r$. At each tooth there is a magnetomotive force (MMF) source to represent the coil wound around the tooth. The upper loops, 1 to n, represents the stator circuit while the lower loops, $n+1$ to $2n$, mainly represents the rotor and airgap circuits. Note the absence of MMF sources in the lower loops, as it is only the current carrying coils which are of interest for calculating inductances and not the flux from the permanent magnets.

The reluctance of each part can be estimated with different accuracy, where the simplest method is to estimate each part with a rectangular shape and neglect the shape of the tooth shoe, slot leakage and the slot opening effect on the airgap. In [30] a more accurate method of estimating the reluctance of each segment is presented.

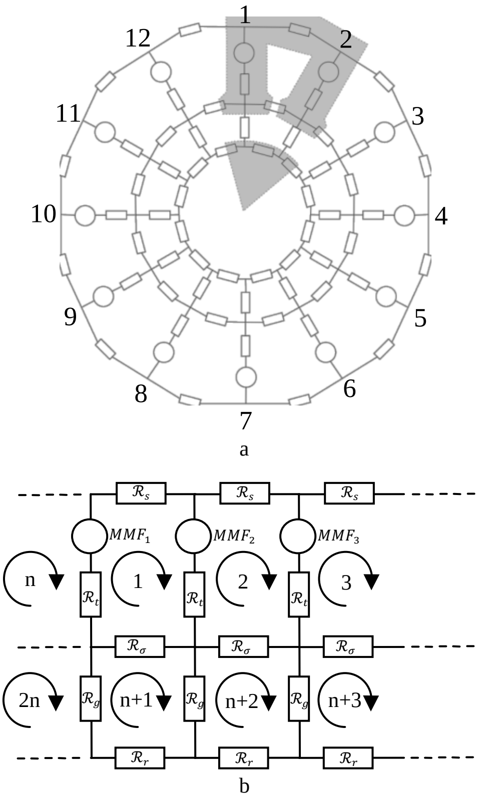

Figure 3.5 Reluctance circuit of a PMSM. Figure a presents the reluctance grid as it is connected in the machine. Figure b presents a more general reluctance grid with its generated flux loops.

The estimated reluctance values are used in a reluctance matrix which describes each reluctance loop shown in Figure 3.5. The matrix is express as

$$\boldsymbol{\mathcal{R}} = \begin{bmatrix} \sum_{k=1}^{2n} \mathcal{R}_{1,k} & -\mathcal{R}_{1,2} & -\mathcal{R}_{1,3} & \dots & -\mathcal{R}_{1,2n} \\ -\mathcal{R}_{2,1} & \sum_{k=1}^{2n} \mathcal{R}_{2,k} & -\mathcal{R}_{2,3} & \cdots & -\mathcal{R}_{2,2n} \\ -\mathcal{R}_{3,1} & -\mathcal{R}_{3,2} & \sum_{k=1}^{2n} \mathcal{R}_{3,k} & \dots & -\mathcal{R}_{3,2n} \\ \vdots & \vdots & \vdots & \ddots & \vdots \\ -\mathcal{R}_{2n,1} & -\mathcal{R}_{2n,2} & -\mathcal{R}_{2n,3} & \dots & \sum_{k=1}^{2n} \mathcal{R}_{2n,k} \end{bmatrix} \tag{3.22}$$

where $\sum_k^{2n} \mathcal{R}_{x,k}$ is the summation of all the reluctance components in contact with loop x. For example, the reluctance part $\mathcal{R}_{1,2}$ is the reluctance component present both in loop 1 and loop 2, i.e. $\mathcal{R}_t$. However, $\mathcal{R}_{1,3}$ will be zero as loop 1 and 3 do not share any reluctance elements. In the case of $x = k$ it refers to the element exclusively present in that loop, for instance $\mathcal{R}_{1,1} = \mathcal{R}_s$. The non-diagonal elements of the matrix are the shared elements of the different loops, where the negative sign is due to the direction of the flow in each loop being identical. As the loops only share elements with neighboring loops, most of the elements in the reluctance matrix will be zero.

The driving MMF can be described as a column vector, whose dimension is equal to the number of loops in the reluctance circuit. The elements consist of the sum of all the MMF sources within the loop with each flux direction taken into account. For the circuit presented in Figure 3.5, the MMF elements are

$$\boldsymbol{MFF} = \begin{bmatrix} MMF_1 - MMF_2 \\ MMF_2 - MMF_3 \\ \vdots \\ MMF_n - MMF_1 \\ 0 \\ \vdots \\ 0 \end{bmatrix} \tag{3.23}$$

since the loops from $n + 1$ to $2n$ does not contain any MMF sources.

The flux in each loop can then be calculated as

$$\boldsymbol{\Phi} = inv(\boldsymbol{\mathcal{R}})\ \boldsymbol{MMF} \tag{3.24}$$

where the flux in each tooth can then be calculated as the difference between the two neighboring loops sharing the tooth reluctance $\mathcal{R}_t$. Using this method, it is possible to calculate how the flux from a single coil is distributed in the machine through the excitation of a single MMF source. Figure 3.6 shows the fluxes in each tooth when only MMF_1 is excited. The fluxes are normalized with respect to the flux in tooth 1. It is assumed that MMF_1 is a coil consisting of one turn carrying one ampere and that all teeth have the same positive orientation of flux. Since the reluctance of the stator back is small compared to the airgap, the flux will distribute across the entire machine. However, the stator back is not negligible small since the neighboring teeth get a larger portion of the flux. In this example, the machine has twelve teeth and the flux is therefore higher in the neighboring tooth 2 and 12.

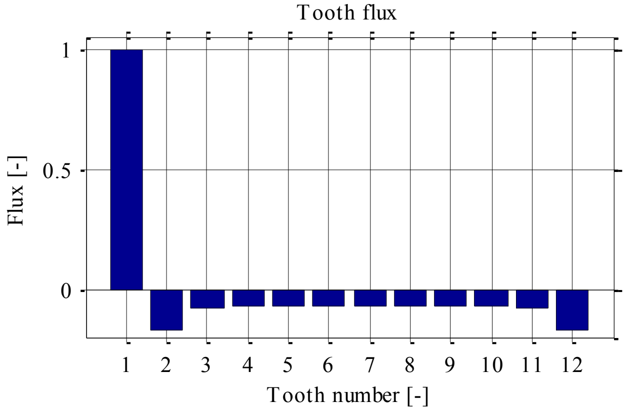

Figure 3.6 Flux distribution from a single coil

If the permeability is assumed to be constant, i.e. no saturation, the inductance is constant. The amount of flux that a coil produce is not solely dependent on the reluctance, as it also depends on the number of turns in the coil and on the current that flows in the coil. The amount of flux produced by coil x that reaches coil y, i.e. Φ_{xy} can be calculated as (if leakage is neglected)

$$\Phi_{xy} = \frac{MMF_x}{\mathcal{R}_{xy}} = \frac{n_x I_x}{\mathcal{R}_{xy}} \tag{3.25}$$

where n_x is the number of turns carrying the current I_x in coil x and $\mathcal{R}_{xy}$ is the reluctance of the flux path from coil x to coil y.

The self inductance, L, is defined as the flux produced by the coil multiplied with the number of turns in the coil, in relation to the current in that coil, i.e.

$$L = \frac{\psi_{xx}}{I_x} = \frac{n_x \Phi_{xx}}{I_x} \tag{3.26}$$

ψ_{xx} is the flux linkage originating from coil x and Φ_{xx} is the amount of flux in coil x that originate from coil x. Mutual inductance, M, is defined as the amount of flux produced by coil x that reaches the coil y multiplied with the number of turns the in the second coil, in relation to current of the first coil, i.e.

$$M = \frac{\lambda_{xy}}{I_x} = \frac{n_y \Phi_{xy}}{I_x} \tag{3.27}$$

If saturation is neglected, i.e. the flux is linearly proportional to the current, the self- and mutual inductances can be simplified by the insertion of (3.25) in to (3.26) and (3.27) respectively. Thus

$$L = \frac{n_x}{I_x}\Phi_{xx} = \frac{n_x}{I_x}\frac{n_x I_x}{\mathcal{R}_{xx}} = \frac{n_x^2}{\mathcal{R}_{xx}} \tag{3.28}$$

$$M = \frac{n_y}{I_x}\Phi_{xy} = \frac{n_y}{I_x}\frac{n_x I_x}{\mathcal{R}_{xy}} = \frac{n_x n_y}{\mathcal{R}_{xy}} \tag{3.29}$$

which states that for non-saturated system, the inductance is inversely proportional to the reluctance of the flux paths.

With the knowledge of the flux distribution, the self- and mutual inductance per tooth and turn can then be calculated using (3.28) and (3.29) respectively. These inductances can then be used to build up the phase inductances with the knowledge of how the phases are distributed among the teeth and how many turns each coil consists of. The total self inductance can be calculated as

$$\boldsymbol{L_s} = \sum_{\boldsymbol{i=1}}^{\boldsymbol{m}}\left(\sum_{\boldsymbol{j=1}}^{\boldsymbol{m}} \boldsymbol{L_{ij}}\,\boldsymbol{n_i n_j}\right) \tag{3.30}$$

where $\boldsymbol{L_{ii}}$ is the self inductance of one tooth and $\boldsymbol{L_{ij}}$ is the coupling terms from one tooth to another. $\boldsymbol{L_{ij}}$ for teeth not belonging to the same phase are assumed zero when calculating the self inductance. $\boldsymbol{n_i}$ and $\boldsymbol{n_j}$ is the number of turns surrounding tooth $\boldsymbol{i}$ and $\boldsymbol{j}$ respectively, and $\boldsymbol{m}$ is the total number of teeth.

A similar approach can be applied when calculating the mutual inductance

$$\boldsymbol{M} = \left(\sum_{\boldsymbol{i=1}}^{\boldsymbol{m}}\left(\sum_{\boldsymbol{j=1}}^{\boldsymbol{m}} \boldsymbol{L_{ij}}\,\boldsymbol{n_i n_j}\right)\right) \tag{3.31}$$

with the difference that $\boldsymbol{L_{ii}}$ is assumed zero as well as the $\boldsymbol{L_{ij}}$ elements of the phases of no interest.

3.3.2 Buildup of back-EMF

Faraday's law of induction states a change of magnetic flux in within a closed conductive loop will induce an electromotive force, EMF, to oppose the change in flux. This can be described as

$$E = -n\frac{d\Phi}{dt} \tag{3.32}$$

where E is the induced EMF, n is the number of turns of the closed loop, and Φ is the flux passing through the loop. In the case of a PMSM, the change in flux is mainly due to a the movement of the permanent magnets in relation to the coils. Since the amplitude of the flux from the permanent magnet is constant (for a given geometry), the level of the induced voltage is therefore solely determined by the rotational speed, where a greater speed gives a larger induced voltage. The shape of the induced voltage depends on the flow of flux in the tooth where the shapes of the magnet and stator tooth affect flux delivery. A simplified case is illustrated in Figure 3.7 where magnets are moving below a stator tooth. The flux is assumed constant with no leakage, giving that the positive direction flux in the tooth increases as more of the positive magnets area is beneath the tooth. The maximum amount of flux in the tooth occurs in this example when the entire magnet is beneath the tooth. As the magnet keeps moving the linkage between the tooth and that magnet decreases until there is no linkage, i.e. there is no part of that magnet beneath the tooth. The flux in the tooth is not only dependant on a single magnet, as it is the net flux in the tooth which induces the voltage. As such, the tooth net flux in this example is zero when half the north magnet and half the south magnet are both beneath the tooth.

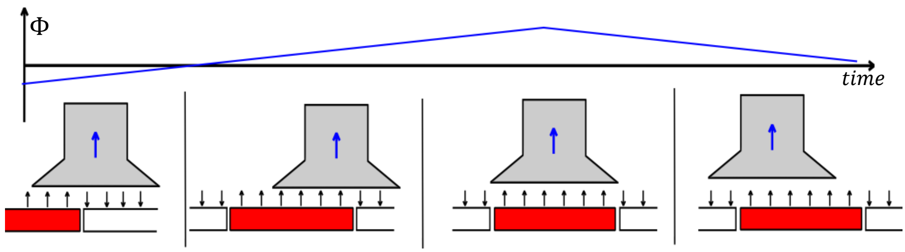

Figure 3.7 Flux in stator tooth for different times instances with magnet moving beneath it.

The induced voltage can be calculated using the shape of the flux in the tooth and (3.32). In the example illustrated in Figure 3.7 the shape of induced voltage will be a square wave due to the constant slope of the flux alteration. In order to produce a sinusoidal shaped induced voltage, a sinusoidal flux alternation is required which can be achieved through some geometric adaptations. However, a perfect sinusoidal with no harmonic content is practically impossible to achieve, but well designed machines can, from a controller perspective, be approximated to an ideal sine wave, where all the frequency components besides the fundamental can be neglected.

The total induced voltage, i.e. the machine back-EMF, in one phase is the summation of all the induced voltages in the coils belonging to this phase. However, as the coils are physically distributed in the machine, the induced voltage is not necessarily linearly proportional to the number of coils in one phase. The teeth electrical distance in the machine can be calculated as

$$\varphi = \frac{p\,360°}{\sum t} \tag{3.33}$$

where φ is the electrical distance between two teeth, p is the number of pole pairs and $\sum t$ is total number of teeth. Therefore each induced voltage should be treated as a vector with a magnitude and direction. If the coils have the same amount of turns then the amplitude is equal for all coils, but they are phase shifted depending the on displacement from the selected reference. Machines typically have a symmetric distribution giving a constant tooth displacement for each phase. An illustrative example of back-EMF buildup of a machine with six coils is illustrated in Figure 3.8, where each short arrow represents the contribution from a single coil. The long arrow is the total back-EMF measurable while running the machine in an open circuit mode, i.e. no current.

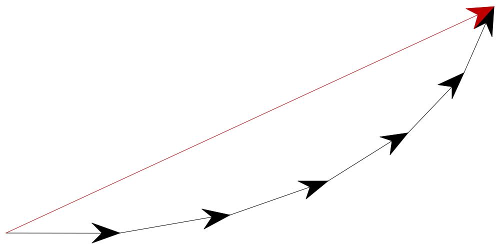

Figure 3.8 Example of the buildup of phase back-EMF for one phase, where the red arrow presents the resulting back-EMF, which is the sum of the black arrows.

The coil distribution will also affect the harmonic content of the back-EMF. The shape of the back-EMF can also be influenced by selecting the direction of the coil windings in order to make the coils electrically closer, which will be used in Section 5.4.1. An illustrative example is if the coils are electrically separated $150°$ but by winding the second coil in an opposite direction compared to the first coil. In this case the electrical distance then becomes $150° - 180° = -30°$ which electrically is much closer and will thus have a combined effect. The resulting back-EMF of the two is illustrated in Figure 3.9. As illustrated, the case of an electrical distance of $-30°$ results in a total amplitude which is greater than for a single coil whereas the case of an electrical distance of $150°$ results in a smaller total amplitude than for a single coil.

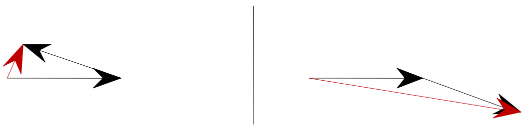

Figure 3.9 Build up of phase back-EMF for one phase, left $150°$shift and right $-30°$ shift. The red arrow represents the sum of the two black arrows.

3.4 Overview of the wind turbine control system

There are several alternatives to control the back-to-back connected converters used in full power converter wind turbines. In this thesis, the method of using a proportional-integral (PI) controller is chosen for both the machine-side and the grid-side converter. An overview of the modeled system is presented in Figure 3.10, where all the measured and used quantities are presented.

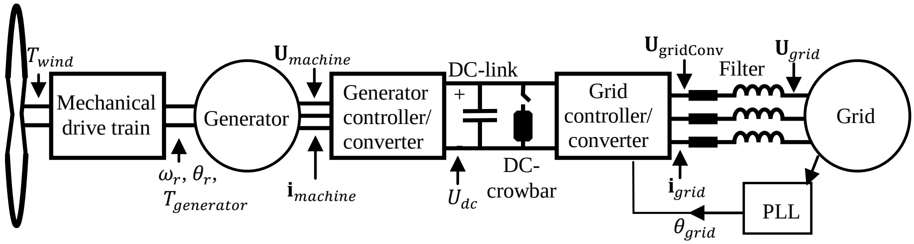

Figure 3.10 An overview of the modeled system together with the measured quantities.

The generator model uses in this thesis is the PMSM described in the previous section. However, to able to use a PI control for the machine-side converter the machine model needs to be transformed to the rotating reference frame using the transformations described in Appendix A. Since a machine connected to an inverter typically use a floating neutral point, (A.3) is used in this thesis. The angle difference between the rotor magnet-north-pole and the axis aligned with the flux created from positive phase a current (referred to as θ_r) is chosen as transformation angle θ. As such when the north pole of a rotor magnet is perfectly aligned with the flux created by the a-axis θ_r is zero. Using this reference the q current represents active power while the d current represents reactive power [31].

Applying the transformation matrix $T(\theta_r)$ to the PMSM machine model described by (3.15) gives

$$\boldsymbol{U}_{dq} = \boldsymbol{R}'\boldsymbol{I}_{dq} + \boldsymbol{dL}'\boldsymbol{I}_{dq} + \boldsymbol{L}'\frac{d\boldsymbol{I}_{dqf}}{dt} + \boldsymbol{e}_{dq} \tag{3.34}$$

where

$$\boldsymbol{R}' = T(\theta_r)\,\boldsymbol{R}\,T^{-1}(\theta_r) \tag{3.35}$$

$$\boldsymbol{dL}' = T(\theta_r)\,\boldsymbol{L}\frac{dT^{-1}(\theta_r)}{dt} \tag{3.36}$$

$$\boldsymbol{L}' = T(\theta_r)\boldsymbol{L}\,T^{-1}(\theta_r) \tag{3.37}$$

$$\boldsymbol{e}_{dq} = T(\theta_r)\,\boldsymbol{e}_{abcf}. \tag{3.38}$$

Evaluated, (3.34) become

$$\boldsymbol{u_{dq}} = u_d + ju_q = R_s\boldsymbol{i}_{dq} + (L-M)\frac{d\boldsymbol{i}_{dq}}{dt} - j\omega_r(L-M)\boldsymbol{i_{dq}} + j\omega_r\Psi_{pm} \tag{3.39}$$

The torque produced from an electrical machine modeled in the rotating reference frame can be expressed as

$$T = \frac{m}{2}p(\Psi_d i_q - \Psi_q i_d) \tag{3.40}$$

where m is the number of phases and p is the number of pole pairs. For a PMSM with the chosen reference angle the flux in the rotating reference frame is described as

$$\Psi_d = \Psi_{pm} + L_d i_d \tag{3.41}$$

$$\Psi_q = L_q i_q \tag{3.42}$$

and for a PMSM the d and q inductances are assumed equal, i.e. $L_d = L_q$.

By substituting (3.41) and (3.42) into (3.40) the torque equation for a PMSM with surface mounted magnet becomes

$$T = \frac{m}{2}p\Psi_{pm}i_q \tag{3.43}$$

3.4.1 Machine-side converter controller

The machine side converter is in this thesis treated as a lossless linear amplifier. Hence, the voltage reference output of the controller equals the converter voltage. As seen in (3.43), for a PMSM the torque is proportional to the current and since modern inverters acts as controllable voltage sources, there is a need to derive the transfer function from voltage to current of the machine in order to be able to control the torque and by extension the power [31].

In order to simplify the analysis (3.39) is transferred to the Laplace domain. With some algebraic rearranging (3.39) becomes

$$\boldsymbol{u}_{dq} - \boldsymbol{e}_{dq} = \big(R_s + s(L-M) + j\omega_r(L-M)\big)\boldsymbol{i}_{dq} \tag{3.44}$$

The transfer function from voltage to currents is therefore

$$\frac{\boldsymbol{i}_{dq}}{\boldsymbol{u}_{dq} - \boldsymbol{e}_{dq}} = \frac{1}{R_s + s(L-M) + j\omega_r(L-M)} = G_m(s) \tag{3.45}$$

The heart of the controller algorithm is the current controller, which is here derived using the approach described in [31]. The open-loop transfer function of the control law is given by

$$\boldsymbol{u}_{dq} = F_c(s)\boldsymbol{i}_{dq,ref} + j\omega_r\big(\hat{L} - \widehat{M}\big)\boldsymbol{i}_{dq} + \hat{\boldsymbol{e}}_{dq} \tag{3.46}$$

where $j\omega_r\big(\hat{L} - \widehat{M}\big)\boldsymbol{i}_{\boldsymbol{dq}}$ is the estimated cross coupling term and $\hat{\boldsymbol{e}}_{\boldsymbol{dq}}$ is the estimated back-EMF. Observe that both these both terms are speed-dependant. $F_c(s)$ is the PI part of the controller defined as

$$F_c(s) = K_p + \frac{K_i}{s} \tag{3.47}$$

By comparing the original machine voltage equation given in (3.39) and the open-loop controller output voltage equations, (3.46), with the assumption of perfect knowledge of the system, the transfer function from current reference to actual current becomes

$$\begin{aligned} R_s\boldsymbol{i}_{dq} + s(L-M)\boldsymbol{i}_{dq} + j\omega_r(L-M)\boldsymbol{i}_{dq} + j\omega_r\Psi_{pm} \\ = F_c(s)\boldsymbol{i}_{dq,ref} + j\omega_r(\hat{L} - \widehat{M})\boldsymbol{i}_{dq} + \hat{\boldsymbol{e}}_{dq} \end{aligned} \tag{3.48}$$

$$\frac{\boldsymbol{i}_{dq}}{\boldsymbol{i}_{dq,ref}} = \frac{1}{s(L-M)+R_s}\, F_c(s) = G_m'(s)F_c(s) \tag{3.49}$$

where $G_m'(s)$ is a reduced machine model without back-EMF and cross coupling terms. With the controller setup in a closed-loop transfer function, i.e. the input for the PI controller is the difference between the reference values and the real current $(\boldsymbol{i}_{dq,ref} - \boldsymbol{i}_{dq})$, the system can be shaped as a first order low-pass filter. Figure 3.11 illustrates the machine current controller using block diagrams.

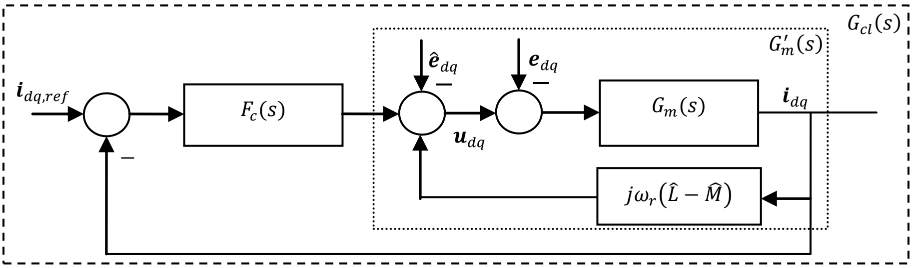

Figure 3.11 Block diagram of the machine current controller structure in a closed-loop configuration

For a given bandwidth for the closed-loop system, the controller parameters K_p and K_i can be determined. The closed loop system transfer function is

$$G_{cl}(s) = \frac{i_{dq}}{i_{dq,ref}} = \frac{F_c(s)G'_m(s)}{1 + F_c(s)G'_m(s)} = \frac{\alpha_{cc}/s}{1 + \alpha_{cc}/s} \tag{3.50}$$

where α_{cc} is the selected bandwidth of the closed-loop system. With some algebraic manipulation (3.50) can be rewritten as

$$F_c(s) = \frac{\alpha_{cc}}{s} G'^{-1}_m(s) = \alpha_{cc}(L - M) + \frac{\alpha_{cc} R_s}{s} = K_p + \frac{K_i}{s} \tag{3.51}$$

Figure 3.12 presents the normalized current response to a step input. The bandwidth of the system is chosen to 1000 rad/s. As seen the controller behaves as desired; the actual current follows its reference value with the desired bandwidth without overshooting.

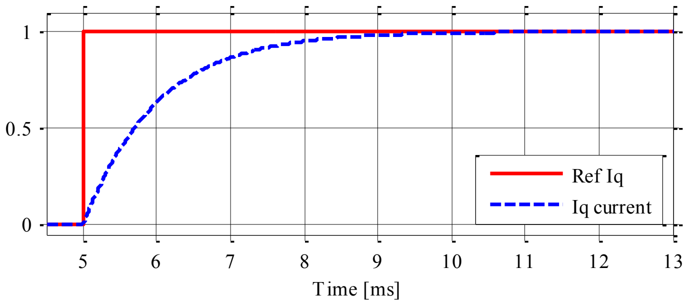

Figure 3.12 Normalized current response from a step input step to the controller

The controller has been derived under the assumption that the converter is able to generate any kind of voltage at its terminals. A potential problem when using an integrator term in the control algorithm is the windup phenomenon which occurs in the case of controller saturation, i.e. the controller request a voltage greater than the converter rating. A method to cope with this issue is to limit the error signal input to the integrator in the event of saturation. The unlimited reference voltage is calculated as

$$\boldsymbol{u}_{dq,ref} = K_p \boldsymbol{e}_{rr} + K_i \frac{\boldsymbol{e}_{rr}}{s} + j\omega_r\left(\hat{L} - \widehat{M}\right)\boldsymbol{i}_{dq} + \hat{\boldsymbol{e}}_{dq} \tag{3.52}$$

where

$$\boldsymbol{e}_{rr} = \boldsymbol{i}_{dq,ref} - \boldsymbol{i}_{dq} \tag{3.53}$$

In case of saturation, the limited dq-voltage output from the controller can be calculated as

$$\boldsymbol{u}_{dq,lim} = K_p \boldsymbol{e}_{rr,lim} + K_i \frac{\boldsymbol{e}_{rr,lim}}{s} + j\omega_r\left(\hat{L} - \widehat{M}\right)\boldsymbol{i}_{dq} + \hat{\boldsymbol{e}}_{dq} \tag{3.54}$$

Subtracting (3.52) from (3.54) gives the new error signal to the integrator part, i.e.

$$\boldsymbol{e}_{rr,lim} = \boldsymbol{e}_{rr} + \frac{U_{dq,lim} - U_{dq,ref}}{K_p} \tag{3.55}$$

where $\boldsymbol{u}_{dq,lim}$ is equal to $\boldsymbol{u}_{dq,ref}$ when the converter is operating in its linear range. For $\boldsymbol{u}_{dq,ref}$ values greater than then maximum voltage that can be delivered from the converter $\boldsymbol{u}_{dq,lim}$ should be forced equal to the convert rating.

Discrete form of the Machine-side converter controller

In actual applications, the controller must be implemented in a digital system and for this reason the controller needs to be discretized. In order to derive the controller in the discrete-time domain the following assumptions are made:

- The back-EMF of the machine changes slowly and can therefore be considered to be constant over one sampling period, T_s,

$$\frac{\boldsymbol{e}_{dq}(k+1) + \boldsymbol{e}_{dq}(k)}{2} = \boldsymbol{e}_{dq}(k) \tag{3.56}$$

- The current variations are linear

$$\text{avg}(\boldsymbol{i}_{dq}(k)) = \frac{\boldsymbol{i}_{dq}(k+1) + \boldsymbol{i}_{dq}(k)}{2} \tag{3.57}$$

- The voltage delivered from the converter is on average equal to the reference value

$$\text{avg}(\boldsymbol{u}_{dq}(k)) = \boldsymbol{u}_{dq,ref}(k) \tag{3.58}$$

Using these assumptions, the control algorithm in the discrete time domain can be written as

$$\boldsymbol{u}_{dq,ref}(k) = K_p\left(\boldsymbol{i}_{dq,ref}(k) - \boldsymbol{i}_{dq}(k)\right) + \boldsymbol{I}_{nt}(k) + \boldsymbol{A}_W(k) + \boldsymbol{u}_{ff}(k) \tag{3.59}$$

Where $\boldsymbol{u}_{ff}(k)$ is the feed forward term including the cross coupling and the back-EMF, $\boldsymbol{I}_{nt}(k)$ and $\boldsymbol{A}_W(k)$ are the integrator part and integrator anti-windup part respectively. $\boldsymbol{I}_{nt}(k)$ is defined as

$$\boldsymbol{I}_{nt}(k+1) = \boldsymbol{I}_{nt}(k) + K_i T_s(\boldsymbol{i}_{dq,ref}(k) - \boldsymbol{i}_{dq}(k)) \tag{3.60}$$

and $\boldsymbol{A}_W(k)$ is defined as

$$A_W(k+1) = A_W(k) + \frac{K_i T_s}{K_p}(U_{dq,lim}(k) - U_{dq,ref}(k)) \tag{3.61}$$

where T_s is the discrete time step.

Figure 3.13 shows both the discrete and continuous current controllers' step responses when the bandwidths of the controllers are set to $1000\ rad/s$ and the sampling frequency (f_s) of the discrete controller is set to $5\ kHz$. The discrete controller behaves as desired as it follows the reference with the desired bandwidth. The difference between the continuous and discrete controller is due to the step changes in the output voltage from the discrete controller. This result in a higher voltage output from the discrete controller compared to the continuous controller during the transient period.

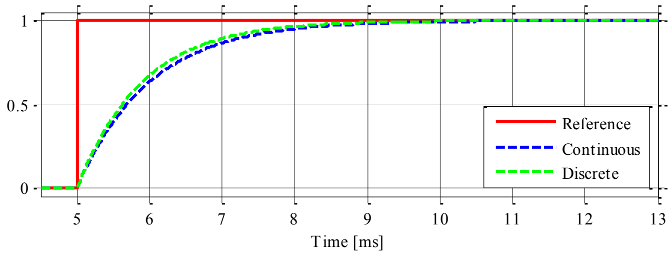

Figure 3.13 Normalized current response from a step input to both the continuous and discrete controllers.

The sampling frequency sets the limit of the maximum allowed bandwidth of the discrete controller [32]. Figure 3.14 presents the step responses of the discrete controller with different bandwidth with respect to the sampling frequency. As can be seen the too high bandwidth result in an unstable system.

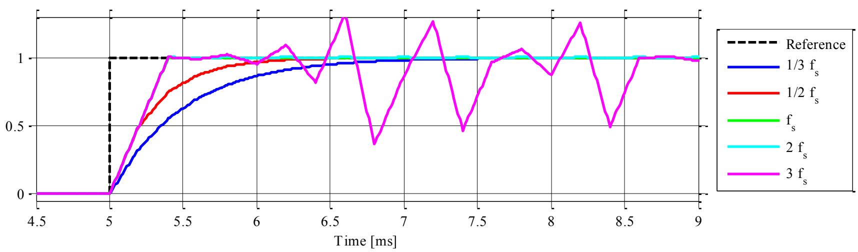

Figure 3.14 Normalized current responses from a step input to the controller using different bandwidth in relation to the sampling frequency

The current controller is an inner loop controller and the outer loop is the torque controller which determines the q-current reference. The torque controller is an open-loop control, where the current reference is calculated through a look-up table.

The lookup table correlates the machine speed to optimum generator torque, as the look-up table is derived from the aerodynamic properties of the turbine rotor. The machine d-current reference is in this thesis constantly set to zero in order to minimize the stator currents, as field-weakening operation is not of interest in this thesis. More information regarding field-weakening operation can be found in [31].

3.4.2 Grid-side converter

The controllers for the machine-side and the grid-side converter are very similar in their structure as the system seen by the controller consists of similar components. The grid voltages can be seen as the back-EMF and the resistive and inductive part of the machine corresponds to the in series RL filter installed between the converter and the grid. Instead of rotor position, a Phase-Locked Loop (PLL, described in Section 0) is used to track the phase angle of the grid voltage vector, to enable synchronization between the converter and the grid. In this thesis the grid rotating reference frame is aligned in accordance with the machine reference, so that q-current represents active current and d-current is the reactive current for both the machine and the grid-side converter.

By using the method described in Section 3.4.1 the final expression for the grid converter controller becomes identical to (3.59), but with the difference that the feed forward part $\boldsymbol{u}_{ff}(k)$ consists of

$$\boldsymbol{u}_{ff}(k) = \boldsymbol{u}_{dq,grid} + j\omega_g L\boldsymbol{i}_{dq} \tag{3.62}$$

where $\omega_g = 2\pi f_{grid}$ and L is the filter inductance and $\boldsymbol{u}_{dq,grid}$ is the grid voltage in the rotating reference frame (see Figure 3.10). The bandwidth and sampling frequency are kept as for the machine-side controller, i.e. a bandwidth of $1000\,rad/s$ and a sampling frequency of $5\,kHz$. Using the power references provided by the DC-link voltage controller together with the measured grid voltage, the current references can be calculated by the use of the electrical power equations in the rotating system. The electrical power equations in the rotating system are

$$P = u_d i_d + u_q i_q \tag{3.63}$$

$$Q = -u_d i_q + u_q i_d \tag{3.64}$$

During balanced conditions together with a perfect alignment of the rotating reference frame the d component of the grid voltage is zero. The current references for the current controller can therefore be calculated as

$$i_{q,ref} = \frac{P_{ref}}{u_{q,grid}} \tag{3.65}$$

$$i_{d,ref} = \frac{Q_{ref}}{u_{q,grid}} \tag{3.66}$$

where the active power reference P_{ref} is calculated from the outer DC-link voltage controller.

DC-link voltage controller

The purpose of the grid-side converter is to deliver energy from the DC-link to the grid. The energy stored in the DC-link capacitor C_{dc} can be express as

$$W_{dc} = C_{dc}\frac{U_{dc}^2}{2} \tag{3.67}$$

A change in the stored energy in the DC-link is caused by a power offset between the generator power and the power delivered to the grid. Ideally, the power produced by the generator should without any delay be delivered to the grid by the grid-side converter, as such the DC-link energy should in the idealized case remain constant. However, in a real system there are always delays and other disturbance, so in order to make the system more redundant a DC-link voltage controller is added to cope with any energy offsets that will occur. The total active power reference is calculated as

$$P_{ref}(k) = K_{pW}\left(\frac{U_{dc}^2(k) - U_{dc.ref}^2(k)}{2}\right) + I_W(k) + P_{gen}(k) \tag{3.68}$$

where

$$I_W(k+1) = I_W(k) + T_s K_{iW}\left(\frac{U_{dc}^2(k) - U_{dc.ref}^2(k)}{2}\right) \tag{3.69}$$

and $P_{gen}(k)$ is the feed-forward information of the generator power (see Figure 3.10). The voltage controller error signal is chosen to use the voltage squared instead of using the directly measured voltage value as it makes the controller independent of the operation point [33]. The controller parameters K_{pW} and K_{iW} should for purely capacitive DC-link, according to [34], be chosen as

$$K_{pW} = \alpha_w C_{dc} \tag{3.70}$$

$$K_{iW} = 0 \tag{3.71}$$

The DC-link voltage controller is cascade connected with the current controller and as a rule of thumb, the outer controller should much slower than the inner controller, i.e. the bandwidth of the energy controller should be chosen to be $\alpha_w \leq 0.1\alpha_{cc}$. As such, the voltage controller bandwidth is chosen to $100\ rad/s$ in this thesis. The reactive power reference is manually chosen to zero in this thesis due to the Swedish grid code which state that a should never produce any reactive power [11].

Figure 3.15 shows the controller behavior for $0.25\,p.u.$ steps in the power feed-forward term (P_{gen}) at $50\,ms, 200\,ms, 300\,ms$ and $400\,ms$ respectively. At $500\,ms$ there is a $0.05\,p.u.$ stepwise increase in the DC-link voltage. As can be seen the controller behaves as desired; the output power follows the feed-forward term and adjusting the DC-link voltage to the nominal. The large variation in the DC-link voltage will not be as severe during normal operation for a wind turbine as the feed-forward power fluctuations are much slower and are not step shaped.

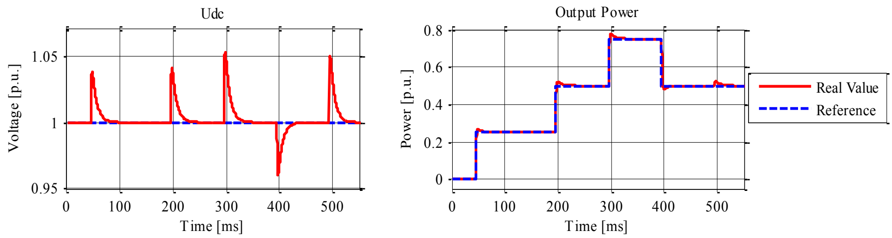

Figure 3.15 Controller response to step increases in the feed-forward power terms and DC voltage.

Phase-Locked Loop

The Phase-Locked Loop, PLL, which tracks the angle of the grid voltage vector, is used as transformation angle for the rotating reference frame. The equations that governs the PLL are [35]

$$\omega_{grid} = 2\pi f_{nom} + K_i \int \boldsymbol{e} \partial t \tag{3.72}$$

$$\theta = \int (\omega_{grid} + \boldsymbol{e} K_p)\, \partial t \tag{3.73}$$

where $\boldsymbol{e}$ is the error angle, which in small signals coincides with the normalized d-component of the grid voltage, i.e. $\boldsymbol{e}$ is calculated as

$$\boldsymbol{e} = -\frac{U_d}{\text{abs}(U_d + jU_q)} \tag{3.74}$$

The parameters K_p and K_i can be chosen using the bandwidth of the PLL, α_{PLL}, as described in [35] to be

$$K_p = 2\alpha_{PLL} \tag{3.75}$$

$$K_i = \alpha_{PLL}^2 \tag{3.76}$$

The selection of the PLL bandwidth is a tradeoff between harmonic rejection and response time, where a low bandwidth leads to better harmonic rejection at the cost of a slower response time. There are methods to improve the performance of the

PLL with regards of speed and harmonic rejection as described in [36]. However, since the wind turbine grid codes do not require grid support during faults, it is sufficient to only monitor the positive sequence. As such, there is no motivation to implement the fast responding PLL.

The discretized forms of (3.72) and (3.73) are

$$\omega_{grid}(k) = 2\pi f_{nom} + I_{PLL}(k) \tag{3.77}$$

$$\theta(k+1) = \theta(k) + T_S\omega_{grid}(k) + T_S K_p \boldsymbol{e}(k) \tag{3.78}$$

where the integrator part I_{PLL} is defined as

$$I_{PLL}(k+1) = I_{PLL}(k) + T_S K_i \boldsymbol{e}(k) \tag{3.79}$$

where T_S is the sampling time of the PLL. Figure 3.16 presents the PLL response to a phase angle jump occurring at time 0.02 seconds and an unbalanced grid fault at 0.5 seconds. In Figure 3.16 two responses are presented, one with a bandwidth of 3 Hz and the other at 10 Hz.

As can be seen from the figure, the higher bandwidth PLL reach the stable operation point after the phase angle jump faster. However, the negative sequence introduced by the grid fault affects the PLL with the higher bandwidth more as the oscillating component have larger amplitude compared with the amplitude of the oscillating component in the lower bandwidth PLL. For this reason, the choice of a 18.85 rad/s (3 Hz) bandwidth for the PLL has been made for this thesis.

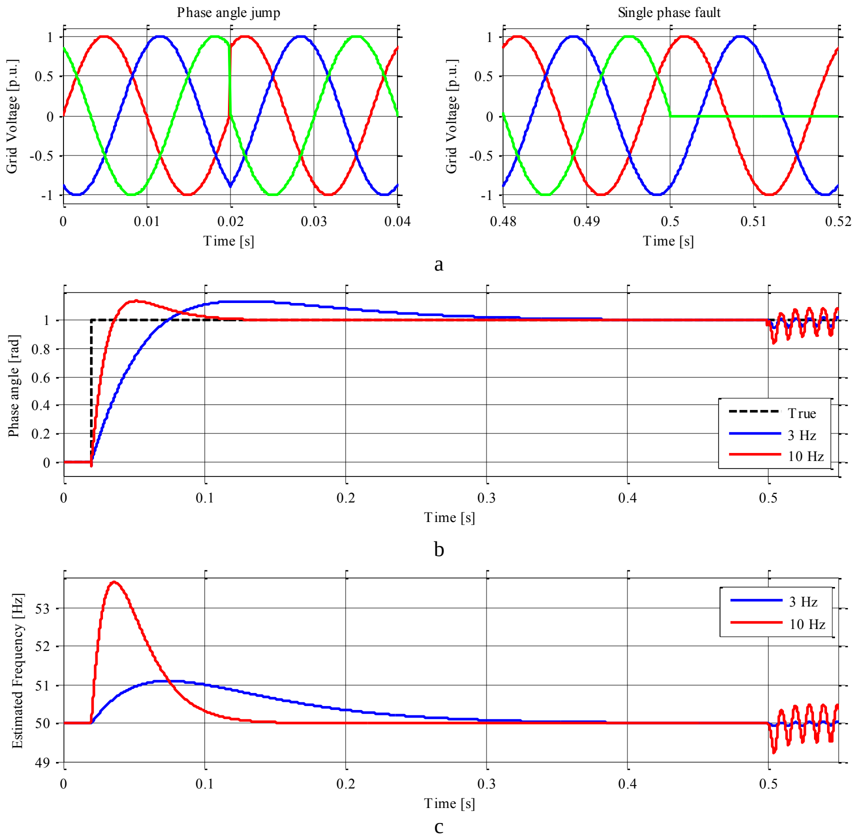

Figure 3.16 Behavior of a PLL with a 3 Hz and 10 Hz bandwidth exposed to a phase angle jump at 0.02 second and a single phase fault at 0.5 second. Figure a presents the grid three phase voltages, figure b presents the phase angle, and figure c presents the estimated grid frequency.

DC-link overvoltage protection

During grid faults or loss of synchronization, the energy produced by the wind turbine cannot be delivered to the grid. During large balanced voltage dips the grid-side converter is only partly able to deliver power to the grid due to current saturation caused by the low voltage. As in typical installations the DC-link energy storage capability is extremely limited, the power unbalance between the generated power and power delivered to the grid will quickly overcharge the DC-link, resulting in system damage. Due to the small time constant of the DC-link (typically in the ms range), within this short time-span the machine controller might not be fast enough to reduce the power production: even if possible, a too large stepwise reduction in the generator torque would cause excessive high mechanical stresses. As such, there is a need of an additional protection system: the DC-crowbar. It consists of a resistive load connected in parallel with the DC-link which can be connected through a switch, see Figure 3.10. The DC-crowbar is typically designed to be able to dissipate a limited amount of energy, i.e. it has a limited amount of time during which it is can be connected. Preferably, the grid faults are cleared during this time otherwise the turbine energy production must cease. As such, the DC-crowbar should therefore be dimensioned according to the grid code requirements.

The DC-link overvoltage protection is based on a fast acting hysteresis controller which activates the DC-crowbar when the DC-link voltage reaches a pre-defined threshold. Once the crowbar has drained the DC-link below the pre-set voltage level the crowbar is disconnected. If the error is still unresolved the voltage level will increase once more and thus reactivating the DC-crowbar. Figure 3.17 shows the operation of the DC-crowbar where the upper limit is set to 1.10 p.u. voltage and the lower limit at 1.05 $p.u.$ As seen the DC-crowbar behaves as typical hysteresis controlled entity.

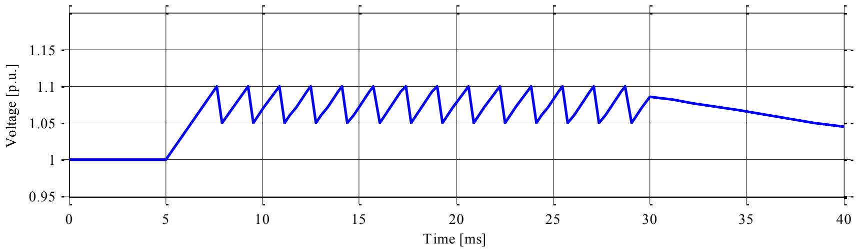

Figure 3.17 The DC-link voltage during unbalance power flow leading to overvoltage. The DC-crowbar activates at 1.1 p.u. DC-link voltage and disconnect at 1.05 p.u.

3.5 Simulation and results

In this section all models described in the previous sections are connected in cascade according to Figure 3.10. As such, the complete system model can be seen as a single large system model with mechanical torque as input and power delivered to the grid as output. However, wind turbine torque measurements are only sparsely available. As such, a more convenient quantity to use is the turbine rotor speed which is more commonly available for wind turbine systems. The system model is then complemented with an unrestrained closed-loop first-order speed controller, which ensures that the reference speed is reached by supplying an adequate torque. Figure 3.18 illustrates the simulation setup used for a typical operation simulation.

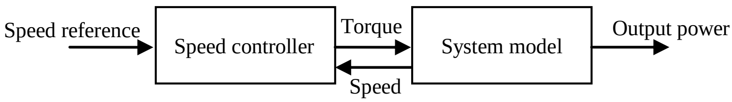

Figure 3.18 Simulated and measured power delivered to the grid

The generator torque reference is also calculated from the turbine speed through a look-up table.

3.5.1 Typical operation

The simulation results presented here use a measured rotor speed as input, where the measurement was taken from an actual 4.1 MW full power converter direct-drive turbine with a PMSG which has a converter power rating of 4.6 MVA. Figure 3.19 shows the wind speed measured at the nacelle and its corresponding normalized rotor speed. This measured rotor speed is used as input to the simulation model.

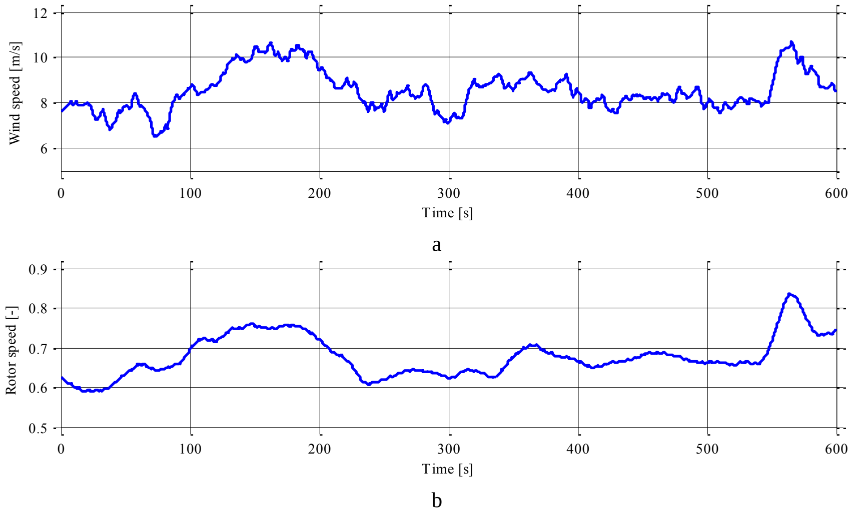

Figure 3.19 Figure a presents measured wind speed, and its corresponding rotor speed is presented in figure b, which is used as the input to the simulation model.

Figure 3.20 shows the simulated output power obtained using the system model presented in this section. The obtained power is compared with the one measured in the actual installation. Observe that the simulated power is slightly higher compared to with the measured one. This is due to the fact that the simulated model does not account of all losses in the system. However, it is important to stress that to develop more accurate models with respect to losses is out of scope for this thesis.

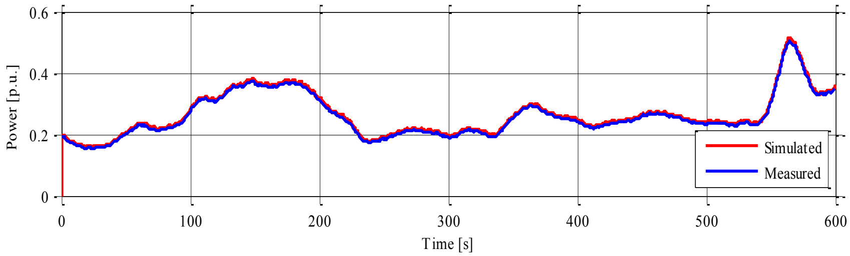

Figure 3.20 Simulated and measured power delivered to the grid

Figure 3.21a shows in more detail the simulated machine controller reaction to the wind gust presented in Figure 3.19 at 540 seconds. The increase in rotor speed causes the machine controller to request more power from the generator. This is the time period of this simulation which contains the highest power derivative, but as can be seen from Figure 3.21b the grid-side controller is able to maintain the DC-link voltage at the desired level even during this time period. Unfortunately there is no measurement available for the DC-link voltage level.

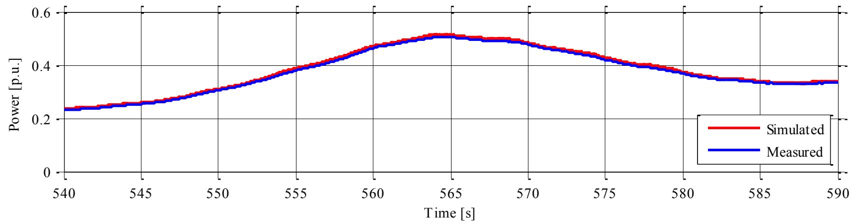

a

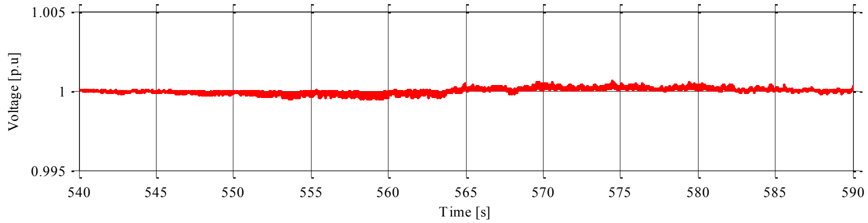

b

Figure 3.21 A wind gust increases the power output, presented in figure a, while the controller is able to keep the DC-link voltage at the desired level, presented in figure b.

As can be seen, the simulated turbine produces approximately the same amount of power as the real turbine measurements for all the simulated inputs.

3.5.2 Low voltage ride through simulation

The complete system model considered in the previous section is used to verify the low voltage ride through capability of the full power converter turbine. The chosen low voltage ride through profile is the one considered by the Swedish TSO (Svenska Kraftnät), see Figure 2.5. Due to the large rotor inertia and the comparably short simulation time, the turbine rotational speed is assumed to be constant during the entire low voltage ride through time period. During the low voltage section (from 0.1s to 0.85s), all the active power delivery to the grid is stopped while the generator continues to operate. The chosen pre-fault operation point is at rated power in order to make the grid code fulfillment the most difficult. Due to this, even though not stated in the Swedish grid code (but in others), 1 p.u. reactive current is injected to the grid during the fault to verify that the full power converter wind turbine is able to provide grid support during low voltage ride through. Figure 3.22 presents the normalized grid voltage at the turbine terminal during the low voltage ride through simulation.

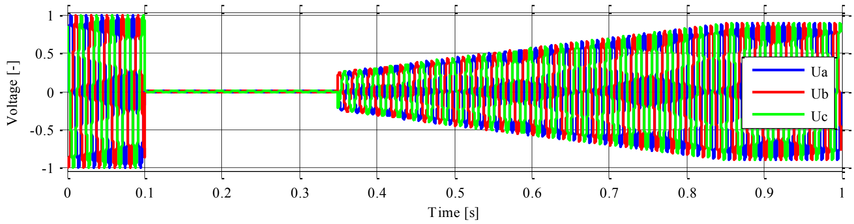

Figure 3.22 Normalized grid voltage during low voltage ride through

Figure 3.23 presents the power and current injected to the grid during the fault. The grid side converter is partly overrated for the turbines rated power, which results in a current lower than rated during pre-fault conditions. This enables more grid support capabilities during grid faults.

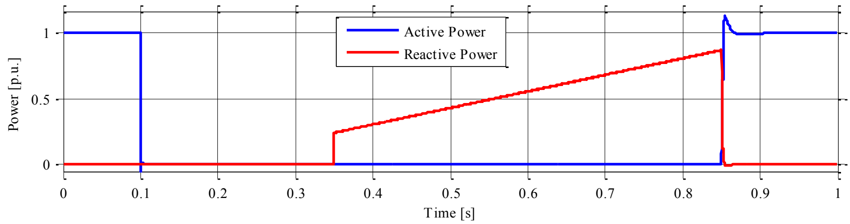

a

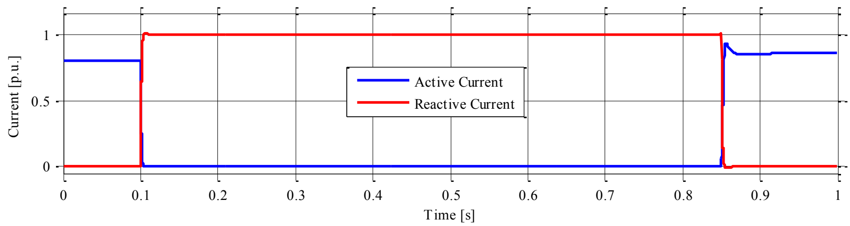

b

Figure 3.23 The grid side converters response during a low voltage ride through. The controller is set to inject one p.u. reactive current to the grid during the grid fault.

Since the turbine speed is unvaried, the generator power will remain constant during the low voltage ride through, resulting in an increase of the DC-link voltage, see Figure 3.24. The increase in voltage will at the pre-specified level activate the DC-crowbar as protection. This will keep the voltage level at an acceptable level.

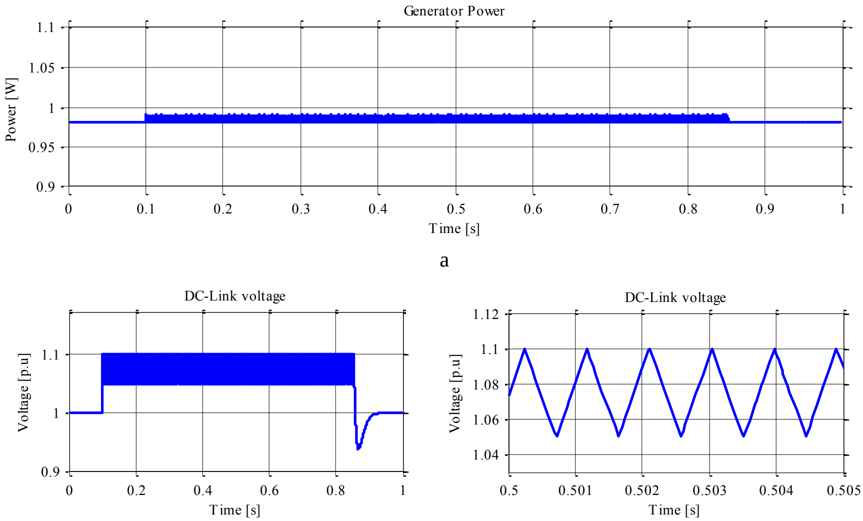

b

Figure 3.24 Figure a present the generator produced power, which remains constant during the fault. Figure b presents the DC-link voltage during the fault, which varies as the DC-crowbar switched on and off during the fault.

Since the fault duration is within the operational time of the DC-crowbar the turbine is able to resume operation once the grid voltage returned to a voltage level which is of the normal operation rage.

3.6 Summary

This chapter presented analytical models of the electrical parts of a full power converter wind turbine with a PMSM as generator, where each part has been modeled as a standalone models. Since the controllers are to be implemented on digital controllers, the controller algorithm has been converted from the continuous time domain to the discrete time domain. All models have been interconnected to form the complete wind turbine system model and simulated. The simulation result has been compared to real turbine measurements with acceptable agreement. The system model has also been used to simulate the low voltage ride trough capabilities of the full power converter wind turbine. As expected, the simulation results have shown that full power converter turbines are able to cope with the low voltage ride through, thus there will be more full power converter turbines in the future.

The system model can be used for more than investigations of the impact of grid disturbance. The impact of any internal fault on other parts of the turbine can also be studied using the system model. The following chapter presents a brief overview of fault that can occur within a wind turbine.

Chapter 4

Overview of faults in wind turbines

This chapter presents a brief overview of the most common component failures that can occur in wind turbine systems. A brief explanation to the cause of the failure is also presented.

4.1 Introduction

A critical aspect for energy production units is the cost of energy. In the case of wind energy, the cost is mainly related to the initial investment and the cost of maintenance. Good maintenance procedures should provide more hours of operation which in turn will reduce the total cost of energy. By utilizing fault detection systems the maintenance can be made more efficient. The idea of utilizing a fault detection system is to:

- Minimize reparation costs and loss of power production.

- Reduced maintenance cost as it can be need-based rather than time-based.

- Improved capacity factor by better scheduling of maintenance during less windy seasons.

An additional benefit of fault detection systems is the generated measurement data which can be used to improve the design of the next generation turbines.

To make the fault detection system effective, the alterations caused by a failed component in the turbine characteristics needs to be known. Using this knowledge, key quantities to be monitored can be identified.

According to [37], the most common wind turbine sub-assemblies to fail for variable-speed turbine types (in descending order) are:

- Electrical system
- Rotor (i.e. blades and hub)
- Converter (i.e. electrical control, power electronics)
- Generator
- Hydraulics
- Gearbox

However, this does not completely agree with [38] which has studied a different population of wind turbines.

Figure 4.1 presents the data presented in [38] which also includes the average downtime caused by each component failure.

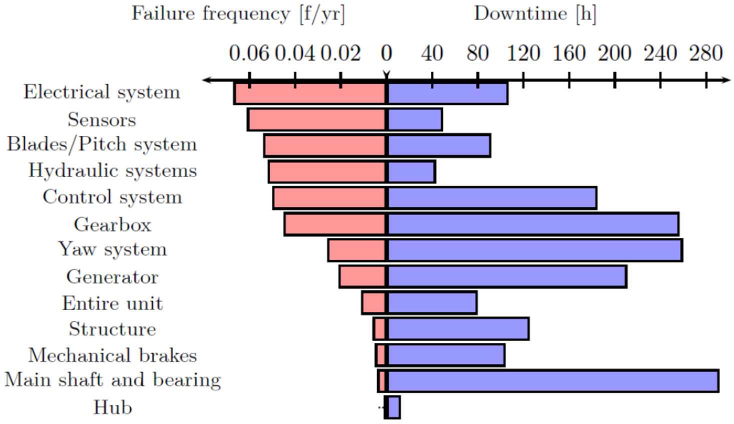

Figure 4.1 The average failure rate and downtime per sub-assembly and year in wind turbines, presented in [38].

As can be seen, both surveys presents the same sub-assemblies but with a small rearrangement in the order of failure rate. However, as can be seen from Figure 4.1 the difference between the failure rates is small among the sub-assemblies tend to fail the most. It can also be seen in Figure 4.1 that the downtime caused by failures of the different subsystems varies more than the failure rates. The most critical sub-assemblies from a reliability perspective are therefore the ones which have both a high failure rate and a long downtime, such as the gearbox (see Figure 4.1).

In [37], it is also stated that large wind turbines have lower reliability compared to small turbines and the failure rate of generators used for direct drive is up to double of geared solutions. However, the generator failure rate can be improved by the use of permanent magnet instead of electrical excitation from rotor windings. The failure rate of the power electronics is higher for wind applications than for other industries [37]. Some of these failures will be described more in detail in this chapter, together with a brief explanation of the causes.

4.2 Mechanical fault

Most of the wind turbine components can be seen as part of either the mechanical system or a part of the structure. Examples of mechanical subassemblies are the drive-train and the blades; the foundation and the tower are examples of structure. The root cause of mechanical component failure is typically due to several reasons in various combinations. Examples are fatigue, corrosion, manufacturing errors, assembly errors, and ambient condition. The ambient condition includes humidity, temperature, and dust. It also includes the weather condition, both for normal and extreme events such as storms and lightning strikes. Damage to the blades needs to be detected early as operating with broken blades can cause secondary damages to the entire wind turbine [1]. The blades also represent a considerable amount of the initial cost of a turbine while being costly and time consuming to repair. This motivates the need for an efficient condition monitoring system for the blades. As the blade consists of layers made from various materials, where all materials tend to have an equal failure tendency. As such, there is not a typical weak spot in the blade architecture with a higher failure rate. The failures are mainly due to creep fatigue and corrosion fatigue in the blades, and the fault characteristic is dependent on the faults location on the blade. Detecting a blade fault is a non-trivial issue as other phenomena can cause similar characteristic behavior. Ice on the rotor as well as dead insects alter the rotor blade surface in a similar manner as cracks and delamination[1], which all have an effect on the rotor aerodynamic efficiency. Figure 4.2a summarizes some of the faults which can occur to a rotor blade and Figure 4.2b shows a photo of a rotor blade with cracks in the gelcoat and some splitting along its fibers [39].

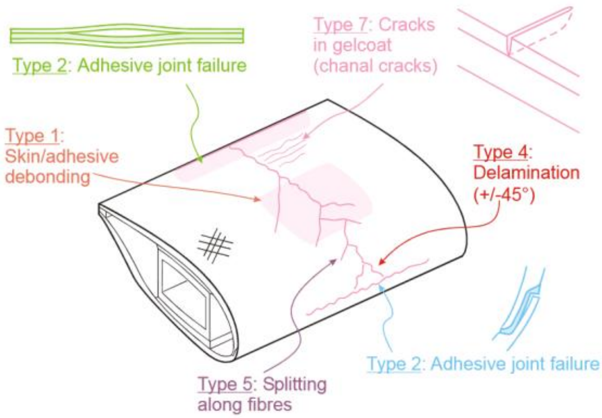

a

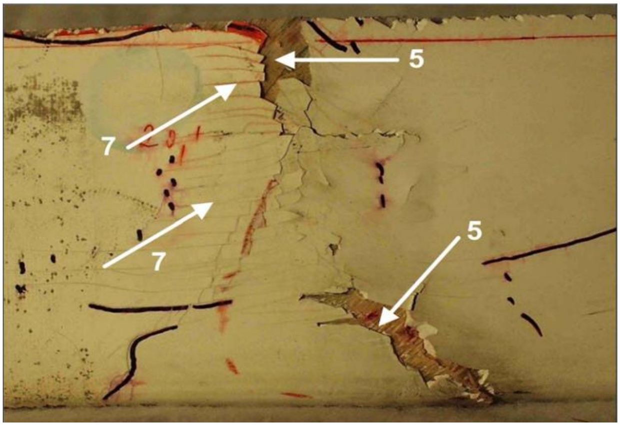

b

Figure 4.2 Examples of rotor damages, presented in [39]

There are specialized methods for detecting blade faults, where the different methods use different techniques such as acoustic emissions, thermal imaging, ultra-sonic methods, and modal-analysis. A more detailed description of the different methods can be found in [40]. In the same reference the authors discuss the applicability of similar methods to investigate failures in the structure of the tower.

In connection to the blades is the pitch-system in which the event of failure can put the turbine in a critical situation. A faulty pitch-system can cause severe unbalanced loading on the rotor, leading to secondary damages to the entire wind turbine. The worst case situation for the pitch-system to fail is during wind speeds greater than the cut-out level. As a result the turbine may be unable to shutdown as the pitch-system cannot be used to turn the rotor blades in order to achieve aerodynamic braking [1].

Within the drive-train, gearbox failure for the indirect drive is one of the most common components to fail [41]. Gear tooth wear is one of the reasons of failure, but the most common is bearing failure within the gearbox. A multistage gearbox includes several bearings, but it is only some specific bearings that tends to fail [1]. There are methods developed to detect bearing faults which use vibration sensors; to increase the reliability of the fault detection, acoustic measurements can also be included [1]. The gearbox issue can solved by choosing a direct-drive solution, but at the expense of a larger multi-pole and more complex generator. However, statistics have shown that this does not solve the issue completely as the direct drive turbines have approximately equal failure rate to that of indirect drives. This is due to the higher failure rate of the generator and the power electronics for direct drive turbines [41]. However, the total downtime may still be reduced as the downtime caused by generator and power electronic failures are lower compared to gearbox failures, see Figure 4.1.

4.3 Power electronic failure

The power electronic components represent a comparably small part of the initial wind turbine cost, but it accounts for a considerate amount of the failures [1]. However, since the mean time to repair of a power electronic component is low, the contribution to the total down time is comparatively low despite the higher fault occurrence. The cause of semiconductor failure can be due to several reasons. Some examples are electrical overstress, electrostatic discharge, contamination and various sorts of mechanical stress. The mechanical failures are typically related to thermal cycling caused by varying electrical loading. The different materials used in the packaging have different thermal expansion coefficients leading to mechanical wear and fatigue [1]. Figure 4.3a presents a principle sketch of bond-wire liftoff due to cracks created from thermal cycling [42]. Figure 4.3b shows a photo of bond-wire crack [43].

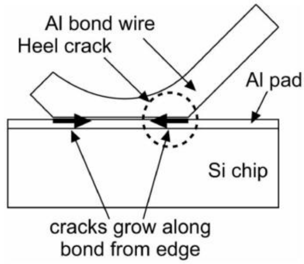

a

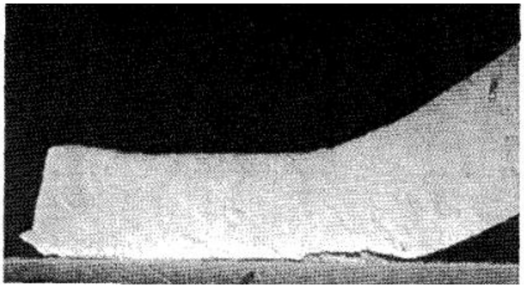

b

Figure 4.3 Bond-wire cracks due to thermal cycling. Figure a can be found in [42] and figure b in [43]

To model the breakdown mechanism requires detailed multi-disciplinary sub-models such as electro-thermal and thermo-mechanical[42]. In [42] the authors review and compare different modeling methods for various power electronics faults. The authors also discuss different possibilities of condition monitoring to assess the remaining lifetime of the units. In essence, they conclude that the research area is in its infant stage and more research is needed before an effective condition monitoring system will be implemented in a converter system (regardless of application).

A fault in a power semiconductor for a two-level converter will result in an open-circuit fault, a short-circuit fault or an intermittent gate-misfire depending on which part of the component has failed [44]. In [44] the authors review different methods used to detect a failure within a power semiconductor, where each method only focuses on a specific type of fault. An open-circuit fault will not cause any direct damage but will cause the controller to become unstable which in turn can cause secondary damage. A short-circuit fault will most likely cause too high currents which makes it more time crucial to detect compared to the open-circuit fault. As a result, the short-circuit fault detection is typically hardware implemented and designed as a protection system rather than a condition monitoring system. The intermittent gate-misfire fault will either effect the system as an open-circuit fault in the case of gate-fire inaction or it create a short-circuit fault in case of an unwanted gate-fire or due to the inability of gate-turnoff.

4.4 Generator faults

The generator, like the mechanical system, can be divided into smaller sub-assemblies: the stator circuit, rotor circuit, the mechanical drive-train, and the structure. The structure is the static construction which holds the physical machine together, for example the stator, and the active structure is the flux carrying part of the structure. The mechanical drive-train consists of the moving parts of the generator, where the most likely component to fail are the bearings [1]. For a PMSM, the rotor circuit only consists of parasitic components which ideally shouldn't carry any current. However, due to the alternating flux mainly produced by the stator currents there will be eddy currents in the rotor, both in the rotor laminate and in the magnets. When excessive, the eddy currents can cause magnet demagnetization. A failure in a magnet mounting results in the loss of a magnet which results in unbalanced machine which results in unbalanced current and torque ripple.

Failure in the stator circuit is mainly due to winding insulation failure. The insulation of the winding can deteriorate due to several reasons. Examples of such reasons are thermal, electrical, mechanical, or environmental issues [45]. Thermal stress accelerates the ageing process of the insulation, i.e. it decreases the operational lifetime of the insulation. A "rule of thumb" stated in [45] is that a 10° C increase in temperature reduces the insulation lifetime up to 50 %. However, simply ageing will not lead to insulation failure, it will only make the insulation more susceptible to other types of stresses which will cause failure. An electrical stress that can cause insulation failure is a too steep voltage transient, which should be considered when a machine is connected to an inverter due to the large voltage gradient created by the switching inverter [46].

Mechanical stress on the winding is caused by the physical movement of the windings, and if two or more windings touch, the friction can cause the insulation fail. The movement originates either from the forces created on a current-carrying conductor within a magnetic field or from some external source. The external source can be misalignment or a damaged bearing, as both creates vibrations. Figure 4.4 shows a photo of the stator which has lost some of the slot wedges which are used to restrict the movement of the winding [47].

Figure 4.4 A photo of a stator missing some slot wedges, presented in [47].

As the working environment of the electrical machine varies with its application, the possible ambient issues are then both location as well as application dependant. Example of possible issues could be contamination, dust, humidity, aggressive chemicals or salt. For coastal and offshore wind turbines, humidity and salt are typical issues. As for of thermal stress, the environmental stress will not cause a direct failure, but will rather cause indirect failures due to insulation deterioration.

An insulation failure might lead to a short circuit between the various parts of the machine. The short circuit may be phase-to-ground, phase-to-phase, coil-to-coil or a turn-to-turn fault. The phase-to-ground short circuit can permanently damage the mechanical structure of the stator. If so, the stator has to be replaced while the rotor can be reused. According to [45], the majority of the insulation faults originate from a small turn-to-turn fault. For a synchronous machine or a PMSM there will be an induced current in the loop created by the turn-to-turn fault. Even though the turn-to-turn fault is typically small compared to the complete phase winding for multi-pole machines, the induced current can be larger than rated current. This high current will produce excessive heat at the fault location in the machine, which will rapidly reduce the lifetime of the insulation of the neighboring conductors. As such, a turn-to-turn fault can initiate an avalanche like failure in the winding where more and more turns become short circuited. Once a turn-to-turn fault has occurred, it is typically only a short time period before the entire winding insulation has failed. It could be in the time range of minutes from initial fault to the failure of the entire winding [1]. Even though most winding faults originate from a turn-to-turn fault, there is no commercial method for the detection of a turn-to-turn fault.

4.5 Summary

This chapter presented a brief overview of some of the most common wind turbine failures. For some of the faults listed in this chapter, there are detection methods available on the market while other types of faults require more research in order to better understand the root cause of the failure. The most common generator failure of electrical nature is the turn-to-turn fault which can develop into other types of winding failure. Since the time window between the initial fault and the complete winding failure can be short, an effective protection system is needed to prevent further damage. For a PMSM, a current will be induced in the short-circuited winding as long as the machine is rotating. However, the current in the short circuited turns cannot be measured at the machine terminals. There is therefore a need for a detection method which is able to detect a turn-to-turn fault during operation in order to prevent further damage. The method should preferably only use already available data, thus reducing the need for additional sensors.

Chapter 5 presents how to model a PMSM with a turn-to-turn fault both analytically and using FEM. From the model results, a method for detecting a turn-to-turn fault using the three phase machine currents is proposed.

Chapter 5

Modeling of a PMSM with turn-to-turn fault

This chapter presents the derivation of the analytical model of a PMSM with turn-to-turn fault in the stator winding. The model is derived both in the stationary and in the synchronously rotating reference frame. The analytical model is verified using a finite element model. A method which indicates that a turn-to-turn fault has occurred is derived using the simulation results of both the healthy and faulty machine model.

5.1 Introduction

The use of PMSM is increasing thanks to the availability of strong magnets which enables machines with high torque density in relation to machine volume. However, the turn-to-turn faults pose a greater issue for the PMSM compared to the induction machine and the electrically excited synchronous machine. This is due to the inability to “turn off” the magnet, hence the only method to avoid inducing currents in the short-circuited turns is to completely stop the machine rotation and remove any voltage or current supplied to the machine. To stop the machine in wind turbine application results in a loss of energy production; however, it is still a better option to stop rather than to continue operation, since running a PMSM with a turn-to-turn fault may lead to a complete breakdown of the machine. It is therefore important to detect a turn-to-turn fault as early as possible, preferably when it occurs, to avoid further damage to the machine. However, since the induced current in the short-circuited turns cannot be measured at the machine terminal, there is a need for a method which is able to detect turn-to-turn faults only using the data available at the machine terminal.

This chapter presents an analytical three-phase model of the PMSM with turn-to-turn fault in the stationary reference frame, similar to the models described in [48-50]. The model is then transformed into the synchronously rotating reference frame using an adapted transformation matrix. The derived analytical model is then verified using a Finite Element Model (FEM). A flexible model is derived from the verified analytical models, where the flexible model is able to represent both the healthy and the faulty machine. The flexible model is during a simulation able to switch from the healthy model to the faulty model. Finally, the harmonic content of the stator current is studied both in the stationary and rotating reference frame in order to identify the possible quantities to monitor as an indication of a turn-to-turn fault. The harmonic content of the stator current during a turn-to-turn fault is compared to the harmonic content of the stator current when a stator magnet is removed in order to verify the difference between the two cases.

5.2 Analytical three-phase model of a PMSM with an turn-to-turn fault

As mentioned in Section 3.3, the single phase representation of a PMSM can be drawn as shown in Figure 5.1a; in the case of a turn-to-turn fault in a phase, the faulted phase can be represented by two parts, as in Figure 5.1b.

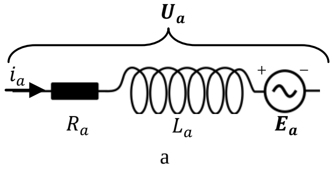

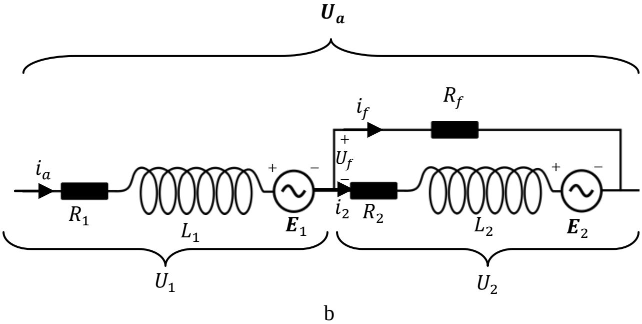

Figure 5.1 The single phase representation of healthy phase illustrated in figure a, and the single phase representation during a turn-to-turn fault illustrated in figure b.

The equations describing the faulty phase of the machine are

$$U_1 = R_1 i_a + L_1 \frac{di_a}{dt} + M_{21} \frac{d(i_a - i_f)}{dt} + M_{1b} \frac{di_b}{dt} + M_{1c} \frac{di_c}{dt} + \boldsymbol{E}_1 \tag{5.1}$$

$$U_2 = R_2\left(i_a - i_f\right) + L_2 \frac{d\left(i_a - i_f\right)}{dt} + M_{12} \frac{di_a}{dt} + M_{2b} \frac{di_b}{dt} + M_{2c} \frac{di_c}{dt} + \boldsymbol{E}_2 \tag{5.2}$$

where R_i is resistance (with $i = 1{,}2$ in reference to Figure 5.1b), L_i is self-inductance, $\boldsymbol{E}_i$ is back-EMF and M_{ij} is mutual inductance (where j can be either $1{,}2, b$ or c). R_f represents the contact resistance between the short circuited turns. As the physical structure of the machine has not been altered due to the turn-to-turn fault, it is still possible to write

$$U_1 + U_2 = U_a \;,\; R_1 + R_2 = R_a \;, U_2 = R_f i_f \tag{5.3}$$

Thus, the phase voltage U_a is given by

$$U_a = R_a i_a + L_a \frac{di_a}{dt} + M_{ab} \frac{di_b}{dt} + M_{ac} \frac{di_c}{dt} - \boldsymbol{E}_a - R_2 i_f - (L_{21} + L_2) \frac{di_f}{dt} \quad (5.4)$$

with the self-inductance L_a defined as the sum of the self-inductances from both part 1 and two 2 in Figure 5.1b, together with their mutual couplings, i.e.

$$L_a = L_1 + L_2 + 2L_{12} \quad (5.5)$$

Since the mutual coupling only depends on the flux from the other phases and on the number of turns in the receiving coil, it is assumed that the total mutual coupling is given by the sum of the couplings of the two parts. Hence the mutual couplings are given by

$$M_{ab} = M_{1b} + M_{2b} \text{ , } M_{ac} = M_{1c} + M_{2c} \quad (5.6)$$

The new short-circuit loop created by the turn-to-turn fault can be described as

$$U_f = 0 = \left(R_f + R_2\right) i_f - R_2 i_a + L_2 \frac{di_f}{dt} - L_{12} \frac{di_a}{dt} - M_{2b} \frac{di_b}{dt} - M_{2c} \frac{di_c}{dt} + \boldsymbol{E}_2 \quad (5.7)$$

where the negative sign on the mutual couplings is due to the selected direction for the current i_f being opposite to i_a (see Figure 5.1b). As the machine is assumed to be symmetrical the following simplifications can be made

$$R_a = R_b = R_c = R_s \quad (5.8)$$
$$L_a = L_b = L_c = L \quad (5.9)$$
$$M_{ab} = M_{ac} = M_{bc} = M \quad (5.10)$$

The modeled two parts of phase a (which occurred due to the turn-to-turn fault) are dependent. As such, a new parameter σ is introduced, where σ is defined as the ratio between the number of short-circuited turns and the total number of turns in the faulty phase.

$$\sigma = \frac{N_2}{N_a} \quad (5.11)$$

Using σ, the resistances $R_1$and R_2 can then be defined as

$$R_1 = (1 - \sigma)\mathrm{R_S} \quad (5.12)$$
$$R_2 = \sigma\mathrm{R_S} \quad (5.13)$$

For machines with a simple geometry, such as machines with one pole pair, all parameters of the faulty phase (such as R_1, L_1 and M_{12}) can be derived from the parameters of the healthy machine using σ (if saturation is neglected), as in the case of (5.12) and (5.13). Observe that this does not hold for machines with more complex geometry, where the inductance parameters must calculated using a reluctance grid (as described in Section 3.3.1) or by the use of a finite element software.

The generic three phase faulty machine can then described as

$$\begin{bmatrix} U_a \\ U_b \\ U_c \\ U_f(=0) \end{bmatrix} = \begin{bmatrix} R_s & 0 & 0 & -\sigma R_s \\ 0 & R_s & 0 & 0 \\ 0 & 0 & R_s & 0 \\ -\sigma R_s & 0 & 0 & \sigma R_s + R_f \end{bmatrix} \begin{bmatrix} i_a \\ i_b \\ i_c \\ i_f \end{bmatrix} +$$
$$\begin{bmatrix} L & M & M & -(M_{af} + \mathrm{L}_f) \\ M & L & M & -\mathrm{M}_{bf} \\ M & M & L & -M_{cf} \\ -(M_{af} + \mathrm{L}_f) & -M_{bf} & -M_{cf} & L_f \end{bmatrix} \frac{d}{dt} \begin{bmatrix} i_a \\ i_b \\ i_c \\ i_f \end{bmatrix} - \omega_r \Psi_{pm} \begin{bmatrix} \sin(\theta_r) \\ \sin\left(\theta_r - \frac{2\pi}{3}\right) \\ \sin\left(\theta_r + \frac{2\pi}{3}\right) \\ -E_f \sin(\theta_r + \varphi) \end{bmatrix} \quad (5.14)$$

where φ is the phase shift between the induced voltage in the short circuited turns and phase a. The resistances can always be derived using σ, while the inductance parameters (for example L_f and M_{af}) are kept in the generic form in order to not be limited to a specific geometry. However, unless the coils of phase a are heavily electrically scattered, the amplitude scale factor for the back-EMF of the faulty winding, E_f, can be approximated to σ. The negative sign is due to the opposite direction of the fault current i_f compared to i_a.

The faulty machine described using (5.14) can be more densely described as

$$\boldsymbol{V}_{abcf} = \boldsymbol{R}\,\boldsymbol{I}_{abcf} + \boldsymbol{L}\,\frac{d\boldsymbol{I}_{abcf}}{dt} - \boldsymbol{E}_{abcf} \quad (5.15)$$

In order to better understand how the different model inputs contribute to the outputs the faulty machine model can be transformed into a state-space model. By rearranging (5.15) into the form of (3.16) it becomes

$$\frac{d\boldsymbol{I}_{abcf}}{dt} = \boldsymbol{L}^{-1}\left(\boldsymbol{V}_{abcf} - \boldsymbol{R}\,\boldsymbol{I}_{abcf} + \boldsymbol{E}_{abcf}\right). \quad (5.16)$$

It can be seen form (5.16) that the state-space matrixes becomes

$$\boldsymbol{A} = \boldsymbol{L}^{-1}(-\boldsymbol{R}) \quad (5.17)$$
$$\boldsymbol{B} = \boldsymbol{L}^{-1}\boldsymbol{U}_{mat} \quad (5.18)$$
$$\boldsymbol{C} = \boldsymbol{I} \quad (5.19)$$
$$\boldsymbol{D} = 0 \quad (5.20)$$

where $\boldsymbol{U}_{mat}$ is the resulting input matrix correlating the inputs and the back-EMF.

By selecting the applied voltages and the electrical speed of the machine as input, i.e.

$$\boldsymbol{u} = \begin{bmatrix} U_a \\ U_b \\ U_c \\ \omega_r \end{bmatrix} \tag{5.21}$$

then $\boldsymbol{U_{mat}}$ becomes

$$\boldsymbol{U_{mat}} = \begin{bmatrix} \mathbf{1} & \mathbf{0} & \mathbf{0} & \Psi_{pm}\sin(\theta_r) \\ \mathbf{0} & \mathbf{1} & \mathbf{0} & \Psi_{pm}\sin\left(\theta_r - \frac{2\pi}{3}\right) \\ \mathbf{0} & \mathbf{0} & \mathbf{1} & \Psi_{pm}\sin\left(\theta_r + \frac{2\pi}{3}\right) \\ \mathbf{0} & \mathbf{0} & \mathbf{0} & -\Psi_{pm}E_f\sin(\theta_r + \varphi) \end{bmatrix} \tag{5.22}$$

for a PMSM with a turn-to-turn fault.

Evaluating the $\boldsymbol{A}$ and $\boldsymbol{B}$ matrixes results in a large analytical expressions for each element. However, with some algebraic and trigonometric reduction the structure of the matrixes becomes

$$\boldsymbol{A} = \begin{bmatrix} A_{11} & A_{12} & A_{13} & A_{14} \\ A_{21} & A_{22} & A_{23} & A_{24} \\ A_{31} & A_{32} & A_{33} & A_{34} \\ A_{41} & A_{42} & A_{43} & A_{44} \end{bmatrix} \tag{5.23}$$

$$\boldsymbol{B} = \begin{bmatrix} B_{11} & B_{12} & B_{13} & \beta_{14}\cos(\omega_r t + \psi_{14}) \\ B_{21} & B_{22} & B_{23} & \beta_{24}\cos(\omega_r t + \psi_{24}) \\ B_{31} & B_{32} & B_{33} & \beta_{34}\cos(\omega_r t + \psi_{34}) \\ B_{41} & B_{42} & B_{43} & \beta_{44}\cos(\omega_r t + \psi_{44}) \end{bmatrix} \tag{5.24}$$

where the terms A_{ij}, B_{ij}, β_{ij} and ψ_{ij} are all constants consisting solely of different mathematical combinations of the parameters of the faulty machine. The state-space model of the faulty machine shows that the input voltages, being sinusoidal, will produce sinusoidal currents at the same frequency as the input. The machine speed, being a DC quantity, will also contribute with a sinusoidal component at the machine speed as the fourth column of $\boldsymbol{B}$ matrix is a sinusoidal. It can also be seen that frequency of component created from the machine speed will at the synchronous frequency, as the input voltages. Hence, machine currents will only contain a single frequency, where the frequency will be at the electrical speed of the machine.

5.3 Analytical model of a PMSM with a turn-to-turn fault in the synchronously rotating reference frame

The machine with a turn-to-turn fault can be seen as a machine with four windings, where the forth winding is represented by the short-circuited loop in the faulty phase. Therefore, when transforming the model into the synchronously rotating reference frame, the transformation matrix needs to be modified. The new transformation matrixes become

$$T'(\theta_r) = \frac{2}{3}\begin{bmatrix} \cos\theta_r & \cos\left(\theta_r - \frac{2\pi}{3}\right) & \cos\left(\theta_r + \frac{2\pi}{3}\right) & 0 \\ -\sin\theta_r & -\sin\left(\theta_r - \frac{2\pi}{3}\right) & -\sin\left(\theta_r + \frac{2\pi}{3}\right) & 0 \\ 0 & 0 & 0 & \frac{3}{2} \end{bmatrix} \tag{5.25}$$

$$T'^{-1}(\theta_r) = \begin{bmatrix} \cos\theta_r & -\sin\theta_r & 0 \\ \cos\left(\theta_r - \frac{2\pi}{3}\right) & -\sin\left(\theta_r - \frac{2\pi}{3}\right) & 0 \\ \cos\left(\theta_r + \frac{2\pi}{3}\right) & -\sin\left(\theta_r + \frac{2\pi}{3}\right) & 0 \\ 0 & 0 & 1 \end{bmatrix} \tag{5.26}$$

where θ_r is the electrical position of the rotor north pole. Observe that in the transformation the zero sequence component is neglected to avoid singularities in the solution of the state-space model when making the inverse of the machine inductance matrix However, by neglecting the zero sequence the information required for operation is unaffected as long as the machine utilizes a floating neutral point, which is common for inverter connected machines.

It should be stressed that in (5.25) the fault current is not transferred into the rotating reference frame, as it will remain an ac-quantity even in the rotating reference frame. This is because it is a single phase component which on its own cannot be represented with a rotating vector. However, the phase quantities are transformed and their fundamental components will appear as dc-quantities in the rotating reference frame. The currents will of course not be pure dc-quantities as the fault creates an imbalance between the phases. This unbalance will introduce an oscillation in the rotating reference frame, which will be shown by the equations describing the faulty machine in the rotating reference system.

By applying the transformation matrix to the model of the faulty machine described by (5.15) yields

$$T'^{(\theta_r)}\boldsymbol{V}_{abcf} = T'^{(\theta_r)}\boldsymbol{R}\,\boldsymbol{I}_{abcf} + T'^{(\theta_r)}\,\boldsymbol{L}\,\frac{d\boldsymbol{I}_{abcf}}{dt} - T'(\theta_r)\boldsymbol{E}_{abcf} \tag{5.27}$$

By utilizing

$$\boldsymbol{I}_{abcf} = T'^{-1}(\theta_r)\boldsymbol{I}_{dqf} \tag{5.28}$$

then

$$T'^{(\theta_r)}\boldsymbol{V}_{abcf} = \\ T'^{(\theta_r)}\boldsymbol{R}\, T'^{-1}(\theta_r)\boldsymbol{I}_{dqf} + T'(\theta_r)\, \boldsymbol{L}\, \frac{dT'^{-1}(\theta_r)\boldsymbol{I}_{dqf}}{dt} - T'(\theta_r)\boldsymbol{E}_{abcf} \tag{5.29}$$

Evaluation of the derivative term gives

$$T'^{(\theta_r)}\boldsymbol{L}\, \frac{dT'^{-1}(\theta_r)\boldsymbol{I}_{dqf}}{dt} = T'(\theta_r)\, \boldsymbol{L}\frac{dT'^{-1}(\theta_r)}{dt} + T'(\theta_r)\boldsymbol{L}\, T'^{-1}(\theta_r)\frac{d\boldsymbol{I}_{dqf}}{dt} \tag{5.30}$$

Inserting (5.30) into (5.27) gives

$$\boldsymbol{V}_{dqf} = \boldsymbol{R}'\boldsymbol{I}_{dqf} + \boldsymbol{dL}'\, \boldsymbol{I}_{dqf} + \boldsymbol{L}'\frac{\partial \boldsymbol{I}_{dqf}}{\partial t} - \boldsymbol{E}_{dqf} \tag{5.31}$$

where

$$\boldsymbol{V}_{dqf} = T'(\theta_r)\boldsymbol{V}_{abcf} \tag{5.32}$$
$$\boldsymbol{R}' = T'(\theta_r)\, \boldsymbol{R}\, T'^{-1}(\theta_r) \tag{5.33}$$
$$\boldsymbol{dL}' = T'(\theta_r)\, \boldsymbol{L}\frac{\partial T'^{-1}(\theta_r)}{\partial t} \tag{5.34}$$
$$\boldsymbol{L}' = T'(\theta_r)\boldsymbol{L}\, T'^{-1}(\theta_r) \tag{5.35}$$
$$\boldsymbol{E}_{dq0f} = T'(\theta_r)\, \boldsymbol{E}_{abcf} \tag{5.36}$$

Therefore, the equations describing the faulty machine in the DQ-system are

$$\begin{bmatrix} U_d \\ U_q \\ U_f(=0) \end{bmatrix} = \begin{bmatrix} R_s & -(L-M)\omega_r & -\sigma\frac{2R_s\, cos(\theta_r)}{3} \\ (L-M)\omega_r & R_s & \sigma\frac{2R_s sin(\theta_r)}{3} \\ K_1\cos(\theta_r - K_2) & K_1\cos(\theta_r - K_3) & R_f + \sigma R_s \end{bmatrix}\begin{bmatrix} i_d \\ i_q \\ i_f \end{bmatrix} \\ + \begin{bmatrix} L-M & 0 & \frac{3}{2}K_4\cos(\theta_r - K_5) \\ 0 & L-M & \frac{3}{2}K_4\cos(\theta_r - K_6) \\ K_4\cos(\theta_r - K_5) & K_4\cos(\theta_r - K_6) & L_f \end{bmatrix}\frac{d}{dt}\begin{bmatrix} i_d \\ i_q \\ i_f \end{bmatrix} \\ + \omega_r\Psi_{pm}\begin{bmatrix} 0 \\ 1 \\ E_f\sin(\theta_r + \varphi) \end{bmatrix} \tag{5.37}$$

where

$$K_1 = -\frac{1}{2}\sqrt{\left(-2M_{af} + M_{bf} + M_{cf} - 2L_f\right)^2 \omega_r^2 + \left(-2\sigma R_S + \sqrt{3}\left(-M_{bf} + M_{cf}\right)\omega_r\right)^2} \tag{5.38}$$

$$K_2 = tan^{-1}\left(\frac{\left(-2M_{af} + M_{bf} + M_{cf} - 2L_f\right)\omega_r}{2\sigma R_S + \sqrt{3}\left(M_{bf} - M_{cf}\right)\omega_r}\right) \tag{5.39}$$

$$K_3 = tan^{-1}\left(\frac{-2\sigma R_S - \sqrt{3}\left(M_{bf} - M_{cf}\right)\omega_r}{\left(-2M_{af} + M_{bf} + M_{cf} - 2L_f\right)\omega_r}\right) \tag{5.40}$$

$$K_4 = -\frac{1}{2}\sqrt{\left(-2M_{af} + M_{bf} + M_{cf} - 2L_f\right)^2 + 3\left(M_{bf} - M_{cf}\right)^2} \tag{5.41}$$

$$K_5 = tan^{-1}\left(\frac{\sqrt{3}\left(-M_{bf} + M_{cf}\right)}{-2M_{af} + M_{bf} + M_{cf} - 2L_f}\right) \tag{5.42}$$

$$K_6 = tan^{-1}\left(\frac{-2M_{af} + M_{bf} + M_{cf} - 2L_f}{\sqrt{3}\left(M_{bf} - M_{cf}\right)}\right) \tag{5.43}$$

As can be seen in the third column of the current and current derivative matrixes in (5.37), the contribution of the fault current to the d- and q-current is position dependant. While the machine is rotating this contribution will be sinusoidal, and since the fault current is not transformed to the rotating reference frame, it is inherently a sinusoidal quantity with the frequency of the machine's electrical speed. Hence, the evaluated contribution of the fault current on the d- and q-current will constitute of the multiplication of two sinusoidal.

The multiplication of two sinusoidals results in two new frequency components: the sum of the two frequencies and the difference between the two original frequencies, i.e.

$$\sin(x)\cos(y) = \frac{\sin(x+y) + \sin(x-y)}{2} \tag{5.44}$$

In this case, the fault current and rotating reference frame have the same frequency which results in a dc-component and a double frequency component. This means that the d- and q-currents will not be pure dc-quantities, since fault current causes a negative sequence component in both the d- and q-current. As shown in (5.37), the fault current affects the d- and q-current equally with regards to amplitude. However, the fault current contribution is $90°$ electrically shifted between the d- and q-current as K_2 is 90° shifted from K_3, as can be seen in (5.39) and (5.40). This is also true for K_5 and K_6, as can be seen in (5.42) and (5.43).

As for the model in the previous section, the rotating reference model is transformed into the state-space form to better understand how the different model inputs contribute to the outputs. Using the same approach as in the previous section gives

$$\frac{d\boldsymbol{I}_{dqf}}{dt} = \boldsymbol{L}'^{-1}\left(\boldsymbol{V}_{dqf} - \boldsymbol{R}'\boldsymbol{I}_{dqf} - \boldsymbol{dL}'\boldsymbol{I}_{dqf} + \boldsymbol{E}_{dqf}\right) \tag{5.45}$$

$$\boldsymbol{A} = \boldsymbol{L}'^{-1}(-\boldsymbol{R}' - \boldsymbol{dL}') \tag{5.46}$$

$$\boldsymbol{B} = \boldsymbol{L}^{-1}\boldsymbol{U}_{mat} \tag{5.47}$$

$$\boldsymbol{C} = \boldsymbol{I} \tag{5.48}$$

$$\boldsymbol{D} = 0 \tag{5.49}$$

where

$$\boldsymbol{U}_{mat} = \begin{bmatrix} 1 & 0 & 0 \\ 0 & 1 & -\Psi_{pm} \\ 0 & 0 & \Psi_{pm}E_f \sin(\theta_r + \varphi) \end{bmatrix}, \boldsymbol{u} = \begin{bmatrix} U_{\boldsymbol{d}} \\ U_{\boldsymbol{q}} \\ \omega_r \end{bmatrix} \tag{5.50}$$

Evaluating the $\boldsymbol{A}$ and $\boldsymbol{B}$ matrixes results in large and complex analytical equations, which are difficult to interpret. However, with some algebraic and trigonometric reduction the structure of the matrixes become

$$\boldsymbol{A} = \begin{bmatrix} A_{11} + \alpha_{11}\cos(2\omega_r t + \varphi_{11}) & A_{12} + \alpha_{12}\cos(2\omega_r t + \varphi_{12}) & \alpha_{13}\cos(\omega_r t + \varphi_{13}) \\ A_{21} + \alpha_{21}\cos(2\omega_r t + \varphi_{21}) & A_{22} + \alpha_{22}\cos(2\omega_r t + \varphi_{22}) & \alpha_{23}\cos(\omega_r t + \varphi_{23}) \\ \alpha_{31}\cos(\omega_r t + \varphi_{31}) & \alpha_{32}\cos(\omega_r t + \varphi_{32}) & A_{33} \end{bmatrix} \tag{5.51}$$

$$\boldsymbol{B} = \begin{bmatrix} B_{11} + \beta_{11}\cos(2\omega_r t + \psi_{11}) & \beta_{12}\cos(2\omega_r t + \psi_{12}) & B_{13} + \beta_{13}\cos(2\omega_r t + \psi_{13}) \\ \beta_{21}\cos(2\omega_r t + \psi_{21}) & B_{22} + \beta_{22}\cos(2\omega_r t + \psi_{22}) & B_{23} + \beta_{23}\cos(2\omega_r t + \psi_{23}) \\ \beta_{31}\cos(\omega_r t + \psi_{31}) & \beta_{32}\cos(\omega_r t + \psi_{32}) & \beta_{33}\cos(\omega_r t + \psi_{33}) \end{bmatrix} \tag{5.52}$$

where A_{ij}, α_{ij}, B_{ij}, β_{ij}, φ_{ij}, and ψ_{ij} are all constants consisting solely of different mathematical combinations of the parameters of the faulty machine. It is important to stress that the constants (such as $A_{ij}$and B_{ij}) do not have the same value as the for the machine model in the stationary reference frame (the complete expression for $\boldsymbol{A}$ and $\boldsymbol{B}$ is given in Appendix C). These structures show that a PMSM with a turn-to-turn fault behaves typically like an unbalanced machine, i.e. a negative sequence is created in the rotating reference frame, even though the inputs are dc-quantities. Since the fault current is not transformed it will not appear as a dc-signal and the frequency of the current is equal to the electrical speed of the machine. Observe the element on the third row and third column of the $\boldsymbol{B}$ matrix, which shows that a fault current will be induced if the machine rotates. The frequency of the current will be dependent on the electrical speed of the machine.

5.4 Finite element model of the healthy machine

In order to verify the analytical model described in the previous section, a FEM model of the PMSM is developed using Ansoft Maxwell. The selected model is a small machine with the rating of a few kW. This choice is made as it reduces the complexity and requires less computational time to solve. The modeled machine has three phases, five pole-pairs, surface mounted magnets and twelve teeth. Each tooth has a single coil wounded around it which consists of five turns. One phase consists of four series connected coils, leading to a total of twenty turns per phase. The implemented model is presented in Figure 5.2 together with the coil arrangement. The coils are arranged so that the flux travels in a closed loop through only one of the neighboring coils, where the neighboring coil is also part of the same phase, see Figure 5.2. This coil arrangement maximizes the self-inductance, but at the same time it will also minimize the mutual coupling between the phases. The advantage of this arrangement is its ability to minimize the fault current during a complete single-phase short circuit, since the phase impedance is maximized due to the maximized self-inductance. Observe that the physical arrangement does not impact the derived analytical model, as the analytical model is more general and does not have a direct dependency on the structure or winding arrangement of the machine. These aspects only affect the model indirectly, through the inductance dependency on the geometry.

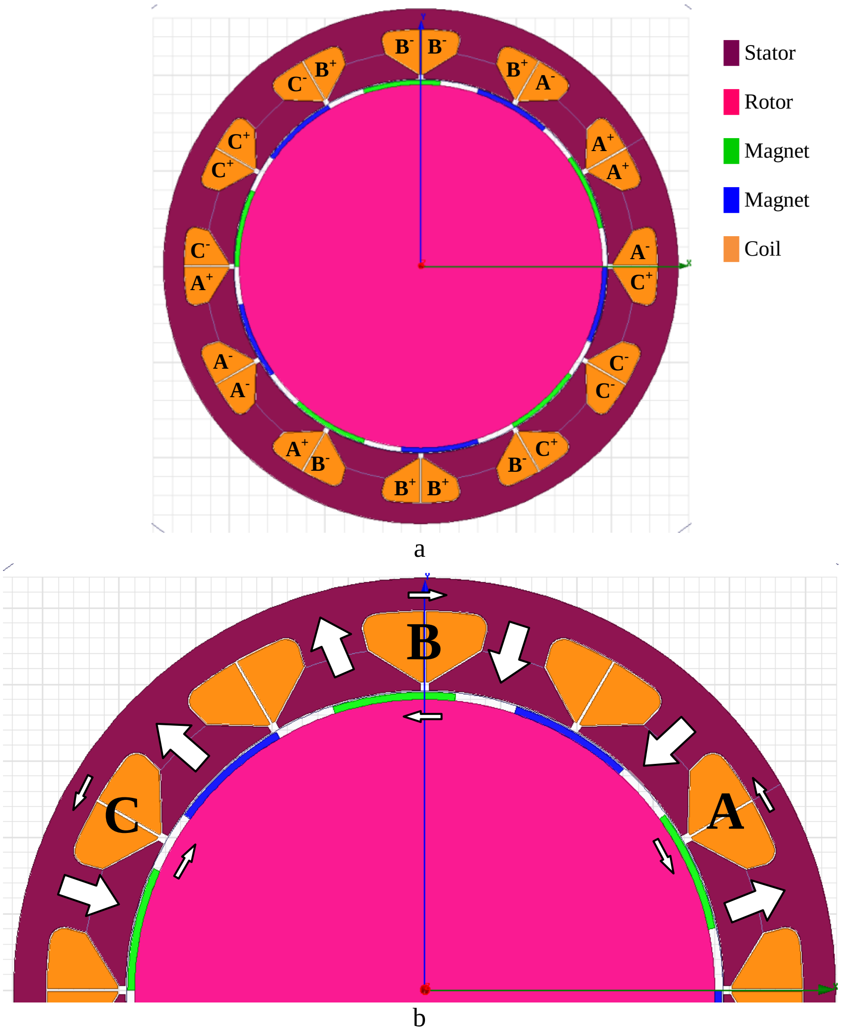

Figure 5.2 FEM model of the machine. Figure a presents the complete machine and the individual winding arrangement of each coil. Figure b presents the flux direction for each phase for positive currents.

The stator and rotor material is chosen to be linear iron, the magnet material is neodymium and the coil material is copper. In Figure 5.2a the coil orientation with superscript + indicates that the winding is exiting the figure towards the reader, whereas – superscript indicates that the winding is entering into the figure. In a magneto-static simulation, the values of the inductances between each coil can be determined. By using the result from the magneto-static simulation the software is able through post-process to calculate the phase and mutual inductance using a method similar to one method described in Section 3.3.1.

Figure 5.3 presents the calculated values of the phase inductances using the simplified rectangular shape for the reluctance described in Section 3.3.1, the more accurate model described in [30], and the results from the FEM simulation. The results are normalized with respect to the self-inductance from the FEM model. As seen from Figure 5.3 the analytical method agrees well for the self inductance, especially when using the more accurate model. For the mutual coupling the different methods have a larger spread in the results. However, it should be stressed once more that this machine has a very low mutual coupling due to its coil arrangement. As such, the difference in absolute values between the methods is small since the actual value is small. It can also be seen that the more accurate reluctance method's results are closer the FEM results compared to the simple model. However, the simple method provides a good first estimation of the inductance value considering the accuracy of the input data required.

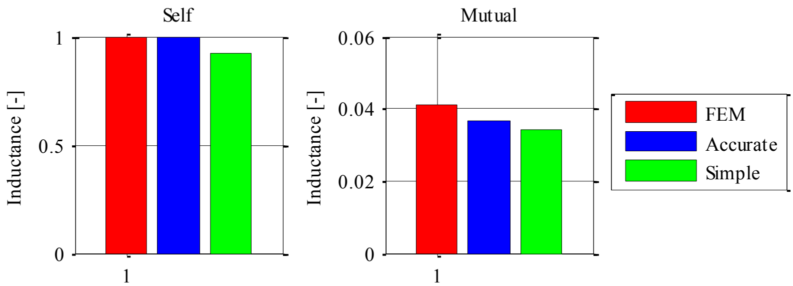

Figure 5.3 Comparison of inductance values for the healthy machine using different method of acquiring the values. The results are normalized with respect to the self-inductance from the FEM model

The FEM model can also be used to investigate the dependency of the inductance on the rotor position. By solving the FEM model for various rotor positions and calculate the inductance for every position, the dependency can be identified. Figure 5.4 presents the normalized inductance value with respect to the electrical position of the rotor. As can be noticed from the figure, the inductances can be considered constant with respect to rotor position, which is a typical assumption for machines with surface mounted magnets.

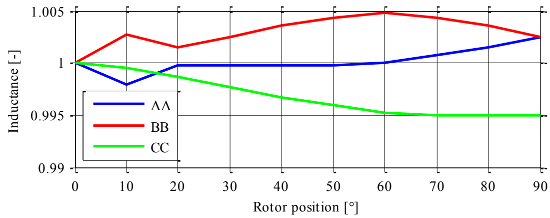

Figure 5.4 FEM calculated self-inductance as a function of electrical rotor position for the different phases.

5.4.1 Back-EMF of the healthy FEM model

In the analytical model, the back-EMF is modeled as the voltage induced by the permanent magnet flux during rotation. In a FEM model this back-EMF can be evaluated through a transient simulation. However, the FEM software calculates induced voltage through integration of flux and unable distinguish the origin of flux. It is therefore important to force all stator currents to zero in order to only have flux originating from the permanent magnets in the machine. In the FEM simulation the machine is set to rotate while all phase currents are forced to be zero in order to simulate an open circuit. Figure 5.5 shows the FEM calculated back-EMF for the three phases normalized with the peak value of phase a. The machine is set to operate at a mechanical rotational speed of 1500 revolutions per minute.

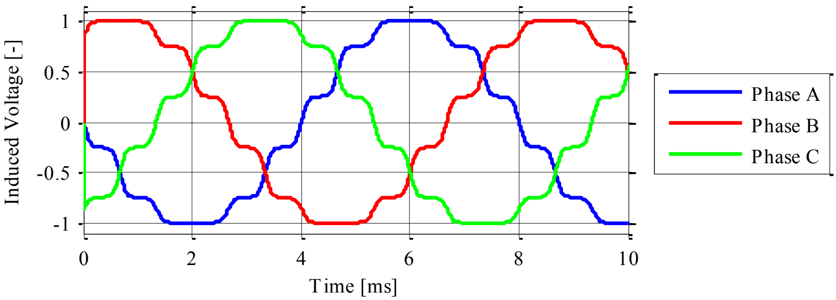

Figure 5.5 FEM calculated back-EMF for the three phases. The machine operates at 1500 rpm while all stator currents are forced to zero.

As can be seen in Figure 5.5, the shape of the back-EMF is not a perfect sine wave and contains low-order harmonics. This is due to the geometry of the modeled machine. By performing a Fourier analysis on the obtained back-EMF, it is possible to observe that, besides the fundamental component, the back-EMF is affected by low-order harmonics. Figure 5.6 presents the harmonic content of the back-EMF, normalized with respect to the fundamental. The fundamental frequency is equal to the machine's electrical speed. By choosing to present the harmonic in multiples of the fundamental rather an in their respective frequencies, the harmonic components will be independent of the machine's operational speed.

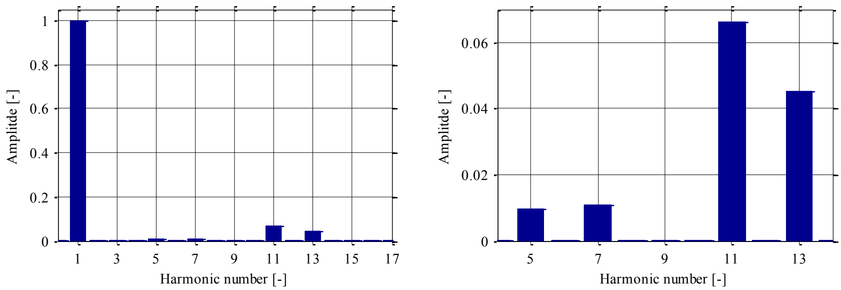

Figure 5.6 Fourier analysis of back-EMF where the amplitude normalized with respect to the fundamental frequency. The left figure presents the first 17 harmonics. The right figure presents a zoomed in version only covering harmonics 5 to 13.

The build-up of the phase back-EMF is the sum of the induced voltage in the four series connected coils. Since the modeled machine has one coil wound around each stator teeth, the phase shift of the fundamental component between each coil can therefore be calculated using the electrical distance between two teeth. Using (3.33), the electrical distance between two teeth for the modeled machine is

$$\varphi = \frac{p\,360°}{\sum t} = \frac{5 \cdot 360°}{12} = 150° \tag{5.53}$$

Figure 5.7 shows the electrical distance off all teeth with respect to tooth A_1, both in total and effective amount of degrees.

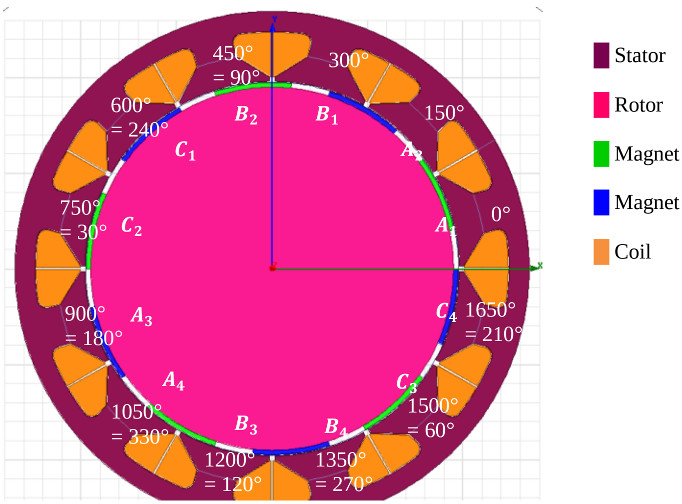

Figure 5.7 The electrical distance off all teeth with respect to tooth A_1, both in total and effective amount of degrees.

However, it is not only the electrical distance which affects the build-up of the back-EMF as the winding direction must also be taken into consideration. As can be seen in Figure 5.2a, coils A_2 and A_3 are wound in opposite direction compared to A_1, as a positive current will create a flux flowing from the stator towards the rotor for a positive current in A_1, where a positive current in A_2 and A_3 will create a flux flowing from the rotor towards the stator. This opposite wounding introduces an additional electrical distance of $180°$. The total back-EMF of phase a is therefore

$$E_a = |A_1|\angle 0° + |A_2|\angle(150 + 180)° + \ |A_3|\angle(180 + 180)° + |A_4|\angle 330° \qquad (5.54)$$

The amplitude of the induced voltage in each coil will be identical as all coils have the same number of turns. If the peak of induced the induced voltage in a single turn is referred to as E_1, then

$$|A_1| = |A_2| = |A_3| = |A_4| = 5E_1 \qquad (5.55)$$

The total back-EMF of a single phase for the modeled machine is then

$$E_a = 2 \cdot 5\ E_1\angle 0° + 2 \cdot 5\ E_1\angle - 30° \approx 19.32E_1\angle - 15° \qquad (5.56)$$

5.4.2 Back-EMF harmonic contribution to the stator current

The modeled back-EMF acts as a speed dependant voltage source. As such, the resulting current is dependent on both the stator circuit as well as the external circuit connected to it. To investigate how the transfer function from the back-EMF to stator currents is affected by the stator circuit, a time varying FEM simulation in performed where the external phase excitations are set to zero voltage. Instead of an external voltage the machine model is loaded with a pure resistive load R which simplifies the simulations. By using a pure resistance as load it will affect the harmonic content in the same way as a converter, as the converter will only effect the fundamental component while acting as a short circuit for the harmonic components.

Figure 5.8 presents a circuit representation of the FEM model simulation setup. As can be seen, the load is connected to the machine terminal in order to close the circuit.

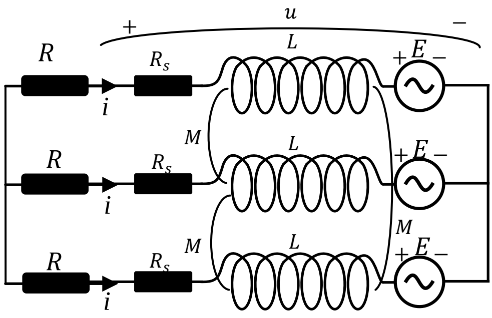

Figure 5.8 Circuit model representation of the FEM model simulation setup.

The machine is excited to a constant mechanical rotational speed of 1500 rev/min. The simulated currents are presented in Figure 5.9 and as it can be seen, the stator currents are less distorted as compared to the back-EMF because of the stator circuit.

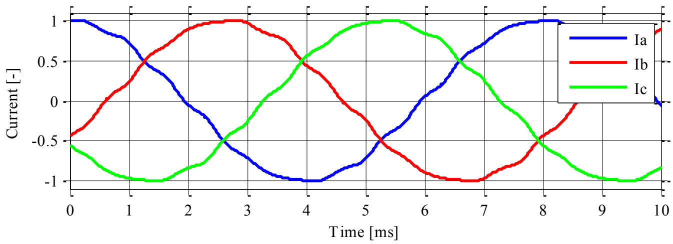

Figure 5.9 Normalized currents from FEM simulation using an external resistance as electrical load.

However, the currents contains the same harmonic content as the back-EMF (see Figure 5.10), where the difference the harmonics amplitude is due to the filtering effect of the stator circuit.

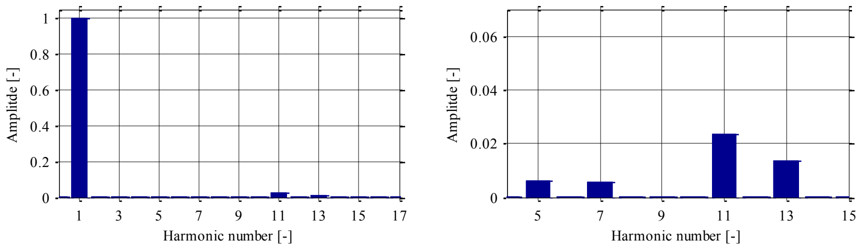

Figure 5.10 Fourier analysis of phase currents loaded with a resistive load, the amplitude normalized with respect to the fundamental frequency.

5.5 Finite element model faulty machine

The faulty FEM machine is based on the healthy machine model; here an additional coil has been included to emulate the turn-to-turn fault. The new coil shares space with one of the existing coils as illustrated in Figure 5.11.

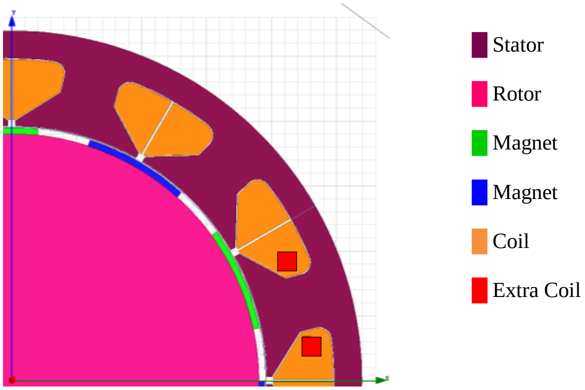

Figure 5.11 FEM model of a PMSM with an additional coil to represent the turn-to-turn fault.

The added coil is used to model the turn-to-turn fault and will further be referred to as faulty coil, and a non-faulted coil will be referred to as healthy coil.

The maximum number of turns in the faulty coil is equal to the number of turns in a healthy coil, as the faulty coil is simply a representation of short-circuited turns. For the machine modeled in this section the maximum number of turns in the faulty coil is five. If an entire coil is short circuited then the affected phase will consist of three healthy coils and the faulty coil consisting of five turns. However, if only one turn is short circuited, then the affected phase will consist of three healthy coils, four healthy turns and the faulty coil consisting of one single turn. Since a turn-to-turn fault does not alter the geometry or remove any turns, the number of turns in a phase will be equal for both the healthy machine and the faulty machine. The difference between the two modes depends on how the turns are connected internally.

The orientation of the faulty coil is in the same direction as the healthy coil in order to keep the current orientation. It should be stressed that the current in the faulty coil is not the current referred to as i_f in Section 5.2 and 5.3, but rather the current i_2 in Figure 5.1b. This current can be calculated as $i_a - i_f$ from the analytical equations of Section 5.2. The FEM simulated back-EMF of the faulty machine is presented in Figure 5.12, where the phase current are forced to zero in order to simulate an open circuit, as for the healthy case. The faulty coil in this example consists of one turn.

The term σ is in this case

$$\sigma = \frac{N_2}{N_a} = \frac{1}{20} = 0.05 = 5\% \tag{5.57}$$

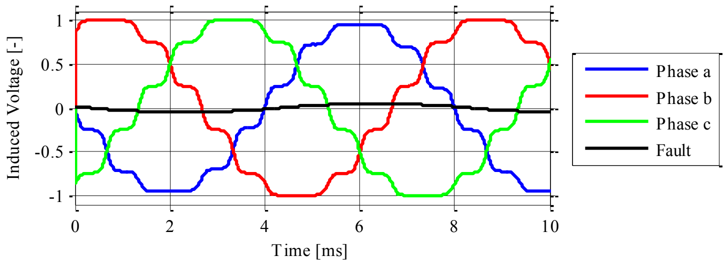

a

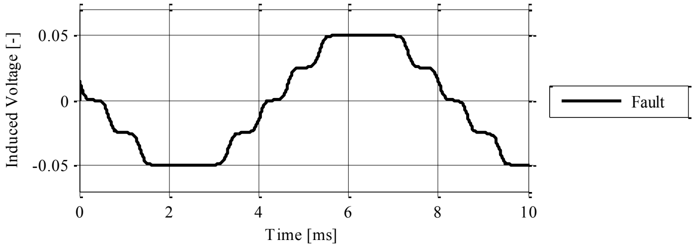

b

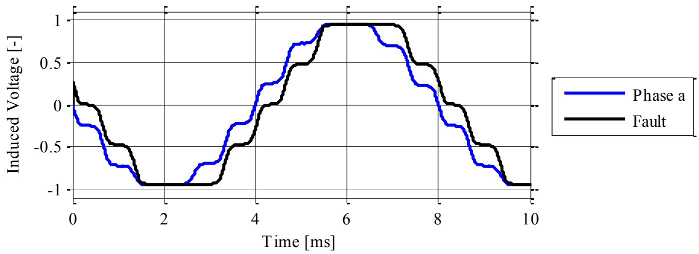

c

Figure 5.12 FEM calculated back-EMF. Figure a presents the induced voltage in the three phases and the faulty coil normalized with respect the peak value of a healthy phase. Figure b presents identical information on the faulty coil as in figure a but whit a larger scale. Figure c presents the faulty coil and phase a where the faulty coil values have be scaled to match the phase a value.

Due to the fault condition, the induced voltage in phase a is slightly reduced as compared with the healthy case (since it only consists of 19 turns during the fault), while the non-faulted phases voltages are unchanged. The induced voltage in the faulty coil is phase shifted with respect to phase a, as can be seen in Figure 5.12c.

This is due to the electrical distance between teeth. Analytically, the back-EMF of the faulty phase a is (where the tooth with the turn-to-turn faults occurs in the reference),

$$E = 4E_1\angle 0° + 5E_1\angle(150+180)° + 5E_1\angle(180+180)° + 5E_1\angle 330° \approx 18.35E_1\angle -15.8° \tag{5.58}$$

Which is $-0.8°$ phase shifted compared to the healthy machine, see (5.56), and the amplitude of the fundamental component is for the faulty machine compared to the healthy machine is

$$\frac{18.35E_1}{19.32E_1} = 0.9498 \approx 0.95 = 1 - \sigma \tag{5.59}$$

This small amplitude difference, together with the small phase shift makes the back-EMF of the faulty machine unbalanced.

Since the faulty coil in this case only consists of a single turn (located at the reference tooth) the back-EMF in the faulty coil is

$$E_f = E_1\angle 0° \tag{5.60}$$

which is the part removed from the healthy machine described by (5.54) compared with the faulty machine described by (5.58).

The inductance values of the faulty machine are calculated using the same method as for the healthy case. The FEM model is solved in an electro-static simulation where the faulty coil is current excited. A reluctance grid can also be used to calculate the faulty inductances by using the equations described in Section 3.3.1. Figure 5.13 presents the two analytical methods using the reluctance grid and the FEM results, normalized with respect to the FEM result of the mutual coupling between the faulty coil and the a phase.

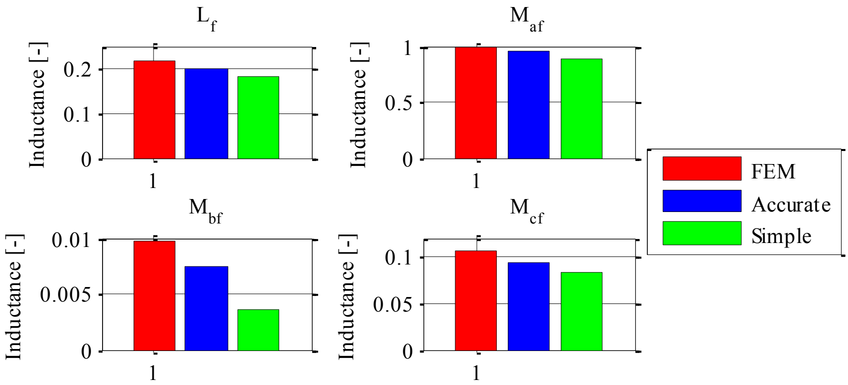

Figure 5.13 Comparison of the different methods for calculating the self-inductance of the faulty coil and the mutual coupling between the faulty coil and the other phases. Note the different scales in the figures.

The analytical methods show less agreement with the FEM results compared with the healthy machine case (see Figure 5.3). The comparative values for M_{bf} is greatly different and for M_{cf} the results also shows low agreement. However, due to the machine layout which is causing a very low mutual coupling between the phases even during healthy conditions, the coupling between the faulty coil and the other phases will be even smaller. I.e. the absolute difference between the methods is small. The difference in mutual coupling between the fault coil and phase b and phase c respectively, is due to the machine geometry. In this case, the fault has occurred in coil A_1 (see Figure 5.7) where the neighboring coils are A_2 and C_4. Hence the flux produced by the faulty coil that reaches a coil belonging to phase b is less than what reaches phase c due to the longer distance between the faulted coil and a coil belonging to phase b.

The FEM model is limited in its connections possibilities, as the simulation software only allows series connection of the different coils. In order to more accurately model the parallel connection of the coils which occurs during a turn-to-turn fault, as wells as incorporating the contact resistance R_f, the FEM software is coupled to the circuit simulator Ansoft Simplorer. The coupling enables more connection possibilities between the coils and the resulting simulation setup is shown in Figure 5.14.

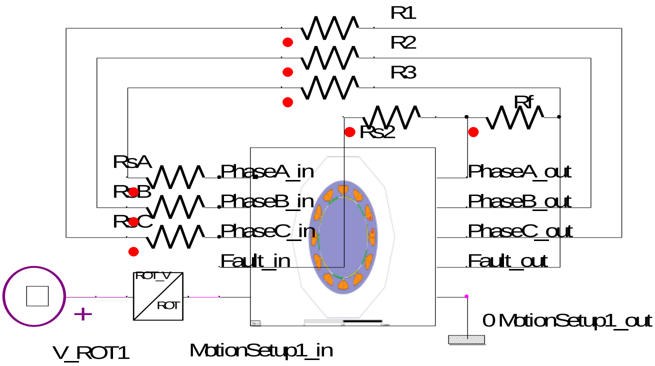

Figure 5.14 Coupling between Ansoft Simplorer and Ansoft Maxwell in order to create the correct connections between the coils.

As in the healthy machine FEM simulation, the faulty machine is connected to a pure resistive load and externally excited to rotate at a constant speed. The simulated currents for the faulty machine are shown in Figure 5.15, normalized with respect to the peak value of current I_b.

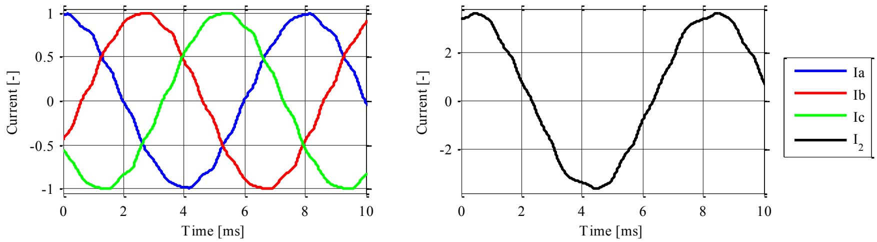

Figure 5.15 Coupled simulation between Ansoft Simplorer and Ansoft Maxwell in order to create more accurate connections of the coils.

For this operation point, the peak current in the faulty coil is about four times the peak current in the other phases, which in this case result in more than six times higher losses in the form of heat. The extra heat will lead to further winding failure and other types of faults, as described in Section 4.4. However, even though this comparatively large current has a large local impact on the machine, the impact on the phase current is very small, as seen in Figure 5.15.

5.6 Comparison between analytical and FEM Models

A healthy three phase machine is analytically modeled according to (3.14) where the parameter values extracted from the healthy FEM are used in order to make the analytical and FEM model as similar as possible for the comparison. The analytical model is simulated using an identical setup as the FEM machine, i.e. an external source governs the rotor rotation and the machine is loaded with a pure resistive load. The simulation results of both the analytical and the FEM models are presented in Figure 5.16. The difference between the stator currents obtained using the two models is presented in Figure 5.16b. As can be more easily seen from the difference figure, the FEM model contains harmonics and not purely the fundamental, which are only accounted for in the analytical model.

The back-EMF of the analytical model is purely sinusoidal with the frequency of the machine's electrical speed (see (3.14)). As such, in order for the analytical model to better agree with the FEM model, the analytical model need to be updated with respect to the harmonics present in the FEM back-EMF.

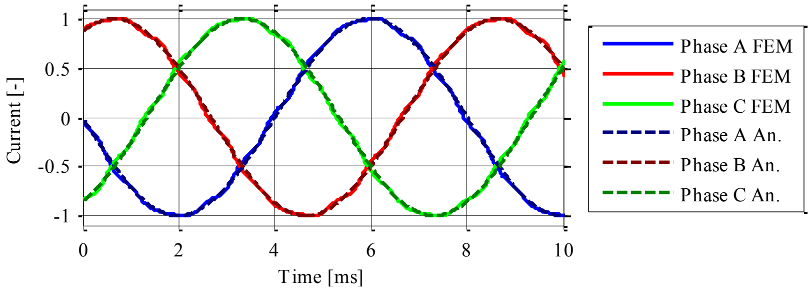

a

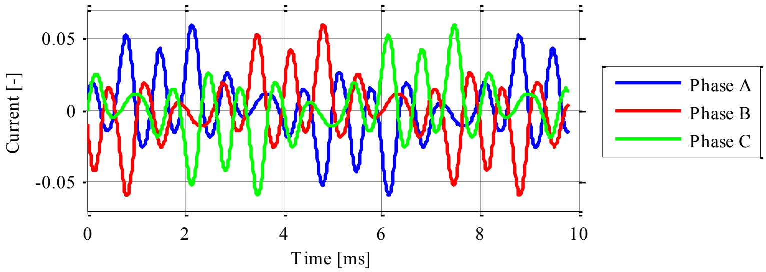

b

Figure 5.16 Comparison of simulation results from the FEM and the analytical model. Figure a presents both simulation results and figure b presents the difference between the two models. Both are normalized with respect the fundamental component.

By performing a Fourier analysis on the FEM back-EMF the harmonics amplitude and phase can be found. The back-EMF vector of the updated analytical model is thus given by

$$\mathbf{E}_{abc} = -\omega_r \Psi_{pm} \begin{bmatrix} \sum_{i=1}^{\infty} \sin\left(A_{H,i}\theta_r + \varphi_{a,i}\right) \\ \sum_{i=1}^{\infty} \sin\left(A_{H,i}\theta_r + \varphi_{b,i} - i\frac{2\pi}{3}\right) \\ \sum_{i=1}^{\infty} \sin\left(A_{H,i}\theta_r + \varphi_{c,i} + i\frac{2\pi}{3}\right) \end{bmatrix} \tag{5.61}$$

where $A_{H,i}$ is the relative amplitude of the i^{th} harmonic and φ_i is the phase shift of i^{th} harmonic. The simulation results of from the updated healthy machine model together with the FEM results are shown in Figure 5.17. There is still a small difference between the models as not all of FEM harmonics are added to the updated analytical model. For the considered operating condition, only harmonics having an amplitude greater than 0.1V have been included in the analytical model. The highest-order harmonic considered in the analytical model is the 25th harmonic as the amplitude of the above harmonics are small and can be difficult to acquire due to the requirement of fast sampling frequency which may not be available in wind turbine applications.

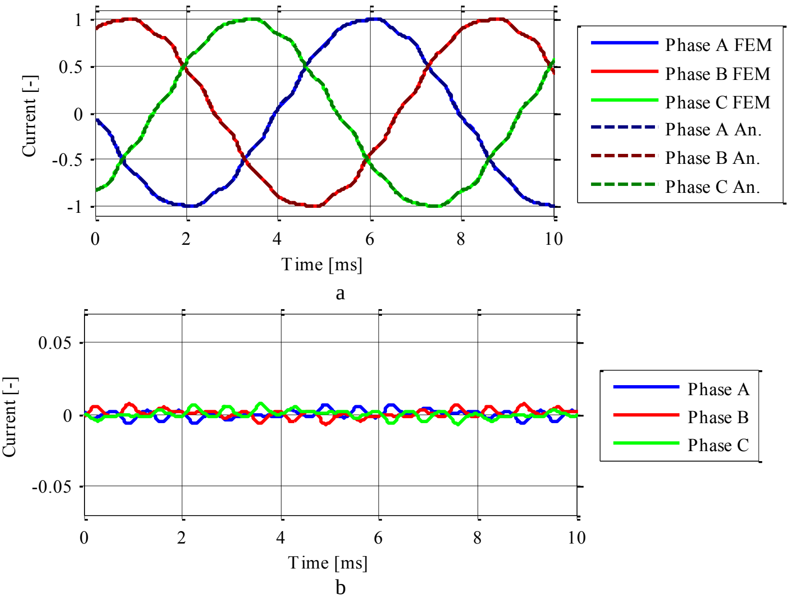

Figure 5.17 Comparison of simulation results from the FEM and the analytical model with added back-EMF components. Figure a presents both simulation results and figure b presents the difference between the two models. Both are normalized with respect the fundamental component.

Using the updated back-EMF vector, the analytical model achieves a satisfactory agreement with the FEM model. The back-EMF is modeled to linearly follow the electrical speed of the machine. To verify the validity of this for both the fundamental and the harmonics, the FEM model was simulated in open-circuit mode at different speeds (two times, half, quarter and at one eight of the nominal speed). The results are presented in Figure 5.18, normalized with respect to the fundamental component at nominal speed. As can be seen, the back-EMF is linear with the speed for the FEM model for both the fundamental and the harmonics.

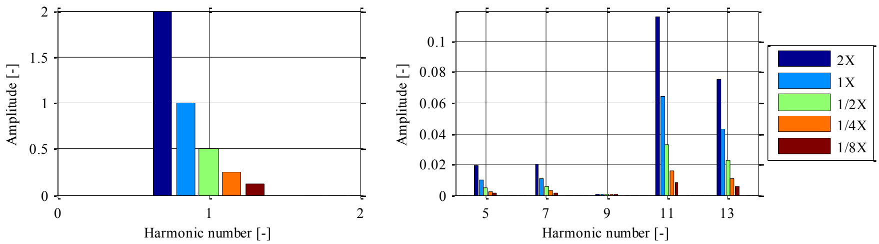

Figure 5.18 Amplitude of FEM back-EMF at various speeds, normalized with respect to the fundamental component at nominal speed.

To verify that the analytical model and the FEM model does not only agree during steady-state operation, more dynamic simulations were performed where the machine speed was varied. Figure 5.19a presents the simulated current response from one phase when the speed was ramped up from nominal speed to two times nominal speed during nominal loading. The machine starts to accelerate at 5 ms, and 10 ms later the machine speed is two times the original value prior to the acceleration (this speed increase during this short time is not a realistic scenario, merely an illustrative example). Figure 5.19b presents the simulated current response from one phase when the speed is stepwise doubled from nominal speed. Both figures are normalized with respect to nominal speed. As it can be seen from the presented results, very good agreement between the FEM and the analytical model is obtained also during dynamic conditions of the machine.

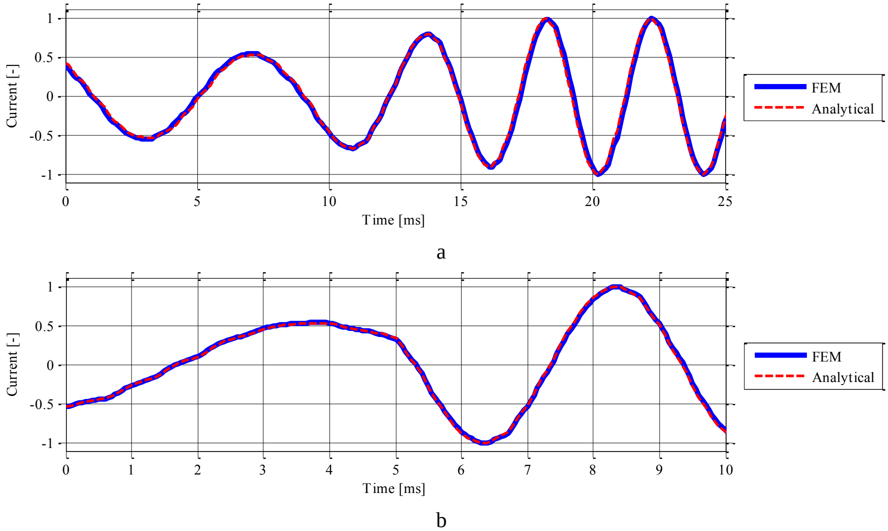

Figure 5.19 Simulation results for one phase from both the analytical model and the FEM model during simulations where the speed is varied. Figure a shows the results during a ramp increase of the speed, where figure b presents a step increase of the speed.

In order to verify that the analytical model and the FEM model also agree for various external loadings, the external resistance connected at the machine terminals (see Figure 5.8) can be varied. Figure 5.20 presents the obtained simulation results (the machine is rotating at nominal speed) when the external resistance changed to two times, five times and ten times the resistance value used for the other simulations, respectively. The results are normalized with respect the nominal resistance. As can be seen, the two models presents simulation results which are satisfactory similar.

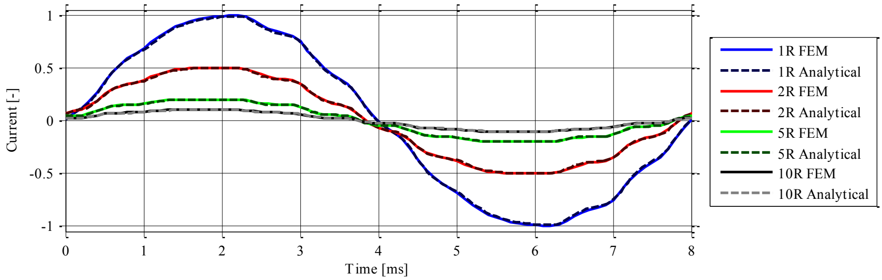

Figure 5.20 Simulation results from both the analytical model and the FEM model for various external loadings.

The same verification procedure is applied for the faulty machine case. The values of the inductances are calculated using the FEM model and the results are used in the analytical model. Figure 5.21a shows the obtained simulation results of the updated analytical faulty machine model together with the results from the faulty FEM model; the machine has one out of twenty turns short circuited and is operating at nominal speed loaded with a the pure restive load as in previous simulations. Figure 5.21b shows the obtained difference between the two model. All results are normalized to with respect to unfaulted machine case operating under equal operation conditions.

As seen in Figure 5.21, the faulty analytical model and the faulty FEM model show a satisfactory agreement with about the same error as for the healthy model. The error is due to not including all harmonics in the analytical model. Since the updated analytical model of the faulty machine provides comparable results as the FEM model at a greatly reduced simulation time, it is therefore more practical to use the analytical model for further analysis of the impact of the fault. The impact can be studied on a system level to see any secondary effects, but the model can also be used to investigate the possibilities to detect a turn-to-turn fault.

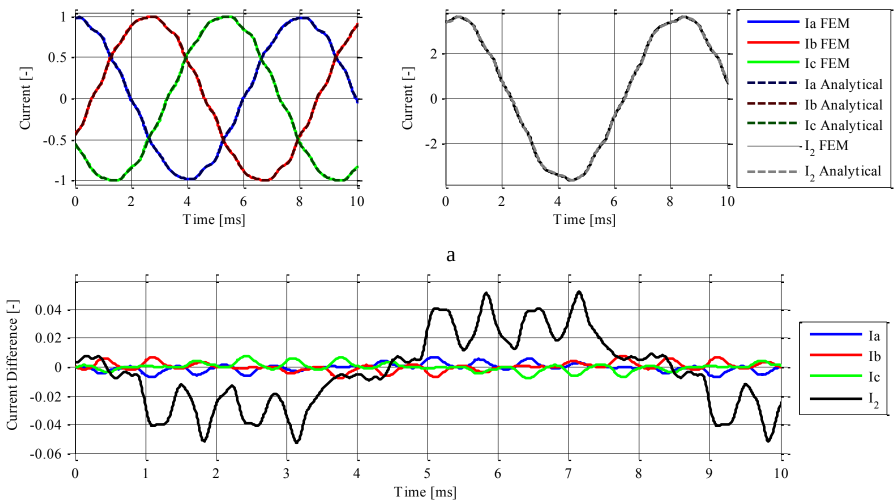

b

Figure 5.21 Comparison of simulation results from the FEM and the analytical model with added back-EMF components. Figure a presents both simulation results and figure b presents the difference between the two models. Both are normalized with respect the fundamental component.

5.7 Flexible analytical model

Assume that the original state of a machine is healthy and, after a given time, the insulation of the stator winding fails (see Section 4.4), causing a turn-to-turn fault that turns the healthy machine in to a faulty machine. It would therefore be convenient to develop a model that is able to simulate the transient behavior from healthy to faulty. This feature would allow the study of how the machine behaves directly before and directly after the fault has occurred. To achieve this, consider that the analytical model of the faulty machine contains all the information of the healthy machine; thus, with some manipulation the faulty machine model is able to simulate the behavior of the healthy machine. The difference between the healthy and the faulty model is current i_f and its interaction with the other currents. By keeping i_f equal to zero, the faulty machine model is effectively the same as the healthy machine model. One method to set i_f to zero would be to chose the value of the emulated contact resistance R_f in Figure 5.1 to infinity, thus treating the fault loop as an open circuit. If the parameter R_f goes towards zero it represents a perfect short circuit between two conductor. However, simply selecting the value of R_f to be infinity large is not a practical solution to implement for the analytical model. When solving the state-space equations, a large value of R_f will make the derivatives terms very large. This requires an impractically small time step in order for the simulation model to converge. An alternative way to simulate the transition between the healthy and the faulty machine model is to modify the fault loop by adding a controllable voltage source, U_f, in series with R_f, see Figure 5.22.

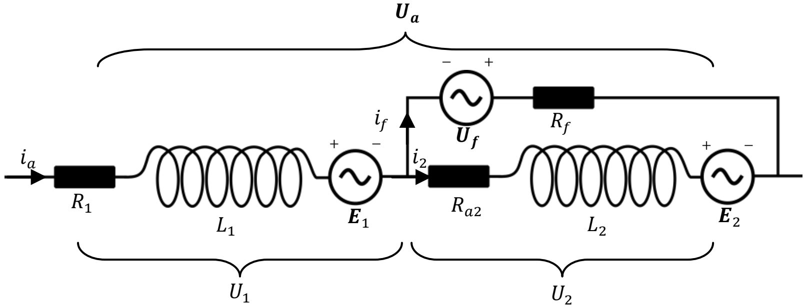

b

Figure 5.22 The single phase representation of healthy phase illustrated in figure a, and the single phase representation during a turn-to-turn fault illustrated in figure b.

During a fault, U_f is forced to zero volts, but during healthy operation U_f is used to instantaneously counteract any current changes in i_f. If the initial condition of i_f is zero, it will remain at this value by selecting the amplitude of U_f to always keep the derivative of i_f to zero. By using the equation of the current derivatives (5.16), the value of U_f can then be determined for every time instant. Figure 5.23 shows the simulation results for a healthy machine model together with the flexible model with the voltage source U_f controlled to counteract the fault current. The two models can be considered to be identical as difference in results is practically non-existing, see Figure 5.23b. After 10 ms of simulation U_f is forced to zero to make the model shift from healthy mode to faulty mode. Figure 5.23c shows the fault current during the first 20 ms of simulation. As can be seen, there is no fault current until the model is switched at 10 ms.

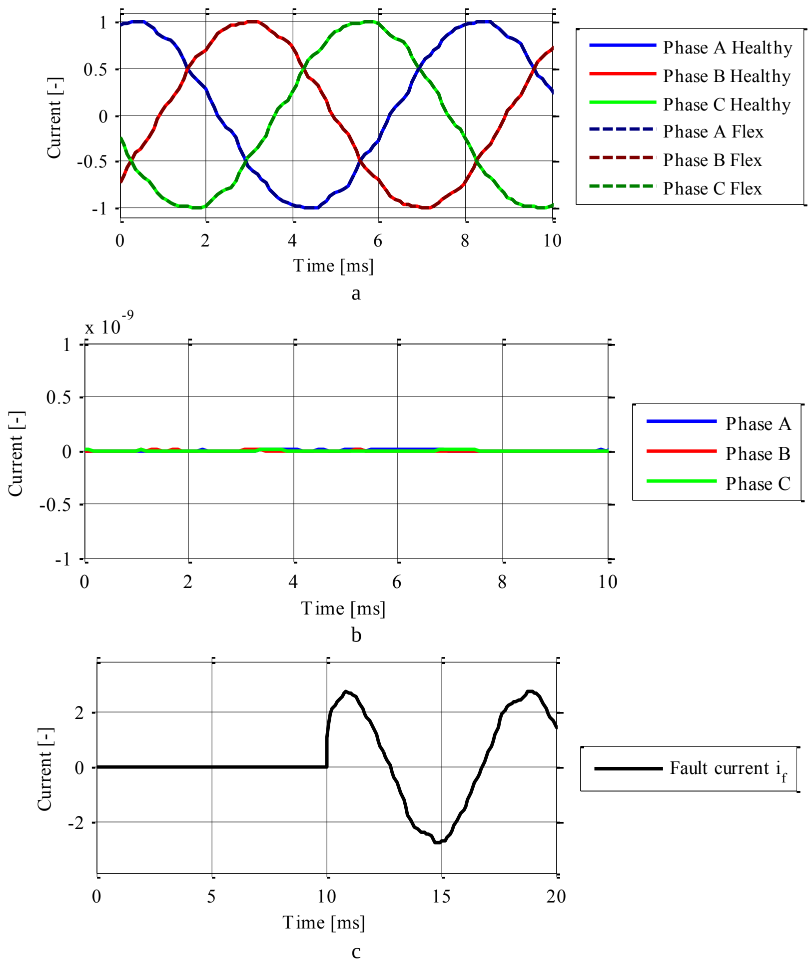

Figure 5.23 Comparison of simulation results from the healthy and flexible model. Figure a presents both simulation results and figure b presents the difference between the two models. Figure c presents the simulated fault current i_f. All are normalized with respect the peak current of the healthy machine.

Using the described flexible model allows the investigation of not only the transition but also the impact of the evolution of connection resistance R_f. By keeping all other simulation parameters constant while varying the fault resistance, the effect of the fault resistance value on the fault current can be studied. Figure 5.24 shows the peak fault current in the faulty coil as a function of the fault resistance.

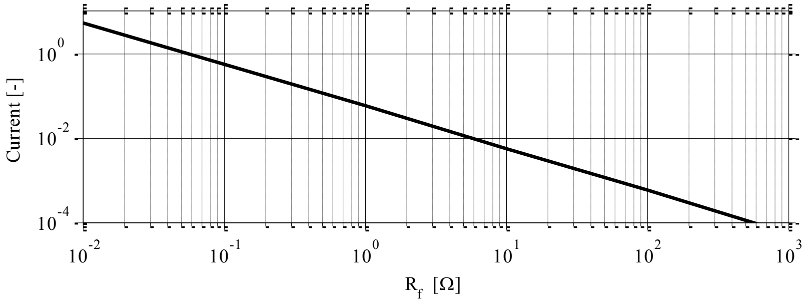

Figure 5.24 Fault resistance effect on fault current i_f normalized with respect to peak healthy phase current with equal loading.

The fault current decreases with an increasing resistance, which is to be expected. This figure also demonstrates how the fault current can increase with time, as the turn-to-turn fault can initially have poor connection with high resistance but as time passes with the extra heat production due the fault, it is likely that the insulation will deteriorate further leading to a better connection between the windings. This will in turn reduce the resistance further causing larger current, more heat and more insulation failure.

Using the flexible model, it is possible to investigate if the steady-state condition of the faulty current depends on point-on-wave when the fault initially occurred. Figure 5.25 presents the simulation results where the fault mode was initiated at different time instances. All the models where simulated using identical settings, except for the triggering of the shift to faulty mode. As can be seen, the fault currents steady-state condition is independent on the time of failure, which was to be expected. As the derived model does not consider any parasitic capacitive couplings between the turns, there is no oscillation during transient transition from healthy to fault. The modeled system only consists of resistance and inductance, which results in the smooth current shown in the figure during the transition, regardless of the point-on-wave of the fault occurrence.

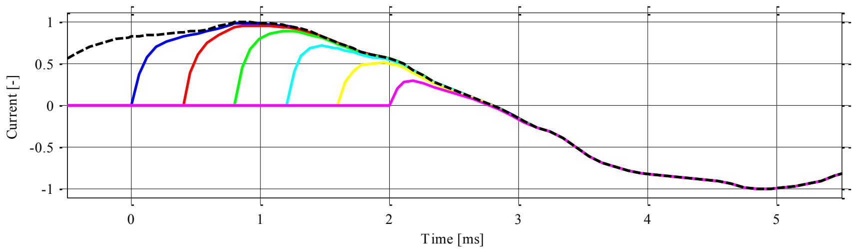

Figure 5.25 The simulation results from the flexible model when the fault occurs at different times.

5.8 Comparison between healthy and faulty machine and the indication of an turn-to-turn fault

The comparison is performed when the models operate in steady-state where the rotor speed is externally excited and the machine is loaded with a pure resistive load, as previously done when comparing the analytical model with the FEM models. Figure 5.26 shows both the current from the healthy model and the faulty model.

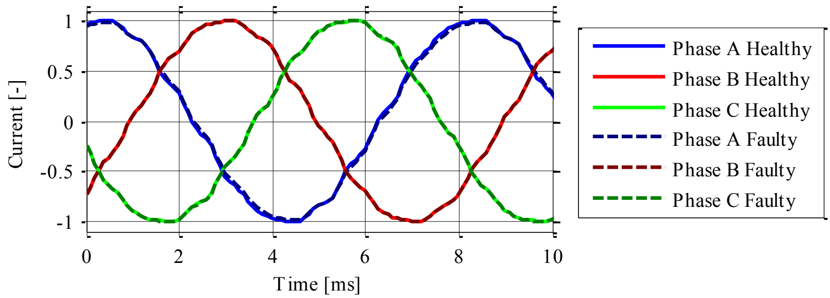

a

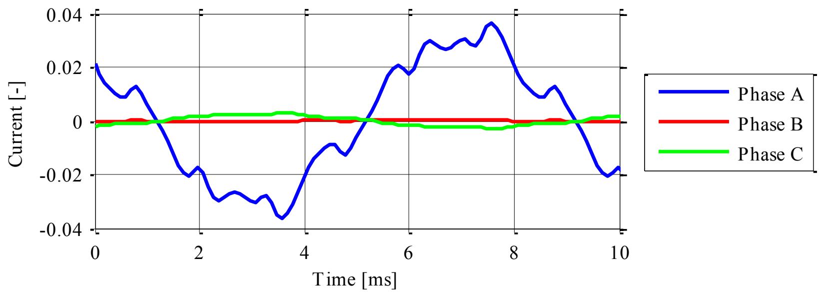

b

Figure 5.26 Normalized phase currents from the healthy and faulty machine models. Figure a presents the three phase currents of both models, figure b present the difference between the two models.

As can be seen in Figure 5.26a, the current from the two models are very similar which pose a problem for detecting the turn-to-turn fault. There is a difference between the two models, especially for the affected phase a which shows the greatest difference. However since both results are not available during operation the method of comparison cannot be utilized as an online indication method. Dependant on the operation point the absolute difference in the current between the healthy and faulty machine may be very small and thus difficult to detect. There is another general drawback with the comparison method, being that it can only indicate that there is difference between the two states. It does not provide any information of the cause of this difference, which could be caused by any part of the machine.

In the case of a turn-to-turn fault, it is both the machine parameters as well as the back-EMF that are affected by the fault. Both the parameters and the back-EMF become unbalanced due to the fault, where the severity of the unbalance depends on the amount of short-circuited turns. The unbalanced back-EMF may have an altered harmonic content compared to the balanced case, and the unbalanced machine parameters will to some extent distort the current as compared to the healthy case. The current frequency content may therefore be a more effective quantity to monitor to be able to detect a turn-to-turn fault. Figure 5.27 presents the frequency spectra of the current from phase a from both the healthy and faulty models. The results are normalized with respect to the fundamental component of the healthy model. As can be seen there are only minor amplitude differences between the two.

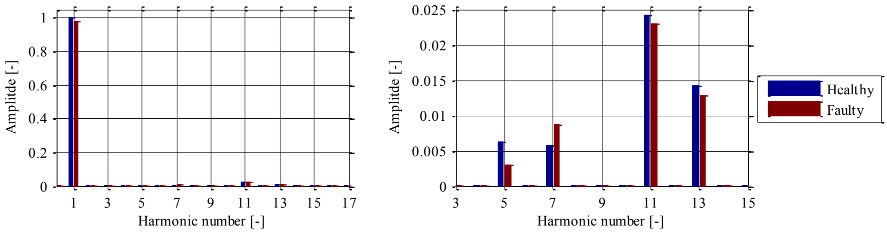

Figure 5.27 Normalized harmonics in the current of phase a from both the healthy and faulty machine models

An alternative can be to monitor the frequency content of the stator current in the rotating reference frame. The frequency content of the stator dq-current from both the healthy and the faulty model is presented in Figure 5.28. Figure 5.28a is normalized with respect to the healthy fundamental components respectively where Figure 5.28b is not normalized, to show that the d- and q-components are affected equally by the fault.

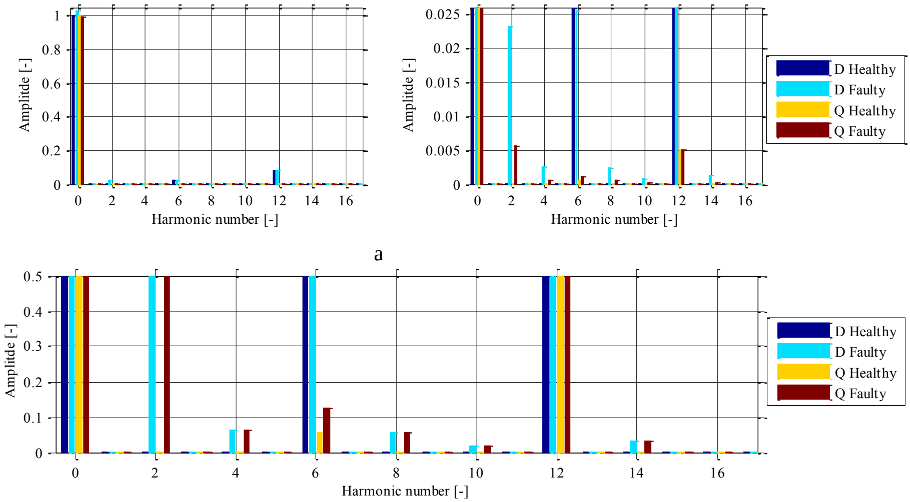

c

Figure 5.28 Harmonics in content in the currents in the rotating reference frame from both the healthy and faulty machine models. Figure a presents the normalized currents, figure b presents the non-normalized information which shows that d- and q-components are affected equally.

The appearance of the second harmonic is the most noticeably change due to its comparatively large amplitude. As shown by (5.37), the appearance of the second harmonic (i.e. the negative sequence) is a typical indication of a system unbalance in the rotating reference frame. The turn-to-turn fault does make the machine turn from a balanced to an unbalanced system. However, making the system unbalanced is not a unique characteristic of a turn-to-turn fault. By looking at Figure 5.28, it is not only the second harmonic that has appeared due to the fault. For instance the fourth and eight harmonics have also appeared. These are created due to the unbalanced back-EMF and the unbalanced machine parameters, together with the transformation to the rotating reference frame. For example, the fourth harmonic originates from the fifth harmonic in the stationary reference frame. The transformation of the d-component for the fifth harmonic is

$$\frac{2}{3}\left[\cos\theta \quad \cos\left(\theta-\frac{2\pi}{3}\right) \quad \cos\left(\theta+\frac{2\pi}{3}\right)\right]\begin{bmatrix} A^*_{H,5}\cos(5\theta+\alpha) \\ A_{H,5}\cos\left(5(\theta-\frac{2\pi}{3})\right) \\ A_{H,5}\cos\left(5(\theta+\frac{2\pi}{3})\right)\end{bmatrix}$$

$$\begin{aligned}
&= \frac{1}{3}[\, A^*_{H,5}\cos(5\theta+\alpha-\theta)+A_{H,5}\cos\left(5\theta+\frac{2\pi}{3}-\left(\theta-\frac{2\pi}{3}\right)\right) \\
&\quad + A_{H,5}\cos\left(5\theta-\frac{2\pi}{3}-\left(\theta+\frac{2\pi}{3}\right)\right)+ A_{H,5}\cos(5\theta+\alpha+\theta) \\
&\quad + A_{H,5}\cos\left(5\theta+\frac{2\pi}{3}+\left(\theta-\frac{2\pi}{3}\right)\right)+A_{H,5}\cos\left(5\theta-\frac{2\pi}{3}+\left(\theta+\frac{2\pi}{3}\right)\right) \\
&= \frac{1}{3}[\, A^*_{H,5}\cos(4\theta+\alpha)+A_{H,5}\cos\left(4\theta-\frac{2\pi}{3}\right)+A_{H,5}\cos\left(4\theta+\frac{2\pi}{3}\right) \\
&\quad + A^*_{H,5}\cos(6\theta+\alpha)+A_{H,5}\cos(6\theta)+A_{H,5}\cos(6\theta)
\end{aligned} \tag{5.62}$$

The same procedure can be performed for the q-component. In the normal balanced case, the 5th harmonic is typically symmetrical, meaning that $A^*_{H,5} = A_{H,5}$ and α is zero. Therefore, under these conditions the harmonic term that oscillates with a frequency of four times the machine speed is equal to zero. However, during a turn-to-turn fault α becomes non-zero and $A^*_{H,5}$ is reduced as compared with the pre-fault condition ($A^*_{H,5}$ is approximately equal to $\sigma A_{H,5}$ during the fault condition) which makes

$$A^*_{H,5}\cos(4\theta+\alpha)+A_{H,5}\cos\left(4\theta-\frac{2\pi}{3}\right)+A_{H,5}\cos\left(4\theta+\frac{2\pi}{3}\right) \neq 0 \tag{5.63}$$

thus, the fourth harmonic appears for this case.

In general, this new set of harmonics can be explained using a vector representation (see Appendix A) of a three phase system. A generic unbalanced and distorted three phase voltage vector $\boldsymbol{e_k}(t)$ in the stationary reference frame can be described as[51]

$$\boldsymbol{e_k}(t) = \boldsymbol{e_{k_p}}(t)+\boldsymbol{e_{k_n}}(t) = E_{k_p}\mathrm{e}^{\mathrm{jk(\omega t+\varphi_p)}}+E_{k_n}\mathrm{e}^{-\mathrm{jk(\omega t+\varphi_p)}} \tag{5.64}$$

where ω is the angular frequency of the system. E_{k_p} and $E_{k_n}$are the amplitudes of positive and negative phase sequence voltage vectors, respectively, φ_p and φ_n are their phase displacements, and k indicates the harmonic number. Observe that in (5.64) the zero sequence component has not been considered. During balanced operation, the negative sequence component for the harmonics 1, 4, 7 and so on, is zero. For harmonics 2, 5, 8 and so on, the positive sequence is zero during normal operation. By moving (5.64) into the rotating reference frame it can be seen that the harmonic shift in frequency as

$$\mathrm{e}^{-j\omega}\boldsymbol{e_k}(t) = E_{k_p}\mathrm{e}^{\mathrm{j(k-1)(\omega t+\varphi_p)}} + E_{k_n}\mathrm{e}^{-\mathrm{j(k+1)(\omega t+\varphi_p)}} \tag{5.65}$$

The positive components will be represented at one harmonic number below while the negative sequence will be represented at one harmonic number above. Thus, both the fifth and seventh harmonic in the stationary reference will be represented as the sixth harmonic in the rotating reference frame during balanced operation. However, as described earlier, during an unbalanced condition the fifth harmonic in the stationary reference frame contains both a negative and positive sequence component, which will then appear as the fourth and sixth harmonic in the rotating frame. As such, during unbalanced conditions, the harmonics in the rotating reference will split-up

In essence, by monitoring the harmonic content of the current in the rotating reference frame it is possible to detect a turn-to-turn fault through observation of the second harmonic in combination with the appearance of new specific harmonics. What appears to be typical for the turn-to-turn fault is the addition of the new harmonics that is originating from the unbalanced back-EMF, which is feed through an unbalanced impedance circuit. Note that the amplitude of the new harmonics have equal amplitude in both the d- and the q-currents, which is to be expected by inspection of (5.51) and (5.52) which shows that the fault currents impact on both the d- and the q-current are equal in magnitude but $90°$ shifted.

However, an unbalance in the back-EMF could also be caused from an unsymmetrical rotor circuit, such as a missing rotor magnet. To see if a missing magnet will have the same effect on the harmonics content of the stator current as the turn-to-turn fault, a FEM simulation of a machine with a missing magnet is performed.

5.9 Comparison of the harmonic content of the back-EMF between a turn-to-turn fault and a missing magnet

As discussed in Section 3.3.2, the back-EMF in not solely dependent on the number of turns in a coil as it also dependent on both the coil arrangement within the winding as well as on the flux in the coils. As such, an unbalance in the back-EMF can therefore originate from an unbalance in the flux distribution between the phases. For a PMSM, an unbalanced flux distribution occurs if a permanent magnet becomes demagnetized, or if it is for any other reason removed. The healthy FEM model presented in Section 5.4 is modified where one magnet is removed, see Figure 5.29 (compare with healthy model in Figure 5.2).

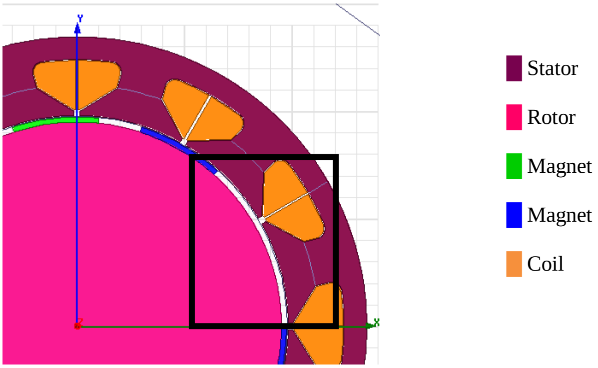

Figure 5.29 FEM model with removed permanent magnet.

The model with the missing magnet is simulated using identical settings as for the healthy machine. The simulated back-EMF is presented in Figure 5.30.

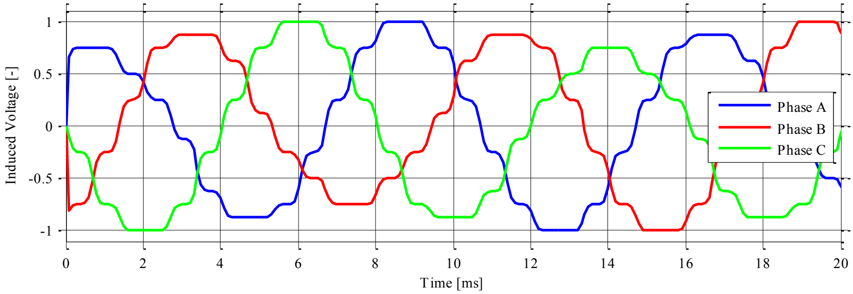

Figure 5.30 Induced voltages for the loss of magnet machine

As can be seen, the shape of the induced voltage for the loss of magnet machine is noticeably different from that of both the healthy machine (see Figure 5.5) and the machine with turn-to-turn fault (see Figure 5.12). Even though the back-EMF cannot be monitored directly, its harmonics content can be seen indirectly through the stator currents, as shown in Section 5.4.2.

The frequency content of the back-EMF for a machine which has lost a magnet is greatly different compared to both the healthy machine and a machine with turn-to-turn faults. Even sub-harmonics are present for the loss of magnet machine, see Figure 5.31.

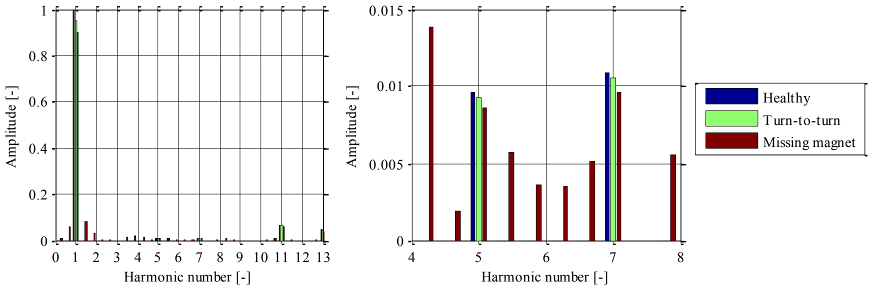

Figure 5.31 Frequency content of the induced voltages for loss of magnet, turn-to-turn and healthy machine normalized with respect to the healthy machine.

As can be seen, the loss of a magnet will produce several completely new harmonics even in the in the stationary reference frame where the turn-to-turn did not. In the case of turn-to-turn fault, the harmonic content in the stationary reference contains the same harmonic, they only become asymmetrical. It is therefore only in the rotating reference frame there will be new harmonics in the case of a turn-to-turn fault. The turn-to-turn fault will also only affect one phase, where the loss of a magnet affects all phases equally.

Even though the back-EMF cannot be monitored during operation but as shown in Section 5.4.2, the harmonics of the back-EMF will be present in stator current, though the ratio between the amplitude of fundamental and the amplitude of the harmonics may not be completely preserved for the currents.

5.10 Summary

In this chapter an analytical method of modeling a three phase PMSM with a turn-to-turn fault has been presented. The model has been mathematically transferred to the rotating reference frame aligned with the magnetic north pole of the rotor. The analytical model has been verified using a FEM model for several operational conditions which satisfactory agreement. A flexible model has been introduced which could be used both as a healthy machine model and through the users input it is able to change and it would act as the faulty machine model. The faulty machine has been modeled to have a turn-to-turn fault consisting of one turn out of the total twenty turns in one phase. This small amount of short-circuited turns does not cause any large difference in the observable stator current, even though the fault current in the machine is several times larger than the phase current. It has been shown that, even the difference between the two models was small, it is possible to detect that a turn-to-turn fault has occurred through the monitoring of the current harmonics in the rotating reference frame. In the case of turn-to-turn fault, there will be an addition of new harmonics in the rotating reference frame, introduced by both the unbalance in the machine parameters, as well as from the unbalance in the back-EMF. The unbalance in the back-EMF is caused by the reduced amount of turns in the faulty phase compared to the other healthy turns. By continuously monitoring the currents' harmonics content in the rotating reference frame in order to observe any new harmonics, it is possible to detect a turn-to-turn fault. Special attention should be given to the second harmonic together and the splitting of the pre-fault symmetrical harmonics present in the healthy machine.

Chapter 6

Conclusion and future work

This chapter will summarize this thesis and conclude with the next step for turn-to-turn detection and identification.

6.1 Conclusion

This thesis has described how to model the electrical parts of a full power converter wind turbine with a three phase PMSM as generator. In particular, the main focus of the thesis has been on the modeling of the generator unit in case of turn-to-turn faults in the stator windings. The overall electrical model of the wind turbine is obtained through the interconnection of different modules, where each module represents a sub-system. The different subsystems have been properly interconnected into one simulation model; the resulting system has been tested both under normal variations of the input wind speed and under rapid dynamic conditions (low voltage ride through). The system model is sufficiently accurate for both normal operation as well as for operation during grid faults. Furthermore, the developed model can be used to investigate the effects that a fault within one of the sub-systems has on a system level.

As presented in Chapter 5, an analytical model of a PMSM with a turn-to-turn fault has been derived. The derived model has partly been transformed into the rotating reference frame using a complimented transformation matrix, as the fault current has been kept in the stationary frame and is therefore kept as an oscillating quantity. The derived analytical model has been verified under different operational conditions using a FEM model. The comparison between the two models showed that the back-EMF vector input to the analytical model needed to be updated to include the impact of the harmonic distortion due to the geometry of the machine. A flexible model has been then developed, in order to allow the simulation of the transition from healthy to faulty machine condition.

Through the analysis of the equations describing the faulty machine in the rotating reference frame, it can be seen that the unbalanced condition of the machine leads to oscillatory component in stator current. The fault will not only impact the machine parameters, but also the back-EMF. Since the active number of turn in the faulty phase is less compared to the healthy phases (in the case of a turn-to-turn fault), the amplitude of the back-EMF in the faulty phase will be less compared with the healthy phases. In addition, for more complex geometries the back-EMF of the faulty phase will also be phase shifted compared to the non-faulty case. The unbalanced back-EMF, along with the unbalanced machine parameters, results in slightly different current for the faulty machine as compared with the non-faulty case. How much the current in the faulty machine model differs from the healthy case depends on the numbers of faulted turns. However, despite the small difference, through inspection of the harmonic content of the stator current in the rotating reference frame the unbalance caused from the turn-to-turn fault can be detected through the appearance of new harmonics for the faulty machine compared with the healthy machine. The new harmonics are caused by the splitting of the unbalanced harmonics in the back-EMF when moving to the rotating reference frame.

The main contribution of this thesis is the further development of the model of a PMSM with turn-to-turn fault (both in the stationary and in the rotating reference frame), the development of the flexible model and the suggestion of a method that can be used to detect a turn-to-turn fault in the stator windings. The developed detection method consists of the continuous monitoring of the harmonics of the stator current in the rotating reference frame in order to identify a specific variation in the harmonic content. The harmonics of special interest are the second and the splitting of the pre-fault symmetrical harmonics, which occurs due to the unsymmetrical condition of the machine caused by the turn-to-turn fault. To verify that the appearance of these specific harmonic can be used as an indication of a turn-to-turn fault and not any fault causing an unbalance in the back-EMF, a FEM model of a PMSM with a missing magnet has been simulated. The back-EMF vector of the turn-to-turn model was compared with the back-EMF vector of the missing magnet model, and in the case of a missing magnet, completely new harmonics was created where for the turn-to-turn case the harmonics stay the same except that they become unsymmetrical.

Although the main aim of the developed mathematical model was for detection of turn-to-turn faults in the PMSM, the model can also be used to investigate the impact of this kind of faults on a system level, for example to investigate their impact on the mechanical system. Furthermore, the model can be used to acquire an estimate of the amplitude of the fault current. As the number of short-circuited turns can be altered, a sensitivity analysis can be performed on the number or turns short circuited and the resulting torque ripple. As the contact resistance between turns can be varied, the impact of the value of the contact resistance on the ability to detect the turn-to-turn fault can be studied, both in terms of value and time variation.

It is of importance to stress that in this thesis the current signals used are noiseless. As the amplitude of the additional harmonics was comparably small, the measurement noise may prove to be an issue when implementing the method in an actual system setup, especially in terms of speed of the detection method. The machine in this thesis is also assumed to have perfectly linear materials, which do not change with the operational conditions. The healthy machine is assumed to be perfectly symmetrical and balanced as well as the end-winding effects are not considered. These assumptions may also prove to be an issue when implementing the method in a real system setup and open up for further research in this field.

6.2 Future work

As discussed earlier, the additional harmonics caused by the fault may have an impact on the mechanical system of the wind turbine. Further research is therefore needed to investigate the interaction between the mechanical and the electrical system during various fault conditions. This does not only consider turn-to-turn faults, but also faulty conditions in the mechanical system that might be reflected in the electrical system. This research may also lead to a method of detecting mechanical faults using the measurement of electrical signals.

Some of the current harmonics have a comparably low frequency. Therefore, if the machine controller has a sufficiently high bandwidth it may counteract the unbalance in the currents caused by the turn-to-turn fault. Thus, the impact of the controller on the detection method needs to be investigated.

The detection method is mainly based on the variation of the harmonic content in the stator current when moving from the healthy to the faulty machine. Even though the models have shown that it is possible to detect a turn-to-turn fault, there may be more effective signals to monitor, which are less sensitive to controller interaction or on the machine design. Further research is also needed to make the detection procedure automated so that is can be used for any PMSM and the method should preferably also be able to estimate how many turns that are affected. The method can also be extended to include additional faults such as the phase-to-ground and phase-to-phase short circuit.

The presented method has been verified using a FEM model; the investigated model can be further improved to more accurately model a PMSM. For instance the end-winding effects can be included. The model as well as the detection method should also be verified experimentally.

References

[1] B. Lu, Y. Li, X. Wu, and Z. Yang, "A review of recent advances in wind turbine condition monitoring and fault diagnosis," 2009.

[2] J. K. Kaldellis and D. Zafirakis, "The wind energy (r)evolution: A short review of a long history," *Renewable Energy,* vol. 36, pp. 1887-1901, 2011.

[3] E. Hau, *Wind turbines: Fundamentals, Technologies, Application, Economics*, 2nd ed. Berlin:Springer, 2006.

[4] A. D. Hansen, N. A. Cutululis, H. Markou, and P. E. Sørensen, "Impact of fault ride-through requirements on fixed-speed wind turbine structural loads," *Wind Energy,* vol. 14, pp. 1-11, 2011.

[5] G. W. E. Council, "GLOBAL WIND REPORTANNUAL MARKET UPDATE 2013," 2014.

[6] G. M. Joselin Herbert, S. Iniyan, E. Sreevalsan, and S. Rajapandian, "A review of wind energy technologies," *Renewable and Sustainable Energy Reviews,* vol. 11, pp. 1117-1145, 2007.

[7] ENERCON. (2014). Available: http://www.enercon.de/en-en/66.htm

[8] M. Liserre, R. Cárdenas, M. Molinas, and J. Rodríguez, "Overview of multi-MW wind turbines and wind parks," *IEEE Transactions on Industrial Electronics,* vol. 58, pp. 1081-1095, 2011.

[9] H. F. Polinder, Jan Abraham; Jensen, B. Bech ; Abrahamsen, Asger B.; Atallah, Kais ; McMahon, Richard A. , "Trends in Wind Turbine Generator Systems," *IEEE JOURNAL OF EMERGING AND SELECTED TOPICS IN POWER ELECTRONICS,* vol. VOL. 1,, SEPTEMBER 2013.

[10] H. Li and Z. Chen, "Overview of different wind generator systems and their comparisons," *IET Renewable Power Generation,* vol. 2, pp. 123-138, 2008.

[11] N. Espinoza, M. Bongiorno, and O. Carlson, "Grid Code Testing of Full Power Converter Based Wind Turbines Using Back-to-Back Voltage Source Converter System," in *EWEA 2013*, Vienna, 2013.

[12] "SPECIAL REPORT ON RENEWABLE ENERGY," IPCC 2011.

[13] E. J. García, "Gamesa Global technology, everlasting energy," in *2012 Wind Turbine Blade Workshop*, Albuquerque, 2012.

[14] S. M. M.R. Islam, R. Saidur, "Renewable and Sustainable Energy Reviews," *Elsevier,* 2013.

[15] M. Brockschmidt, F. Pohlmann, S. Kempen, and P. Gröppel, "Testing of nano-insulation materials: Some ideas, some experiences," 2011, pp. 506-510.

[16] H. Polinder, "Overview of and trends in wind turbine generator systems," 2011.

[17] W. C. Y. X. Z. Tan, *Wind Turbine Generator Technologies, Advances in Wind Power*, 2012.

[18] C. R. Bratiloveanu, D. T. C. Anghelus, and I. Boldea, "A comparative investigation of three PM-less MW power range wind generator topologies," 2012, pp. 535-543.
[19] P. Dvorak, "Need for new magnet materials drives research," http://www.windpowerengineering.com, 2011.
[20] H. Tiegna, Y. Amara, G. Barakat, and B. Dakyo, "Overview of high power wind turbine generators," 2012.
[21] F. M. Blaabjerg, Ke, "Future on Power Electronics for Wind Turbine Systems," *Emerging and Selected Topics in Power Electronics, IEEE Journal of*, vol. 1, pp. 139 - 152 2013.
[22] S. Kouro, M. Malinowski, K. Gopakumar, J. Pou, L. G. Franquelo, B. Wu, J. Rodriguez, M. A. Perez, and J. I. Leon, "Recent advances and industrial applications of multilevel converters," *IEEE Transactions on Industrial Electronics*, vol. 57, pp. 2553-2580, 2010.
[23] N. Mittal, B. Singh, S. P. Singh, R. Dixit, and D. Kumar, "Multilevel inverters: A literature survey on topologies and control strategies," 2012.
[24] F. Z. Peng, W. Qian, and D. Cao, "Recent advances in multilevel converter/inverter topologies and applications," 2010, pp. 492-501.
[25] M. Sztykiel, "Overview of power converter designs feasible for high voltage transformer-less wind turbine," 2011, pp. 1420-1425.
[26] H. Zhang and L. M. Tolbert, "SiC's potential impact on the design of wind generation system," 2008, pp. 2231-2235.
[27] M. R. Islam, S. Mekhilef, and R. Saidur, "Progress and recent trends of wind energy technology," *Renewable and Sustainable Energy Reviews,* vol. 21, pp. 456-468, 2013.
[28] M. S. Lu, C. L. Chang, W. J. Lee, and L. Wang, "Combining the wind power generation system with energy storage equipments," 2008.
[29] D. Bang, H. Polinder, G. Shrestha, and J. A. Ferreira, "Review of generator systems for direct-drive wind turbines," 2008, pp. 1800-1810.
[30] T. D. Strous, H. Polinder, and J. A. Ferreira, "Inductance calculations for PM machines with concentrated windings," 2011, pp. 447-452.
[31] L. Harnefors, *Control of Power Electronic Converters and Variable-Speed Drives*.
[32] R. Ottersten, "On Control of Back-to-Back Converters and Sensorless Induction Machine Drives," ed: Chalmers tekniska högskola, 2003.
[33] R. Ottersten, *On control of back-to-back converters and sensorless induction machine drives*: Ph.D. dissertation, Dept. Elect. Power Eng.,Chalmers Univ. Technol., Göteborg, Sweden, , 2003.
[34] L. Harnefors, M. Bongiorno, and S. Lundberg, "Input-admittance calculation and shaping for controlled voltage-source converters," *IEEE Transactions on Industrial Electronics,* vol. 54, pp. 3323-3334, 2007.
[35] L. Ängquist and M. Bongiorno, "Auto-normalizing Phase-Locked Loop for grid-connected converters," 2009, pp. 2957-2964.
[36] M. Beza, *Control of Energy Storage Equipped Shunt-connected Converter for Electric Power System Stability Enhancement*: Chalmers tekniska högskola, 2012.

[37] F. Spinato, P. J. Tavner, G. J. W. Van Bussel, and E. Koutoulakos, "Reliability of wind turbine subassemblies," *IET Renewable Power Generation*, vol. 3, pp. 387-401, 2009.

[38] F. Besnard, K. Fischer, and L. Bertling, "Reliability-Centred Asset Maintenance - A step towards enhanced reliability, availability, and profitability of wind power plants," 2010.

[39] B. F. S. E. J. C. P. D. F. M. J. H. M. J. T. K. J. K. M. Halling, "Improved design of large wind turbine blade of fibre composites based on studies of scale effects (Phase 1)," Risø National Laboratory2004.

[40] C. C. Ciang, J. R. Lee, and H. J. Bang, "Structural health monitoring for a wind turbine system: A review of damage detection methods," *Measurement Science and Technology,* vol. 19, 2008.

[41] G. J. W. v. B. P J Tavner, F Spinato "Machine and Converter Reliabilities in Wind Turbines " presented at the IEE 2nd International Conference on Power Electronics, Machine & Drives, Dublin, 2006.

[42] S. Yang, D. Xiang, A. Bryant, P. Mawby, L. Ran, and P. Tavner, "Condition monitoring for device reliability in power electronic converters: A review," *IEEE Transactions on Power Electronics*, vol. 25, pp. 2734-2752, 2010.

[43] M. Held, P. Jacob, G. Nicoletti, P. Scacco, and M. H. Poech, "Fast power cycling test for IGBT modules in traction application," 1997, pp. 425-430.

[44] B. Lu and S. K. Sharma, "A literature review of IGBT fault diagnostic and protection methods for power inverters," *IEEE Transactions on Industry Applications,* vol. 45, pp. 1770-1777, 2009.

[45] S. Grubic, J. M. Aller, B. Lu, and T. G. Habetler, "A survey on testing and monitoring methods for stator insulation systems of low-voltage induction machines focusing on turn insulation problems," *IEEE Transactions on Industrial Electronics*, vol. 55, pp. 4127-4136, 2008.

[46] T. B. Hammarström, Tord; Blennow, Jörgen; Gubanski, Stanislaw, "PARTIAL DISCHARGES IN A STATOR UNDER SYNTHEZISED VOLTAGE WAVEFORMS," presented at the Proceedings of the 18th International Symposium on High Voltage Engineering 2013, 2013.

[47] K. Alewine and W. Chen, "A review of electrical winding failures in wind turbine generators," 2011, pp. 392-397.

[48] B. Vaseghi, B. Nahid-Mobarekeh, N. Takorabet, and F. Meibody-Tabar, "Experimentally validated dynamic fault model for PMSM with stator winding inter-turn fault," 2008.

[49] B. Vaseghi, B. Nahid-Mobarakeh, N. Takorabet, and F. Meibody-Tabar, "Modeling of non-salient PM synchronous machines under stator winding inter-turn fault condition: Dynamic model - FEM model," 2007, pp. 635-640.

[50] W. Tang, G. Liu, and J. Ji, "Winding turn-to-turn faults detection of five-phase fault-tolerant permanent-magnet machine based on parametric model," 2012.

[51] M. Bongiorno, J. Svensson, and A. Sannino, "Effect of sampling frequency and harmonics on delay-based phase-sequence estimation method," *IEEE Transactions on Power Delivery*, vol. 23, pp. 1664-1672, 2008.

Appendix A

Moving from stationary to rotating reference frame

A widely used mathematical transformation in the electrical engineering discipline is the transformation from the stationary to the rotating reference frame. This makes an oscillating quantity at the transformation frequency appear as a DC quantity. The mathematical transformation matrix for a three phase system is

$$T_1(\theta) = K\frac{2}{3}\begin{bmatrix} \cos\theta & \cos\left(\theta - \frac{2\pi}{3}\right) & \cos\left(\theta + \frac{2\pi}{3}\right) \\ -\sin\theta & -\sin\left(\theta - \frac{2\pi}{3}\right) & -\sin\left(\theta + \frac{2\pi}{3}\right) \\ \frac{1}{3} & \frac{1}{3} & \frac{1}{3} \end{bmatrix} \tag{A.1}$$

where θ is the transformation angle related to the rotational speed of the rotating reference frame and K is a scaling constant. By selecting K to 1 the transformation becomes amplitude invariant.

The inverse of the transformation matrix is

$$T_1^{-1}(\theta) = K\begin{bmatrix} \cos\theta & -\sin\theta & 1 \\ \cos\left(\theta - \frac{2\pi}{3}\right) & -\sin\left(\theta - \frac{2\pi}{3}\right) & 1 \\ \cos\left(\theta + \frac{2\pi}{3}\right) & -\sin\left(\theta + \frac{2\pi}{3}\right) & 1 \end{bmatrix} \tag{A.2}$$

If the zero sequence component is neglected the transformation matrix becomes

$$T(\theta) = K\frac{2}{3}\begin{bmatrix} \cos\theta & \cos\left(\theta - \frac{2\pi}{3}\right) & \cos\left(\theta + \frac{2\pi}{3}\right) \\ \sin\theta & \sin\left(\theta - \frac{2\pi}{3}\right) & \sin\left(\theta + \frac{2\pi}{3}\right) \end{bmatrix} \tag{A.3}$$

with the inverse

$$T^{-1}(\theta) = K\begin{bmatrix} \cos\theta & \sin\theta \\ \cos\left(\theta - \frac{2\pi}{3}\right) & \sin\left(\theta - \frac{2\pi}{3}\right) \\ \cos\left(\theta + \frac{2\pi}{3}\right) & \sin\left(\theta + \frac{2\pi}{3}\right) \end{bmatrix} \tag{A.4}$$

For a balanced frequency component with equal speed as the rotating reference frame the transformed components becomes

$$K\frac{2}{3}\begin{bmatrix}\cos\theta & \cos\left(\theta-\frac{2\pi}{3}\right) & \cos\left(\theta+\frac{2\pi}{3}\right)\\ \sin\theta & \sin\left(\theta-\frac{2\pi}{3}\right) & \sin\left(\theta+\frac{2\pi}{3}\right)\end{bmatrix}\begin{bmatrix}A_a\cos\theta\\ A_b\cos\left(\theta-\frac{2\pi}{3}\right)\\ A_c\cos\left(\theta+\frac{2\pi}{3}\right)\end{bmatrix}=$$
$$K\frac{1}{3}\begin{bmatrix}A_a+A_b+A_c+A_a\cos 2\theta+A_b\cos\left(2\theta-\frac{4\pi}{3}\right)+A_c\cos\left(2\theta+\frac{4\pi}{3}\right)\\ A_a\sin 2\theta+A_b\sin\left(2\theta-\frac{4\pi}{3}\right)+A_c\sin\left(2\theta+\frac{4\pi}{3}\right)\end{bmatrix} \quad \text{(A.5)}$$

If $A_a = A_b = A_c = A$ then (A.5) become $\begin{bmatrix}AK\\0\end{bmatrix}$ since the double frequency component is perfectly symmetric. Similar calculations can be done for the harmonics. If they are balanced they will only appear at one frequency where the other will be canceled due to symmetry.

Vector representation of three phase quantities

A three-phase positive system constituted by the three quantities $x_1(t)$, $x_2(t)$ and $x_3(t)$ can be transformed into a vector in a complex reference frame, usually called $\alpha\beta$-frame, by applying the transformation defined by:

$$\underline{x} = x_\alpha(t) + \mathrm{j}x_\beta(t) = K\cdot\left[x_1(t) + x_2(t)\cdot \mathrm{e}^{\mathrm{j}\frac{2}{3}\pi} + x_3(t)\cdot \mathrm{e}^{\mathrm{j}\frac{4}{3}\pi}\right] \quad \text{(A.6)}$$

where the factor K is usually taken equal to $\sqrt{\frac{3}{2}}$ for ensuring power invariance between the two systems. Equation (A.1) can be expressed as a matrix equation:

$$\begin{bmatrix}x_\alpha(t)\\ x_\beta(t)\end{bmatrix} = \mathbf{C}_{23}\begin{bmatrix}x_1(t)\\ x_2(t)\\ x_3(t)\end{bmatrix} \quad \text{(A.7)}$$

where:

$$\mathbf{C}_{23} = \begin{bmatrix}\sqrt{\frac{2}{3}} & -\frac{1}{\sqrt{6}} & -\frac{1}{\sqrt{6}}\\ 0 & \frac{1}{\sqrt{2}} & -\frac{1}{\sqrt{2}}\end{bmatrix} \quad \text{(A.8)}$$

The inverse transformation is given by:

$$\begin{bmatrix} x_1(t) \\ x_2(t) \\ x_3(t) \end{bmatrix} = \mathbf{C_{32}} \begin{bmatrix} x_\alpha(t) \\ x_\beta(t) \end{bmatrix} \tag{A.9}$$

where:

$$\mathbf{C_{32}} = \begin{bmatrix} \sqrt{\frac{2}{3}} & 0 \\ -\frac{1}{\sqrt{6}} & \frac{1}{\sqrt{2}} \\ -\frac{1}{\sqrt{6}} & -\frac{1}{\sqrt{2}} \end{bmatrix} \tag{A.10}$$

This holds under the assumption that the sum of the three quantities is zero. Otherwise, there will also be a constant (zero-sequence) component. In the latter case, Eqs.(A.7) and (A.9) become:

$$\begin{bmatrix} x_\alpha(t) \\ x_\beta(t) \\ x_o(t) \end{bmatrix} = \mathbf{C_{23o}} \begin{bmatrix} x_1(t) \\ x_2(t) \\ x_3(t) \end{bmatrix} \tag{A.11}$$

and for the inverse transformation:

$$\begin{bmatrix} x_1(t) \\ x_2(t) \\ x_3(t) \end{bmatrix} = \mathbf{C_{32o}} \begin{bmatrix} x_\alpha(t) \\ x_\beta(t) \\ x_o(t) \end{bmatrix} \tag{A.12}$$

with the two matrixes given by:

$$\mathbf{C_{23o}} = \begin{bmatrix} \sqrt{\frac{2}{3}} & -\frac{1}{\sqrt{6}} & -\frac{1}{\sqrt{6}} \\ 0 & \frac{1}{\sqrt{2}} & -\frac{1}{\sqrt{2}} \\ \frac{1}{\sqrt{6}} & \frac{1}{\sqrt{6}} & \frac{1}{\sqrt{6}} \end{bmatrix} \tag{A.13}$$

and

$$\mathbf{C_{32o}} = \begin{bmatrix} \sqrt{\frac{2}{3}} & 0 & \frac{1}{\sqrt{6}} \\ -\frac{1}{\sqrt{6}} & \frac{1}{\sqrt{2}} & \frac{1}{\sqrt{6}} \\ -\frac{1}{\sqrt{6}} & -\frac{1}{\sqrt{2}} & \frac{1}{\sqrt{6}} \end{bmatrix} \tag{A.14}$$

Voltage vectors for unsymmetrical three-phase systems

The phase voltages for a three-phase system can be written as:

$$\begin{aligned} e_a(t) &= \hat{e}_a(t)\cdot\cos(\omega t-\varphi_a) \\ e_b(t) &= \hat{e}_b(t)\cdot\cos(\omega t-\frac{2}{3}\pi-\varphi_b) \\ e_c(t) &= \hat{e}_c(t)\cdot\cos(\omega t-\frac{4}{3}\pi-\varphi_c) \end{aligned} \tag{A.15}$$

where $\hat{e}_a(t)$, $\hat{e}_b(t)$ and $\hat{e}_c(t)$ are the amplitudes of the three-phase voltages, φ_a, φ_b and φ_c are the phase angles of the three-phase voltages, and ω is the angular frequency of the system.

If the amplitudes $\hat{e}_a(t)$, $\hat{e}_b(t)$ and $\hat{e}_c(t)$ are unequal, the voltage vector can be written as the sum of two vectors rotating in opposite directions and interpreted as positive- and negative-sequence vectors:

$$\underline{e}^{(\alpha\beta)}(t) = E_p \mathrm{e}^{\mathrm{j}(\omega t+\varphi_\mathrm{p})} + E_n \mathrm{e}^{\text{-}\mathrm{j}(\omega t+\varphi_\mathrm{n})} \tag{A.16}$$

where E_p and E_n are the amplitudes of positive- and negative-sequence vectors, respectively, and the corresponding phase angles are denoted by φ_p and φ_n. To determine amplitudes and phase angles of positive- and negative-sequence vectors in Eq. (A.19), a two-step solving technique can be used. First, the phase shifts are set to zero, so that the amplitudes E_p and E_n can easily be detected. In the next step, the phase shifts φ_p and φ_n are determined.

Appendix B

FEM Machine Parameters

Machine parameters

R_s	1.6 mΩ
R_f	20 mΩ
L	292 μH
M	-12 μ
M_{af}	12.6 μH
M_{bf}	0.12 μH
M_{cf}	-1.35μH
L_f	2.75 μH
Ψ_{pm}	0.068
Pole pairs	5
f_0	125 Hz

Machine geometry

Stator diameter	270 mm
Rotor diameter	190 mm
Airgap	3.1 mm
Magnet height	2.3 mm
Magnet length	80 mm
Stator back	10.5 mm
Shoe height	2 mm
Tooth width	21 mm
Slot width	38 mm
Stack length	109 mm

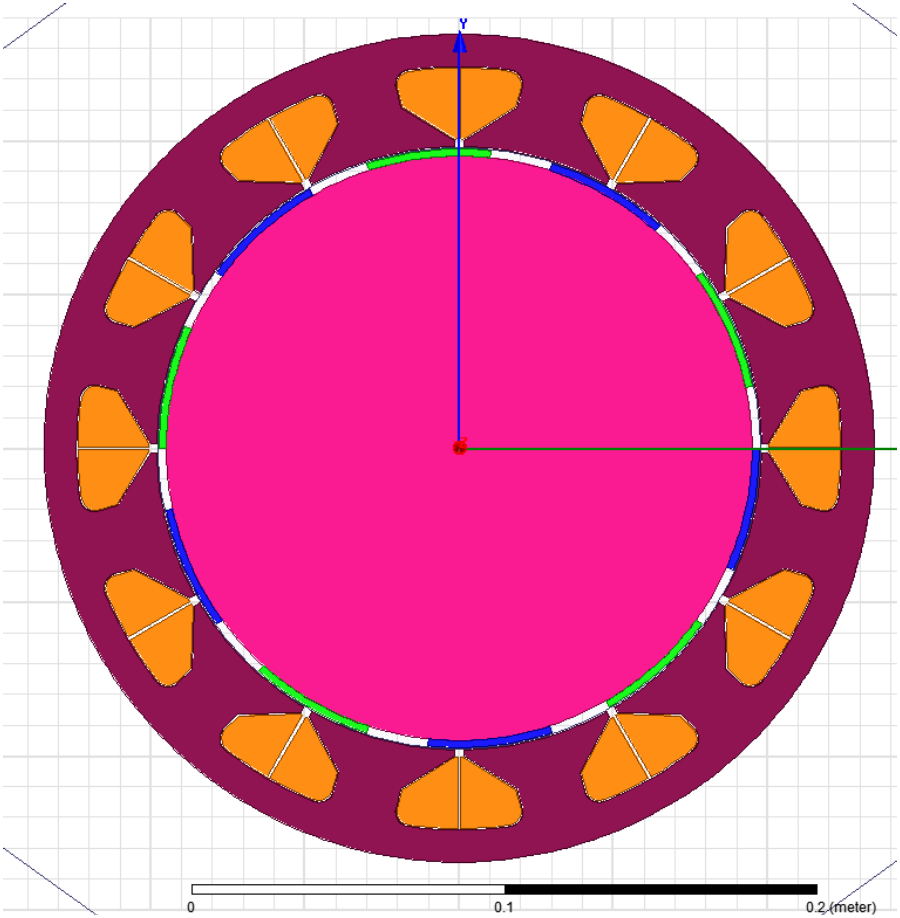
Y
0
0.1
0.2 (meter)

Appendix C

*Parameter values of the **A** matrix in (5.51)and the **B** matrix in (5.52)*

$$\boldsymbol{A}[1,1] = \frac{\mathrm{Lf}(-L+M)\mathrm{Rs} + \mathrm{K1K9}(L-M)\mathrm{Cos}[\mathrm{K10}-\mathrm{thetaR}]\mathrm{Cos}[\mathrm{K2}-\mathrm{thetaR}] + \mathrm{K1K5Cos}[\mathrm{K4}-\mathrm{thetaR}]((-L+M)\mathrm{wrCos}[\mathrm{K2}-\mathrm{thetaR}] + \mathrm{RsCos}[\mathrm{K4}-\mathrm{thetaR}])}{(L-M)(\mathrm{Lf}(L-M) - \mathrm{K1K5}(\mathrm{Cos}[\mathrm{K2}-\mathrm{thetaR}]^2 + \mathrm{Cos}[\mathrm{K4}-\mathrm{thetaR}]^2))}$$

$$\boldsymbol{A}[1,2] = -\frac{2\mathrm{K1K9}(L-M)\mathrm{Cos}[\mathrm{K12}-\mathrm{thetaR}]\mathrm{Cos}[\mathrm{K2}-\mathrm{thetaR}] + 2\mathrm{K1K5RsCos}[\mathrm{K2}-\mathrm{thetaR}]\mathrm{Cos}[\mathrm{K4}-\mathrm{thetaR}] + (L-M)\mathrm{wr}(\mathrm{K1K5} - 2L\mathrm{Lf} + 2\mathrm{Lf}M + \mathrm{K1K5Cos}[2(\mathrm{K4}-\mathrm{thetaR})])}{2(L-M)(\mathrm{Lf}(L-M) - \mathrm{K1K5}(\mathrm{Cos}[\mathrm{K2}-\mathrm{thetaR}]^2 + \mathrm{Cos}[\mathrm{K4}-\mathrm{thetaR}]^2))}$$

$$\boldsymbol{A}[1,3] = \frac{2\mathrm{Rssigma}(\mathrm{Lf}(L-M) - \mathrm{K1K5Cos}[\mathrm{K4}-\mathrm{thetaR}]^2)\mathrm{Cos}[\mathrm{thetaR}] + \mathrm{K1Cos}[\mathrm{K2}-\mathrm{thetaR}](3(L-M)(\mathrm{Rf}+\mathrm{Rssigma}) - 2\mathrm{K5RssigmaCos}[\mathrm{K4}-\mathrm{thetaR}]\mathrm{Sin}[\mathrm{thetaR}])}{3(L-M)(\mathrm{Lf}(L-M) - \mathrm{K1K5}(\mathrm{Cos}[\mathrm{K2}-\mathrm{thetaR}]^2 + \mathrm{Cos}[\mathrm{K4}-\mathrm{thetaR}]^2))}$$

$$\boldsymbol{A}[2,1] = \frac{-\mathrm{Lf}(L-M)^2\mathrm{wr} + \mathrm{K1K5}(L-M)\mathrm{wrCos}[\mathrm{K2}-\mathrm{thetaR}]^2 + \mathrm{K1}(\mathrm{K9}(L-M)\mathrm{Cos}[\mathrm{K10}-\mathrm{thetaR}] - \mathrm{K5RsCos}[\mathrm{K2}-\mathrm{thetaR}])\mathrm{Cos}[\mathrm{K4}-\mathrm{thetaR}]}{(L-M)(\mathrm{Lf}(L-M) - \mathrm{K1K5}(\mathrm{Cos}[\mathrm{K2}-\mathrm{thetaR}]^2 + \mathrm{Cos}[\mathrm{K4}-\mathrm{thetaR}]^2))}$$

$$\boldsymbol{A}[2,2] = \frac{\mathrm{Lf}(-L+M)\mathrm{Rs} + \mathrm{K1K5RsCos}[\mathrm{K2}-\mathrm{thetaR}]^2 - \mathrm{K1}(L-M)(\mathrm{K9Cos}[\mathrm{K12}-\mathrm{thetaR}] - \mathrm{K5wrCos}[\mathrm{K2}-\mathrm{thetaR}])\mathrm{Cos}[\mathrm{K4}-\mathrm{thetaR}]}{(L-M)(\mathrm{Lf}(L-M) - \mathrm{K1K5}(\mathrm{Cos}[\mathrm{K2}-\mathrm{thetaR}]^2 + \mathrm{Cos}[\mathrm{K4}-\mathrm{thetaR}]^2))}$$

$$\boldsymbol{A}[2,3] = \frac{\mathrm{K1Cos}[\mathrm{K4}-\mathrm{thetaR}](3(L-M)(\mathrm{Rf}+\mathrm{Rssigma}) + 2\mathrm{K5RssigmaCos}[\mathrm{K2}-\mathrm{thetaR}]\mathrm{Cos}[\mathrm{thetaR}]) + 2\mathrm{Rssigma}(\mathrm{Lf}(-L+M) + \mathrm{K1K5Cos}[\mathrm{K2}-\mathrm{thetaR}]^2)\mathrm{Sin}[\mathrm{thetaR}]}{3(L-M)(\mathrm{Lf}(L-M) - \mathrm{K1K5}(\mathrm{Cos}[\mathrm{K2}-\mathrm{thetaR}]^2 + \mathrm{Cos}[\mathrm{K4}-\mathrm{thetaR}]^2))}$$

$$\boldsymbol{A}[3,1] = \frac{\mathrm{K9}(-L+M)\mathrm{Cos}[\mathrm{K10}-\mathrm{thetaR}] + \mathrm{K5RsCos}[\mathrm{K2}-\mathrm{thetaR}] + \mathrm{K5}(L-M)\mathrm{wrCos}[\mathrm{K4}-\mathrm{thetaR}]}{\mathrm{Lf}(L-M) - \mathrm{K1K5}(\mathrm{Cos}[\mathrm{K2}-\mathrm{thetaR}]^2 + \mathrm{Cos}[\mathrm{K4}-\mathrm{thetaR}]^2)}$$

$$\boldsymbol{A}[3,2] = \frac{(L-M)(\mathrm{K9Cos}[\mathrm{K12}-\mathrm{thetaR}] - \mathrm{K5wrCos}[\mathrm{K2}-\mathrm{thetaR}]) + \mathrm{K5RsCos}[\mathrm{K4}-\mathrm{thetaR}]}{\mathrm{Lf}(L-M) - \mathrm{K1K5}(\mathrm{Cos}[\mathrm{K2}-\mathrm{thetaR}]^2 + \mathrm{Cos}[\mathrm{K4}-\mathrm{thetaR}]^2)}$$

$$\boldsymbol{A}[3,3] = \frac{3(L-M)(\mathrm{Rf}+\mathrm{Rssigma}) + \mathrm{K5Rssigma}(\mathrm{Cos}[\mathrm{K2}] + \mathrm{Cos}[\mathrm{K2}-2\mathrm{thetaR}] - 2\mathrm{Cos}[\mathrm{K4}-\mathrm{thetaR}]\mathrm{Sin}[\mathrm{thetaR}])}{3(\mathrm{K1K5} + \mathrm{Lf}(-L+M) + \mathrm{K1K5Cos}[\mathrm{K2}-\mathrm{K4}]\mathrm{Cos}[\mathrm{K2}+\mathrm{K4}-2\mathrm{thetaR}])}$$

$$\boldsymbol{B}[1,1] = \frac{\mathrm{Lf}(-L+M) + \mathrm{K1K5Cos}[\mathrm{K4} - \mathrm{thetaR}]^2}{\mathrm{Lf}(-L+M) + \mathrm{K1K5Cos}[\mathrm{K4} - \mathrm{thetaR}]^2(L-M) + \mathrm{K1K5}(L-M)\mathrm{Cos}[\mathrm{K2} - \mathrm{thetaR}]^2}$$

$$\boldsymbol{B}[1,2] = \frac{\mathrm{K1K5Cos}[\mathrm{K2} - \mathrm{thetaR}]\mathrm{Cos}[\mathrm{K4} - \mathrm{thetaR}]}{(L-M)(\mathrm{Lf}(L-M) - \mathrm{K1K5}(\mathrm{Cos}[\mathrm{K2} - \mathrm{thetaR}]^2 + \mathrm{Cos}[\mathrm{K4} - \mathrm{thetaR}]^2))}$$

$$\boldsymbol{B}[1,3] = -\frac{\mathrm{K1PsiPMCos}[\mathrm{K2} - \mathrm{thetaR}](\mathrm{K5Cos}[\mathrm{K4} - \mathrm{thetaR}] + (-L+M)\mathrm{sigmaSin}[\mathrm{shift} + \mathrm{thetaR}])}{(L-M)(\mathrm{Lf}(L-M) - \mathrm{K1K5}(\mathrm{Cos}[\mathrm{K2} - \mathrm{thetaR}]^2 + \mathrm{Cos}[\mathrm{K4} - \mathrm{thetaR}]^2))}$$

$$\boldsymbol{B}[2,1] = \frac{\mathrm{K1K5Cos}[\mathrm{K2} - \mathrm{thetaR}]\mathrm{Cos}[\mathrm{K4} - \mathrm{thetaR}]}{(L-M)(\mathrm{Lf}(L-M) - \mathrm{K1K5}(\mathrm{Cos}[\mathrm{K2} - \mathrm{thetaR}]^2 + \mathrm{Cos}[\mathrm{K4} - \mathrm{thetaR}]^2))}$$

$$\boldsymbol{B}[2,2] = \frac{\mathrm{Lf}(-L+M) + \mathrm{K1K5Cos}[\mathrm{K2} - \mathrm{thetaR}]^2}{(L-M)(\mathrm{Lf}(-L+M) + \mathrm{K1K5Cos}[\mathrm{K2} - \mathrm{thetaR}]^2) + \mathrm{K1K5}(L-M)\mathrm{Cos}[\mathrm{K4} - \mathrm{thetaR}]^2}$$

$$\boldsymbol{B}[2,3] = \frac{\mathrm{PsiPM}(\mathrm{K1K5Cos}[\mathrm{K2} - \mathrm{thetaR}]^2 - (L-M)(\mathrm{Lf} - \mathrm{K1sigmaCos}[\mathrm{K4} - \mathrm{thetaR}]\mathrm{Sin}[\mathrm{shift} + \mathrm{thetaR}]))}{(L-M)(\mathrm{Lf}(L-M) - \mathrm{K1K5}(\mathrm{Cos}[\mathrm{K2} - \mathrm{thetaR}]^2 + \mathrm{Cos}[\mathrm{K4} - \mathrm{thetaR}]^2))}$$

$$\boldsymbol{B}[3,1] = \frac{\mathrm{K5Cos}[\mathrm{K2} - \mathrm{thetaR}]}{\mathrm{Lf}(-L+M) + \mathrm{K1K5}(\mathrm{Cos}[\mathrm{K2} - \mathrm{thetaR}]^2 + \mathrm{Cos}[\mathrm{K4} - \mathrm{thetaR}]^2)}$$

$$\boldsymbol{B}[3,2] = \frac{\mathrm{K5Cos}[\mathrm{K4} - \mathrm{thetaR}]}{\mathrm{Lf}(-L+M) + \mathrm{K1K5}(\mathrm{Cos}[\mathrm{K2} - \mathrm{thetaR}]^2 + \mathrm{Cos}[\mathrm{K4} - \mathrm{thetaR}]^2)}$$

$$\boldsymbol{B}[3,3] = \frac{\mathrm{K5PsiPMCos}[\mathrm{K4} - \mathrm{thetaR}] + (-L+M)\mathrm{PsiPMsigmaSin}[\mathrm{shift} + \mathrm{thetaR}]}{\mathrm{Lf}(L-M) - \mathrm{K1K5}(\mathrm{Cos}[\mathrm{K2} - \mathrm{thetaR}]^2 + \mathrm{Cos}[\mathrm{K4} - \mathrm{thetaR}]^2)}$$